To the Graduate Council:

I am submitting herewith a dissertation written by Brent William Blaha entitled "Characteristics of Laser Heat Treating During Processing of a Low Carbon Steel". I have examined the final copy of this dissertation for form and content and recommend that it be accepted in partial fulfillment of the requirements for the degree of Doctor of Philosophy, with a major in Mechanical Engineering.

T. Dwayne McCay, Major Professor

We have read this dissertation
and recommend its acceptance:

Accepted for the Council:

Interim Vice Provost and
Dean of The Graduate School

CHARACTERISTICS OF LASER HEAT TREATING DURING PROCESSING OF A LOW CARBON STEEL

A Dissertation
Presented for the
Doctor of Philosophy
Degree
The University of Tennessee, Knoxville

Brent W Blaha
August 2001

Dedicated to my loving wife, Elina

Out of the night that covers me,
Black as a Pit from pole to pole,
I thank whatever gods may be
For my unconquerable soul.
In the fell clutch of circumstance
I have not winced nor cried aloud,
Under the bludgeonings of chance
My head is bloody, but unbowed.
Beyond this place of wrath and tears
Looms but the horror of the shade,
And yet the menace of the years
Finds,and shall find me, unafraid.
It matters not how straight the gate,
How charged with punishments the scroll,
I am the master of my fate:
I am the captain of my soul.

INVICTUS, *W.E. Henley, 1875*

ACKNOWLEDGEMENTS

I would like to thank everybody who contributed to the completion of this work in some way or another. A special thanks goes to my advisor, Dr. Dwayne McCay, for his guidance, support, and ability to see me through to the end. Dr. Mary Helen McCay, Dr. John Hopkins, and Dr. Naren Dahotre have been instrumental in teaching me the ways around a laboratory and the physics behind laser materials processing.

Over the years, I have had countless opportunities to share ideas with numerous fellow students: Ram Sivakumaran, Martin Kalberer, Ruben Bons, Jon Winkler, Terri Tramel and Arvind Aggarwal. To you I say thanks also.

None of the work could have been accomplished without the efforts of the full time staff at UTSI's Center for Laser Applications. These include Fred Schwartz, who makes the lasers work, Jim Hornkohl, who makes the computers work, and Newt Wright, who makes everything else work. In addition, Carole Thomas, Penny Smith, and Diane Chellstorp have always been of assistance and always with a kind word.

Lastly, I would especially like to thank my wife Elina. I've pushed her patience beyond that which any person should reasonably expect; yet it was not lost. Thank you for your unending support over the years.

ABSTRACT

Some of the characteristics of laser heat treating are examined. A numerical model has been created that quantifies the transient thermal field to assist in the prediction of heating and cooling rates that influence the transformation from one solid phase to another. The model is compared to experiments performed on coupons of AISI 1050 steel with a Nd:YAG . By comparing experimental heat affected zone depths with corresponding modeled thermal fields, an estimate of the influence of heating rate on the temperature at which ferrite begins to transform to other phases is made.

Bulk heating from repetitive tracks is seen to reduce cooling rates in subsequent processing tracks, though they remain high and the reduction is not likely to influence transformations that depend on high cooling rates (austenite to martensite for example).

TABLE OF CONTENTS

I Introduction 1

II Background 4
2.1 Energy Equation 4
2.2 Analytical Work 6
2.3 Modeling Work 12
2.4 Multitrack Work 14

III Theory 16
3.1 Model 16
3.2 Thermal Properties 22
3.3 Heat Treat Physics 22

IV Model 28
4.1 Sample Preparation and Experimentation 28
4.2 CFD-ACE 30
4.3 Boundary Conditions 32
4.4 Thermophysical Properties 34
4.5 Solver Modification 35
4.6 Input file Modifications 37
4.7 Grid Generation 37
4.8 Timestep Determination 46
4.9 Comparison with Temperature Measurements 60

V Experimental and Numerical 69
5.1 Numerical Processing Parameters 69
5.2 Experimental Processing Parameters 70

VI Results and Discussion 75
6.1 Single Tracks 75
6.2 Multiple Tracks 78
6.3 Numerical Results 84
6.4 Discussion 89

VII Conclusion 98

List of References 101

Appendices 105
Appendix A: User Boundary Condition 106
Appendix B: Modified Input File 113

Vita 116

LIST OF FIGURES

Figure		Page
2.1	Schematic of a volumetric heat source	7
2.2	Schematic of a boundary heat source	8
3.1	Laser heat treating domain of interest.	17
3.2	A rectangular tophat beam profile	19
3.3	An elliptical Guassian beam profile.	20
3.4	Isothermal Transformation diagram for 1050 steel.	24
3.5	Continuous Cooling Transformation diagram for 1040 steel	25
3.6	Effect of heating rate on the temperature at which ferrite transforms to austenite in pure iron	26
3.7	The effect of heating rate on the temperature at which austenite forms in steel with 0.8% carbon content.	27
4.1	Thermophysical properties for AISI 1050 steel.	36
4.2	The influence of grid resolution on the resulting surface temperature profile at the center of the track.	41
4.3	The influence of grid spacing on the peak temperature at any point on the surface.	42
4.4	Orthographic view of the model grid depicting how the grid spacing varies spatially.	43
4.5	Side composite of the model grid	44
4.6	Top view of the model grid	45
4.7	Peak surface temperatures for 10 millisecond time step	48
4.8	Peak surface temperatures for 7.5 millisecond time step	49
4.9	Peak surface temperatures for 6 millisecond time step	50
4.10	Peak surface temperatures for 4.44 millisecond time step	51

4.11 Peak surface temperatures for 3 millisecond time step 52

4.12 Peak surface temperatures for 1.5 millisecond time step 53

4.13 Peak surface temperatures for 0.75 millisecond time step 54

4.14 Peak surface temperatures for 0.5 millisecond time step 55

4.15 Peak surface temperatures for 0.25 millisecond time step 56

4.16 The influence of the discrete time step on peak temperatures. 57

4.17 The magnitude of the thermal oscillation at different timestep sizes 58

4.18 The wavelength of the thermal oscillation at different time steps 59

4.19 Instrumented steel coupon showing the typical location of the thermocouples 62

4.20 Comparing measured and modeled temperature profiles for run 1 63

4.21 Comparing measured and modeled temperature profiles for run 2 64

4.22 Comparing measured and modeled temperature profiles for run 3 65

4.23 Comparing measured and modeled temperature profiles for run 4 66

4.24 Comparing measured and modeled temperature profiles for run 5 67

4.25 Comparing measured and modeled temperature profiles for run 6 68

5.1 Measured beam profile for 4643 optics at focus for a) beam width (direction of beam travel) and b) beam length 71

5.2 Measured beam profile for 6644 optics at focus for a) beam width (direction of beam travel) and b) beam length 73

6.1 Image showing the heat affected zone for a single track 76

6.2 The track center depth of the heat affected zone at different beam powers .. 79

6.3 Schematics of multiple track runs (a) and resulting heat affected zone (b) .. 80

6.4 Image showing the HAZ for three overlapping tracks. 81

6.5 HAZ depths resulting from each track at various indices using a 871 watt beam 85

6.6 HAZ depths resulting from each track at various indices using a 968 watt beam 86

6.7 HAZ depths resulting from each track at various indices using a 1089 watt beam 87

6.8 Peak temperature contour lines after the completion of the first, second and third tracks respectively 88

6.9 Cumulative 1000 K isotherm depth 90

6.10 HAZ depth sensitivity to temperature changes resulting from bulk heating. 91

6.11 Peak cooling rate isolines 92

6.12 Cooling rates near the surface for each track 93

6.13 Time spent above 1000 K 94

6.14 Influence of the track number on the amount of time spent above the 1000 K isotherm 95

6.15 Predicted transition temperature from different absorption coefficients 97

LIST OF SYMBOLS AND ABBREVIATIONS

Abbreviations

s	second
m	meter
mm	millimeter
kg	kilogram
W	watts
min	minute
J	joules
K	degrees Kelvin
AISI	American Iron and Steel Institute
BC	boundary condition
LHT	laser heat heating
HAZ	heat affected zone
TC	thermocouple
UTSI	University of Tennessee Space Institute

Symbols

α	absorption coefficient
ε	emmisivity
π	pi (3.141592654)
ρ	density (kg/m^3)
σ	Stefan Boltzmann constant ($5.67x10^{-8}$ W/m^2K^4)
C_p	specific heat (J/kgK)
h	enthalpy (J/kg)
h_t	convective heat transfer coefficient (W/m^2K)
H	domain length in z direction (mm)
k	conductivity (W/mK)
l_p	distance beam travels (mm)
L	domain length in x direction (mm)
n	number of completed tracks
P	beam power (W)
P_0	beam power (W)
q"	beam flux (W/m^2)
$q"_b$	energy flux at the boundary (W/m^2)
Q	Volumetric heat source (W/m^3)
t	time (s)
t_l	single track total time (s)
t*	time into current track (s)
Δt	time step size (s)
Δt	time from the end of the first track to the start of the second (s)
T	temperature (K)
T_∞	freestream temperature (K)

T_0	initial temperature (K)
T_b	boundary temperature (K)
T_{surr}, T_w	surroundings/wall temperature (K)
V	beam speed (mm/min)
w	beam width (mm)
W	domain length in y direction (mm)
x,y,z	coordinates (mm)
$x_b(t)$, $y_b(t)$	beam location at any t (mm)
x_{b0}, y_{b0}	beam location at t = 0s (mm)
x_r	beam radii to 1/e point in x direction (Guassian beam) (mm)
x_r	beam ½ width in x direction (rectangular tophat beam) (mm)
y_r	beam radii to 1/e in y direction (Gaussian beam) (mm)
y_r	beam ½ length in y direction (rectangular tophat beam) (mm)
Δy	index (mm)

CHAPTER I

INTRODUCTION

The use of lasers in materials processing is widespread. Lasers are used for welding, cutting, drilling, and even heat treating [1]. Laser surface alloying can now be used to improve desired mechanical properties. For example, steel like hardness on the surface of aluminum can be achieved by using a laser to melt carbide particles into the surface of the aluminum [2].

Consider the process of transformation hardening a low carbon ferritic steel using a laser. Typically, a laser beam focussed to a desired energy density and moving with a given velocity with respect to the substrate material traverses some distance across the surface of the substrate. As the beam passes over a particular spot on the substrate, the absorbed energy heats the surface of the material at that location. Depending on the beam energy density and speed, portions of the material near the surface are heated to elevated temperatures and the phase of the base material may transform to other phases. For example, above the austenitic temperature, ferrite may transform into austenite. The transformation, if any, is typically limited to a very small depth relative to the "bulk" depth of the substrate. After the beam passes the spot and energy is no longer being absorbed at the surface, the bulk of the substrate acts like a large heat sink, rapidly quenching the heated portions near the surface. At low cooling rates, any austenite will transform back into ferrite, since austenite is unstable below the austenitic temperature. However, if the cooling rate is high, such as achieved in quenching, the austenite will transform to martensite. The beam, displaced from its starting position forming what will

hereafter be termed a track, is offset by an amount such that a new track is formed that overlaps with the first. Multiple, overlapping tracks can thus be used to process large areas of substrate material.

However, in the regions where the tracks overlap, the material has actually been treated twice (or more, depending on overlap and beam size). These regions will possibly have a different phase distribution than in regions that are treated only once. In overlap regions, the additional treatment opportunities could lead to additional ferrite to austenite, resulting in a higher amount of martensite, relative to the non-overlap regions. To further complicate the heat treat process, the martensite formed from the first track is itself heat-treated during subsequent tracks, which may lead to the formation of ferrite and carbide ("tempered martensite") [3]. Annealing may also take place. The end result, after processing an entire region, is a possibly complicated distribution of many different steel phases near the surface of the treated substance. The diverse microstructure can lead to undesirable consequences.

In traditional heat treating, the material to be treated is heated uniformly to a temperature above the eutectoid temperature (where ferrite transitions to austenite, 723 C) and held for anywhere between a few minutes to as long as several hours. The length of time spent above the transition temperature influences the amount of austenite that forms (since the change of ferrite to austenite is a diffusion transformation) as well as the size of the austenite grains. Upon quenching to room temperature, martensite forms. Continuous cooling curves predict the amount of martensite that forms based on the rate at which the material cools.

Therein are several differences between laser heat treating (LHT) and traditional heat-treating. In LHT, the ability to control the amount of time spent above the transition temperature is far less direct. Indeed, the time is predicted to be significantly less than traditional heat-treating allows. The addition of multiple tracks tends to increase the bulk temperature of the material which reduces the quench effectiveness of the bulk. Additionally, the non-uniformity of the thermal field affects the transformation process since higher temperatures favor increased atom mobility in the transformations that require diffusion, such as ferrite to austenite [4]. Lastly, the transition temperature at which ferrite in low carbon steels transforms to other phases is itself influenced by the heating rate [5]. All these factors become present in LHT that are not otherwise considered by traditional heat treating processes.

This dissertation attempts to determine the influence of these factors during LHT of a low carbon steel (AISI 1050). By creating a computational model that calculates the time dependent thermal field and comparing its predicted isotherms and heating and cooling rates to the results of actual LHT of 1050 steel, three questions are addressed. Does the rapid heating rate effect the transition temperature at which ferrite transforms to other phases? How long are the dwell times above relevant transition temperatures? For example, even if the temperature exceeds the austenization temperature, is there sufficient time for austenite to form? And lastly, is there a rise in bulk temperature that reduces the effectiveness of the bulk as a heat sink? This project attempts to address these questions.

CHAPTER II

BACKGROUND

Steel's mechanical properties are a function of the solid microstructure. The various phases that comprise the microstructure are themselves determined by the alloy composition and thermal history. Assuming a constant composition, the thermal history is the determining factor in the microstructure formation. For this reason, a great deal of effort has and is being spent attempting to quantify the transient temperature field. An accurate model of the temperature field can be used to predict the mechanical properties of the steel.

This chapter describes what work has been done to bring us to the current state of the art regarding the prediction of the temperature field in laser materials processing. The first section describes the energy equation, the fundamental equation for calculating the thermal field. The second section describes various analytical solutions to the energy equation along with the assumptions used to derive them. Section 3 is a similar review of numerical solutions. Section 4 describes some of the experimental work done in laser surface heat-treating. The final section (5) shows some of the investigation into multitrack effects.

2.1 Energy Equation

If mass transport, via either diffusion or convection, is negligible, the temperature field can be calculated from the heat equation, which in general form can be written as:

$$\frac{\partial}{\partial t}[\rho h] = \vec{\nabla} \cdot k\vec{\nabla}T + Q \tag{2.1}$$

where T is the spatially and temporally varying temperature, ρ is the solid density, h is the enthalpy, and k is the thermal conductivity. Both ρ and k are, in general, functions of temperature. Q represents any source of energy that is added volumetrically to the material.

For a finite volume, three-dimensional region, any solution to the heat equation requires a boundary condition (BC) for each of the region's surfaces. A general form of the BC can be written as:

$$0 = -k\frac{\partial T}{\partial n}\bigg|_b + q_b'' \qquad (2.2)$$

where the n indicates the derivative is to be taken normal to the surface and the subscript b indicates values taken at the boundary. The term, q_b'', is the energy flux leaving the surface.

There are two distinct approaches used to solve this equation and its associated BC for laser material processing, depending on whether the energy from the laser beam is absorbed entirely at the boundary or appreciably penetrates into the volume. An example where such beam penetration is significant is in the medical industry, where lasers are used to process tissue and other biological material [6]. Except in the case of keyhole welding, however, absorption at the surface is acceptable for laser materials processing of solid metals.

In models that allow for beam penetration into the solid, the volumetric heat source in equation (2.1), Q is used to represent the beam, and is a function of both space and time since the beam has a specific power distribution and can move with respect to

the material. The energy flux leaving the surface in a beam penetrating type model usually includes convection and radiation (see Figure 2.1):

$$(2.3) \qquad q_b'' = h_t(T - T_\infty) + \varepsilon\sigma(T^4 - T_{surr}^4)$$

where h_t is the temperature dependent convective heat transfer coefficient, ε is the temperature dependent emissivity of the processed material, and σ is the Stefan-Boltzmann constant. T_∞ is the convection freestream temperature and T_{surr} is the temperature of the surroundings. In some instances, it may be appropriate to use an isothermal (T_b = const) or adiabatic ($q_b'' = 0$) BC.

When the laser beam is absorbed at the surface (see Figure 2.2), the equations can be written to incorporate the beam energy in the boundary condition. In this case, the volumetric heat source, Q, in equation (2.1) is zero, and the boundary energy flux in equation (2.2), q_b'', is written as

$$(2.4) \qquad q_b'' = h_t(T - T_\infty) + \varepsilon\sigma(T^4 - T_{surr}^4) - q''(x, y, z, t)$$

where q"(x,y,z,t) represents the energy flux from the moving beam. Equation (2.3) remains valid for any surfaces in which there is no beam flux. An exhaustive search through the literature suggests virtually all attempts to solve equation (2.1) in laser materials processing use one of these two forms.

2.2 Analytical Work

Analytical solutions to equation (2.1) certainly are useful, often serving as a first approximation and estimation to a problem, subject to the limitations required deriving

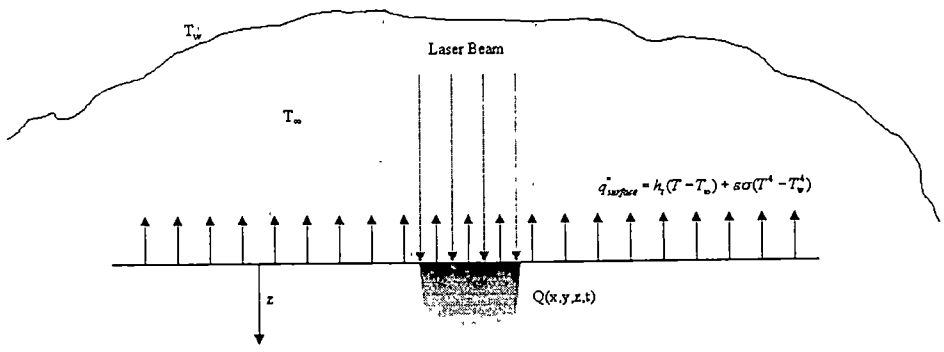


Figure 2.1: Schematic of a volumetric heat source.

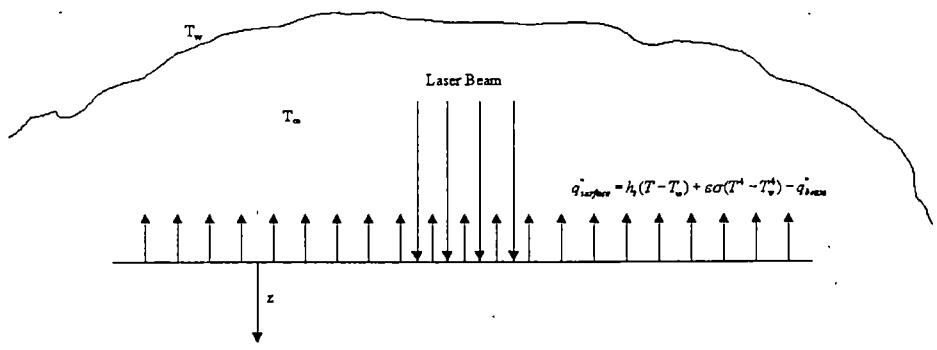


Figure 2.2: Schematic of a boundary heat source.

them. To be useful as such, however, the solution must be easy to use. As the reader that looks at the literature will see, only with a number of simplifying assumptions can analytic solutions be obtained. The fewer simplifying assumptions that are made, the more complex the resulting solution is.

Of the various analytic solutions that can be found in the literature, most differences between them arise from three different assumptions, in addition to whether the beam is modeled as a boundary or volume source. The first assumption is whether the thermal properties, primarily conductivity and specific heat, are constants or dependent on other properties (such as temperature). Virtually every analytic solution assumes density is a constant. The second assumption regards how the beam shape is modeled geometrically; most analytic solutions assume a Guassian beam shape since the associated mathematics is relatively easy. And lastly, an assumption with regard to the domain size and boundary conditions is made. Very few analytical models attempt to determine the thermal field in a finite size, three-dimensional region with appropriate boundary conditions. What follows is a brief review of what previous work has been done.

The first serious attempt at determining the temperature field in a solid with a moving heat source, whether as a volumetric or boundary source, is attributed to Rosenthal [7]. Modeling the source in the boundary conditions and assuming constant thermal properties and an infinite domain, a relatively simple result for the thermal field can be derived. A coordinate transformation, $\xi = x - v * t$, changes the unsteady heat transfer problem (from the perspective of an observer positioned at the origin fixed in the material) to a steady problem (from the perspective of an observer moving with the

beam). This "quasi-steady" state approach has been used repeatedly since Rosenthal's work in 1946.

Since the solution is simple and is used extensively by subsequent work, it is included here. Assume a point source is moving in an infinite medium, and the point source has a strength given by:

$$(2.5) \qquad q = \lim_{R \to 0} \left(-\frac{\partial T}{\partial R} 4\pi R^2 k \right) \qquad R = \sqrt{\xi^2 + y^2 + z^2}.$$

If the solid is initially at a uniform temperature, T_0, the resulting thermal profile, derived by Rosenthal is:

$$(2.6) \qquad T - T_0 = \frac{q}{4\pi k} e^{-\lambda v \xi} \frac{e^{-\lambda v R}}{R} \qquad \lambda = \frac{\rho c_p}{2k}.$$

Thus, in both time and distance, the temperature distribution changes exponentially from the point of the energy source. The major drawback, however, is that the solution predicts the temperature goes to infinity at the source, R = 0. This is, of course, a result of using a point source.

Cline and Anthony [8] have extended Rosenthal's work by using a Guassian beam, absorbed volumetrically, and Green's functions to superimpose the effect of individual point sources. Their solution involves numerous integrals and summations, and hence requires a computer for evaluation of actual temperature values. Virtually all solutions that use anything other than a point source are similarly complex.

Manca et al [9], use constant properties and a Gaussian boundary source, but solve the temperature field in a region with boundaries; the domain is finite in the

direction of the beam movement. Other similar works include those by Chaudrhy and Zubair [10-12], Chen and Lee [13], and Nissim et al [14].

Lax [15,16] allows for a temperature dependent conductivity by linearizing the energy equation through the use of a Kirchoff transformation. Specific heat is still assumed constant. The work by Moody and Hendel [17] is similar.

Ashby and Easterling [18] argue that a Guassian source, when scanning at high speeds, can be modeled as infinitely thin in the direction of beam movement. This additional simplification allows the integral solution of Cline and Anthony to reduce to a simple equation, given here:

$$(2.7) \qquad T - T_0 = \frac{Aq/v}{2\pi\lambda[t(t+t_0)]^{1/2}} \exp\left[-\frac{1}{4a}\left(\frac{z^2}{t} + \frac{y^2}{t+t_0}\right)\right], \qquad t_0 = \frac{r_B^2}{4a}$$

where T_0 is the initial temperature, A is the absorptivity, q is the beam power, v is the beam speed, λ is the thermal conductivity, a is the thermal diffusivity, and r_B is the beam radius.

All of the aforementioned works assume either an infinite or semi-infinite domain. A few authors have derived solutions that incorporate 3d boundary conditions for finite sized domains. Abou-Arab [19] assumes constant properties and a point source volumetric beam. Maier et al [20] utilize constant properties and both a rectangular tophat and Guassian beam shapes.

Kar and Mazumder [21] have perhaps the most complete analytical solution to the energy equation, allowing for temperature dependent thermal properties (both conductivity and specific heat, albeit in assumed form) and 3d boundary conditions.

They assume a constant initial temperature. Their solution is also the most complex and actual temperature values cannot be obtained without the use of a computer.

2.3 Modeling Work

Analytical solutions to equation (2.1) require simplifying assumptions to make them solvable. Modeling the heat transfer numerically removes most assumption requirements. In fact, modeling all the conservation equations (mass, momentum, energy, and species) becomes possible; current mathematics are insufficient to solve the non-linear, coupled conservation equations analytically.

Even when only the energy equation is important, i.e. during heat treatment where mass transport is negligible, a numerical solution has its advantages. For example, thermal properties can be functions of temperature, composition, wavelength, time, etc, depending on appropriateness. Beam absorption characteristics can be incorporated as functions of wavelength and temperature. The model can describe a finite size volume with physically realistic boundary conditions. And the beam geometry does not have to be modeled in a mathematically convenient form. True laser beams tend to have less ideal forms. A profile of a beam from a Nd:YAG laser is shown in Chapter V.

Another important advantage of using a numerical solution to the energy equation is in having the ability to use non-uniform initial conditions. Consider the case of heat treating the surface of a material using a focussed laser beam. The finite size beam moves across a region, heat treating a "track" of a measurable width. After moving some distance, the beam is offset an amount less than the width of the track and the process is repeated. Unless sufficient time is allotted between successive tracks, the temperature

field prior to the second and successive tracks will not be uniform. Additionally, even though laser processing is frequently referred to as a "quenching" process, owed to the very high cooling rates experienced, the cumulative effect of a large number of tracks can produce bulk heating, depending on the boundary conditions used. These two points are of great interest to this body of work. How do previous heat treatment tracks influence the microstructure formation on subsequent heat treatment? In none of the following reviewed works does this question appear adequately addressed.

Numerical models of laser processing are well represented in the literature, and as with the analytic solutions, different authors make different assumptions regarding beam geometry and thermal properties. Abou-Arab et al [22] use a finite difference scheme to solve the three-dimensional heat transfer problem with a volumetric point source/sink and constant thermal properties. Erhard et al [23] use finite element to model a rectangular tophat, boundary condition type heat source. The domain is finite in y and z, but infinite in x. Convection and radiation are neglected from all surfaces except the bottom. Mazumder and Steen [24] also use an infinite length domain in the direction of beam movement (having also transformed the problem into quasi-steady state) and a boundary condition heat source, but they incorporate convection and radiation losses from the sides. They also use thermal properties that are independent of temperature.

Manca et al [25] also use an infinite x domain with the beam modeled in the convection/radiation boundary condition. Additionally, they allow for temperature dependent conductivity and specific heat. They also use a variety of beam shapes, including rectangular, Guassian, and donut shaped. Kou et al [26] use a rectangular tophat beam with temperature dependent properties, but assume semi infinite extent.

Michaleris and DeBiccari [27] numerically solve the heat equation in a two-dimensional region, but use temperature dependent thermal properties. In addition, they have artificially increased the conductivity at temperatures above melting to account for the additional heat transfer that occurs during convection.

Several authors model the full set of conservation laws (mass, momentum and heat transfer), although generally only in two dimensions. Pirch et al [28], Chan et al [29], and Thompson and Szekely [30] all use two-dimensional domains with constant transport properties. Surface tension effects on convection in melt regions are included.

2.4 Multitrack work

The influence of individual processing tracks on subsequent heat-treating is critical since it affects the thermal field. However, this appears to be largely ignored in the literature, although Maier et al [20] examine the influence somewhat. Using Green's functions, they determine the three-dimensional temperature field in a rectangular region while processing. They assume constant thermal properties and neglect all phase change effects and surface heat losses. Between tracks, they use finite differencing (numerical) to calculate the transient temperature field when there is no absorption of energy. While not explicitly stated, it appears from the figures that the finite difference scheme is used to spread the energy distribution, calculated analytically, uniformly throughout the volume. This uniform bulk temperature is then used as the initial condition for the next track.

Beyond this, there appears to be very little in the literature regarding multitrack effects. The Maier et al work [20] does not account for temperature dependent

properties, phase transition, or include realistic lossy boundary conditions. Also, the use of a uniform temperature distribution prior to each processing track is what would be expected when there are long periods of time between tracks; short periods would leave a non-uniform temperature distribution prior to subsequent tracks.

CHAPTER III

THEORY

This chapter details the equations that are solved in subsequent chapters. The first section describes the enthalpy equation and appropriate, three-dimensional boundary conditions used in the numerical model. Section two gives the relation between enthalpy and temperature for use when the specific heat is a function of temperature. Section three gives relations for determining the hardness of various steel phases using the cooling rate calculated numerically.

3.1 Model

The energy equation and associated boundary conditions for a Cartesian system are described here. The actual numerical implementation of these equations is described in Chapter 4.

The domain of interest is a rectangular solid with (x,y,z) dimensions of (L,W,H) respectively. The laser beam is aligned in the –z direction and impinges the solid on the top at z = H. The beam moves in the +x direction with a speed V. Figure 3.1 depicts this scenario.

In Cartesian coordinates, the enthalpy equation, eq (2.1) can be written as

$$\rho \frac{\partial h(T)}{\partial t} = \frac{\partial}{\partial x}\left[k(T)\frac{\partial T}{\partial x}\right] + \frac{\partial}{\partial y}\left[k(T)\frac{\partial T}{\partial y}\right] + \frac{\partial}{\partial z}\left[k(T)\frac{\partial T}{\partial z}\right]. \tag{3.1}$$

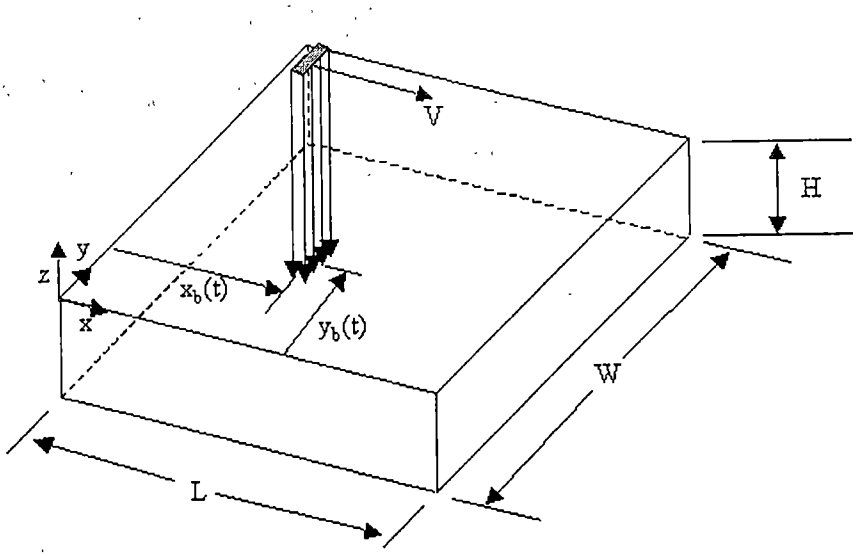


Figure 3.1: Laser heat treating domain of interest.

The boundary conditions, which include convective and radiative losses, are

$$(3.2)\quad 0 = -k(T)\frac{\partial T}{\partial x} + h_t(T - T_\infty) + \varepsilon\sigma(T^4 - T_w^4) \qquad @\ x = 0$$

$$0 = k(T)\frac{\partial T}{\partial x} + h_t(T - T_\infty) + \varepsilon\sigma(T^4 - T_w^4) \qquad @\ x = L$$

$$0 = -k(T)\frac{\partial T}{\partial y} + h_t(T - T_\infty) + \varepsilon\sigma(T^4 - T_w^4) \qquad @\ y = 0$$

$$0 = k(T)\frac{\partial T}{\partial y} + h_t(T - T_\infty) + \varepsilon\sigma(T^4 - T_w^4) \qquad @\ y = W$$

$$0 = -k(T)\frac{\partial T}{\partial z} + h_t(T - T_\infty) + \varepsilon\sigma(T^4 - T_w^4) \qquad @\ z = 0$$

$$q''(x,y,t) = k(T)\frac{\partial T}{\partial z} + h_t(T - T_\infty) + \varepsilon\sigma(T^4 - T_w^4) \qquad @\ z = H$$

where q"(x,y,t) is the energy flux from the moving beam.

For a rectangular tophat beam (Figure 3.2), with a beam power P(t), absorptivity (α), depth $2x_r$, and width $2y_r$, q"(x,y,t) can be written as

$$(3.3)\quad q''(x,y,t) = \frac{\alpha P(t)}{4x_r y_r} \qquad |x - x_b(t)| < x_r \quad \textit{and} \quad |y - y_b(t)| < y_r$$

$$= 0 \qquad \textit{otherwise.}$$

where $x_b(t), y_b(t)$ is the position of the center of the beam, which changes with time. For an elliptical Gaussian beam (Figure 3.3) with power P(t), radii to the 1/e points in x and y given by x_r and y_r respectively, the energy flux can be written as

$$(3.4)\quad q''(x,y,t) = \frac{\alpha P(t)}{\pi x_r y_r}\exp\left\{-\frac{[x - x_b(t)]^2}{x_r^2} - \frac{[y - y_b(t)]^2}{y_r^2}\right\}.$$

P(t) is a function of time since the beam may be turned off between tracks for a period of time Δt.

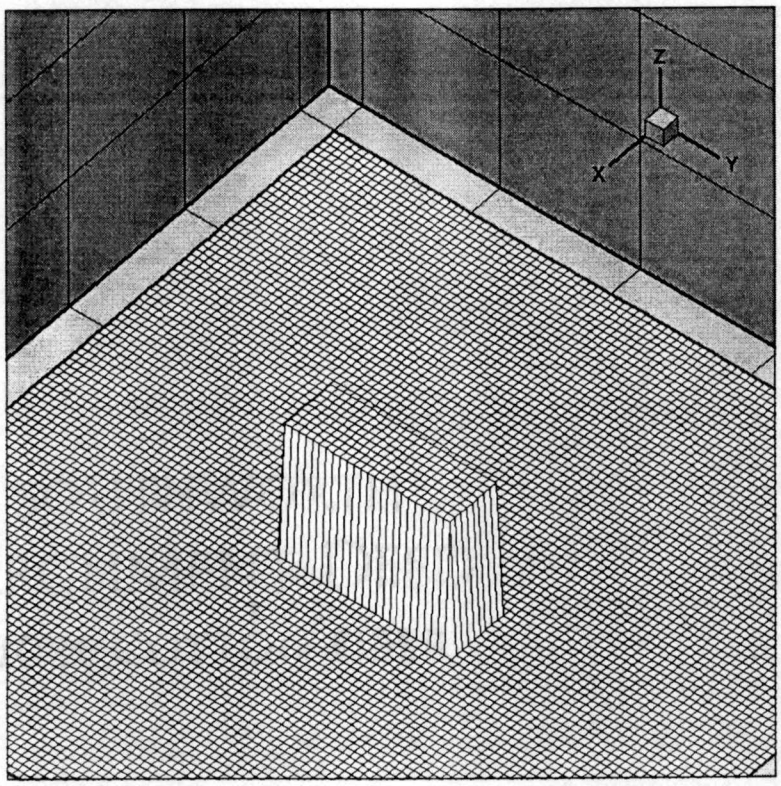


Figure 3.2: A rectangular tophat beam profile.

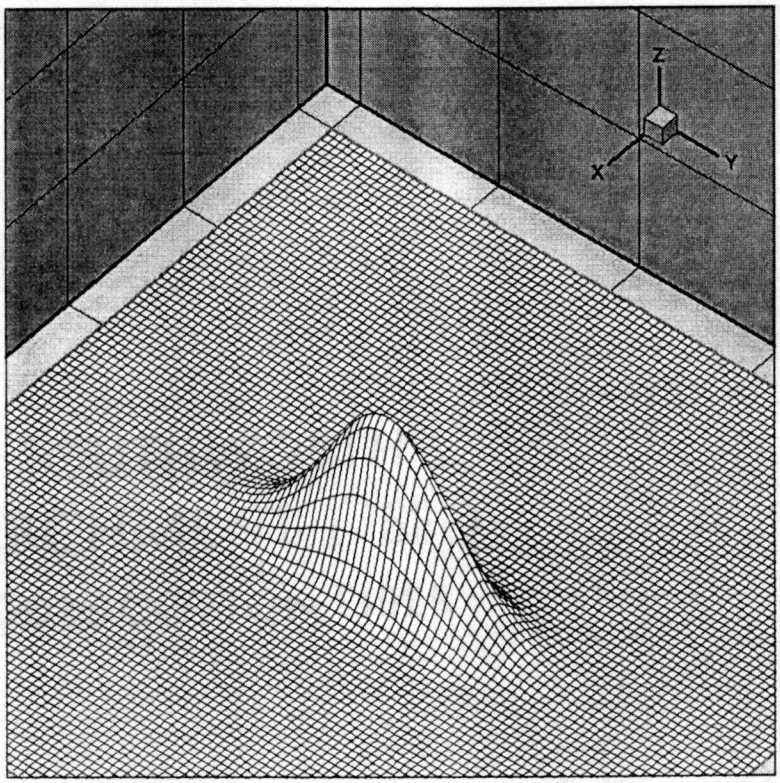


Figure 3.3: An elliptical Guassian beam profile.

The beam is moving in the x direction with a constant speed (V), and processes for a distance l_p. The total time (t_1) for a single, complete track is simply

$$t_1 = \frac{l_p}{V} + \Delta t \tag{3.5}$$

and the integer number of completed tracks is

$$n = INT\left(\frac{t}{t_1}\right) \tag{3.6}$$

Define the time into the current track to be

$$t^* = t - nt_1 \tag{3.7}$$

Then P(t), which has a nominal, "on" value of P_0 can be written simply as

$$P(t) = P_0 \qquad 0 \le t^* < \frac{l_b}{V} \tag{3.8}$$

$$= 0 \qquad \frac{l_b}{V} \le t^* < t_1.$$

Finally, we can calculate the position of the beam using

$$x_b(t) = x_{b0} + Vt^* \tag{3.9}$$

$$y_b(t) = y_{b0} + n\Delta y$$

where Δy is the offset in the y direction between each track and x_{b0},y_{b0} is the position of the beam at t = 0. Depending on the beam profile, either equation (3.3) or (3.4) and equations (3.5) through (3.9) can be used to solve the enthalpy equation and its boundary conditions, equations (3.1) and (3.2) numerically.

3.2 Thermal Properties

The enthalpy equation, equation (3.1), and its boundary condition, equation (3.2), have three thermodynamic properties; density (ρ), conductivity (k), and specific heat (Cp). In general, all three may vary with temperature. For this project however, only the specific heat and conductivity are variable; the density is assumed constant.

Enthalpy is related to temperature via the equation

$$h(T) = h(T_0) + \int_{T_0}^{T} C_p(\overline{T})\, d\overline{T} \tag{3.10}$$

where at $T_0 = 0$ K, $h(T_0) = 0$.

3.3 Heat Treat Physics

Heat treating low carbon steels is a two step process. First the base steel is heated to a temperature above a transition temperature to form a different phase (austenite, for example, a necessary precursor to forming martensite). The second step involves cooling the material. For example, below the martensite start temperature, austenite may transform into martensite.

Traditionally, the first step is performed isothermally. That is, the steel is placed in a furnace at a constant temperature for a period of time, during which two things occur. Above the austenization temperature, for example, the base material structure begins to transform to austenite. After the base is completely changed, the austenite grains begin to enlarge, resulting in fewer grains. For a steel with 0.8% carbon content, complete austenization occurs at 860 degrees C in about 100 seconds [31]. For commercial purposes, there is little reason to austenitize at higher temperatures, which contributes to increased oxidation.

In the second step (same example), the material is cooled to a temperature below the martensite start temperature. The cooling may be done isothermally, in which the material is quenched to a predetermined temperature then held there during the transformation of martensite from austenite, or it may be done continuously, during which the transformation occurs at different temperatures. For either case, cooling curves exist that can be used to predict the final phase composition. Figure 3.4 gives the isothermal transformation diagram for 1050 steel. Figure 3.5 gives the continuous cooling transformation diagram for 1040 steel. Although 1050 has a higher carbon content, for qualitative purposes the critical cooling rates for which martensite forms are of the same order of magnitude.

With laser materials processing, the control of the process is different than with traditional methods. Since the heat is applied at the surface only, a thermal field with spatial gradients is established. During the transformation of the base material's initial phase into something different, the material is continuously heated, rather than held at a constant temperature. Additional transformations (martensite from austenite, for example), occur while the material is continuously cooled. The forward transformation represents a significant difference from traditional heat-treating.

In addition, with traditional heat treating, the heating rate is known to influence the temperature at which ferrite transforms to austenite [32]. Figure 3.6 shows the heating rate influence on this temperature for pure iron. Figure 3.7 shows a more pronounced influence for a steel with 0.80% carbon content.

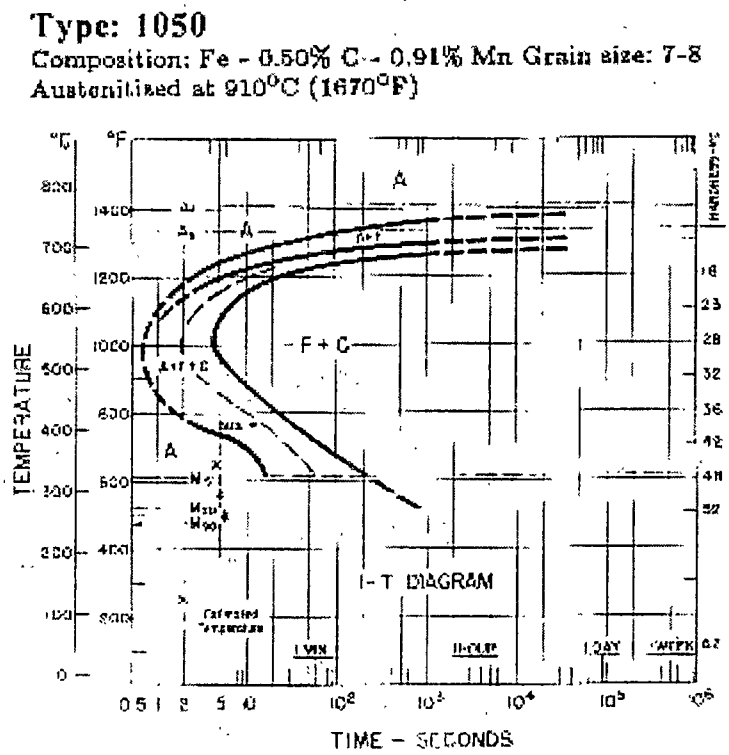


Figure 3.4: Isothermal Transformation diagram for 1050 Steel. (Source: Atlas of Time-Temperature Diagrams for Irons and Steels. G.F. Vandervoort, ed. ASM International: Materials Park, OH 1991)

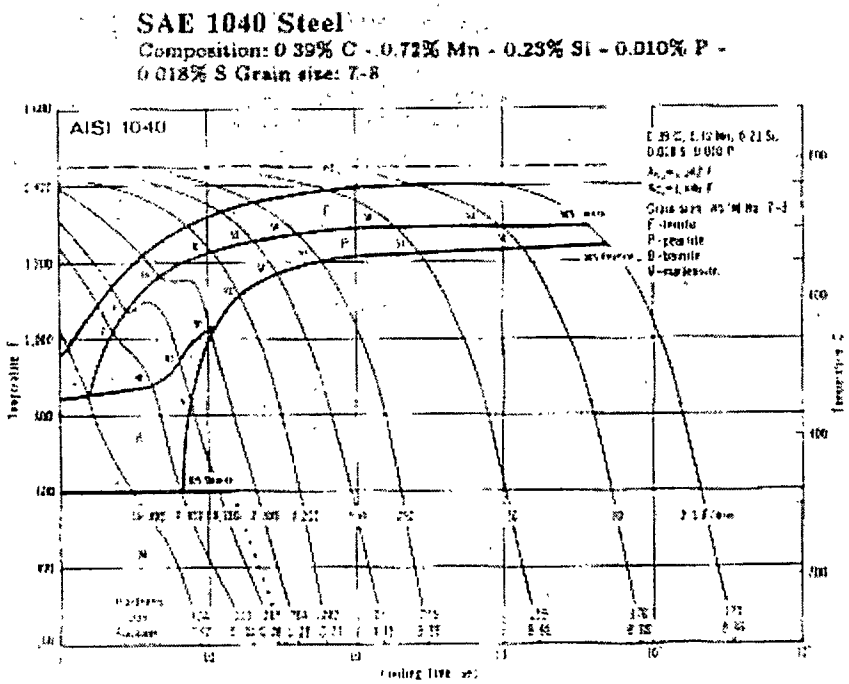


Figure 3.5: Continuous Cooling Transformation diagram for 1040 steel. (Source: Atlas of Time-Temperature Diagrams for Irons and Steels. G.F. Vandervoort, ed. ASM International: Materials Park, 1991)

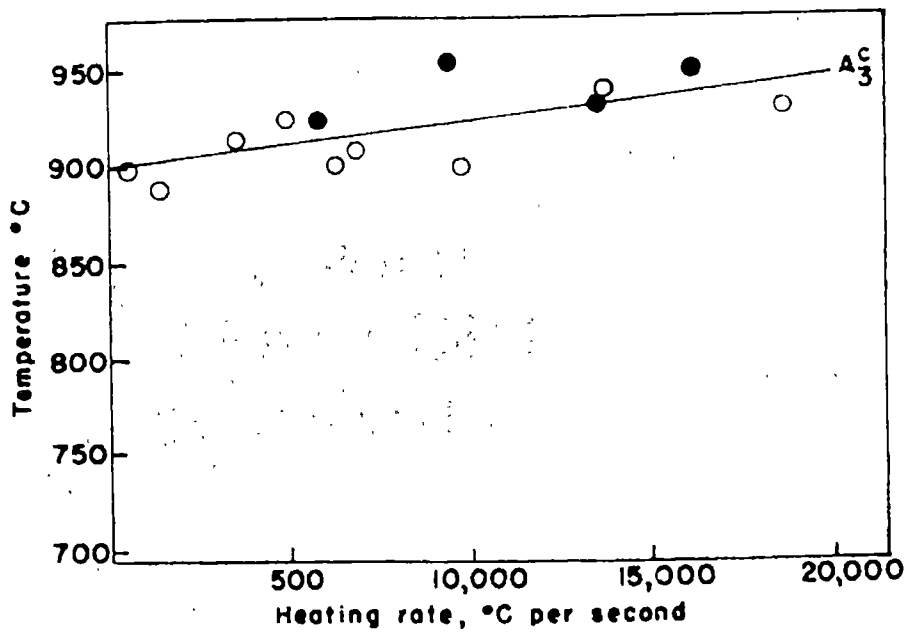


Figure 3.6: Effect of heating rate on the temperature at which ferrite transforms to austenite in pure iron. (Source: Brooks, CR. Prinicples of the Heat Treatment of Plain Carbon and Low Alloy Steels. ASM International: Materials Park, OH 1996)

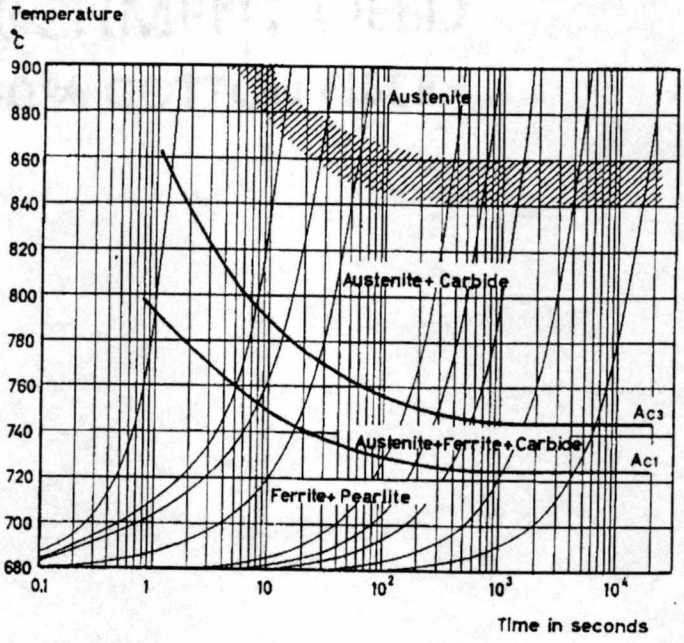


Figure 3.7: The effect of heating rate on the temperature at which austenite forms in steel with 0.8% carbon content. (Source: Brooks, CR. Prinicples of the Heat Treatment of Plain Carbon and Low Alloy Steels. ASM International: Materials Park, OH 1996)

CHAPTER IV

MODEL

This chapter describes the computer model used to calculate the time dependent temperature field that exists while laser heat treating steel. The commercial code, CFD-ACE v4.0 (CFD Research Corporation) was selected to perform computations. Hereafter, any reference to "model" or "code" refers to this software.

Using a commercial code entails both a major advantage and disadvantage when compared to composing a code from first principles. The advantage is the generic nature of the commercial code enables it to be used in a much wider class of applications, including more complex laser processing than is employed here. A major disadvantage is the decrease in computation speed due to the overhead inherent in the commercial code since not all of the commercial code's functionality will be employed. The decision to utilize a commercial code was ultimately based on the desirability of future research to build on this work when incorporating melting and vaporization into the problem.

The commercial code used, CFD-ACE, uses a conservative, control volume approach in solving the governing equation (enthalpy) [33]. The conservative approach is a major advantage in the accuracy of modeling a process that has inherently large thermal gradients [34].

4.1 Sample Preparation and Experimentation

The intent of the model in this project is to simulate laser heat treating on AISI 1050 steel coupons. In this and later chapters, comparison between modeled and laser

heat treated results will be made. For this reason, it is necessary to identify the steps done for the experiment. Both sample preparation and experimentation parameters are identified. Unless otherwise specified, any reference to experimental results refers to materials and equipment described here.

The material used in the research is AISI 1050 steel. As received from the manufacturer, this material comes as large sheets, ¼" thick and several feet per side. The sheets are cut at the University of Tennessee Space Institute's machine shop into smaller pieces, generally either 1" square or 3" x 6" (the particular size used will be identified as needed). The smaller pieces are then sandblasted to remove the grime and any oxidation that exists as received from the manufacturer.

When processing, a Hobart HLP 3000 Nd:YAG laser with a fiber optic beam delivery is used. The optics' motion is controled using a Techno motion controler system. This system enable the user to specify distance, speed and direction parameters during processing.

Once laser processing is complete, a cross section of the sample is obtained by cutting the material on LECO CM20 and Mark V CS600-A cutting blades (for rough and fine cuts respectively) and mounted using a Buehler Pneumet I mounting press. The mounted samples are then sanded (up to 800 grit sandpaper) and polished (using 0.1 micron Alumina suspension polishing compound) to a mirror finish. A 30 second etch in 5% Nital etching solution shows the resulting HAZ, pictures of which were taken using a digital frame grabber.

4.2 CFD-ACE

Getting a solution to a problem using CFD-ACE generally involves three preliminary steps; creating the grid, defining the boundary conditions, and setting the run conditions (establishing the number of iterations to run and the time step size for example). The solver is then run, generating a solution for each time step.

The CFD-ACE commercial package includes three different modules: GEOM, used to generate grids; GUI, used to establish the boundary, initial, and run condition values and initiate the solver; and VIEW, used to examine the resulting data files. CFD-ACE uses a proprietary data file for storing grid and solution information, so an additional module, DTF, is available that includes program subroutines (Fortran and C) for extracting information from the data file into a user's own programs.

The typical procedure for using CFD-ACE in this project is:

1) Use GEOM to
    a) Create the grid.
    b) Specify what the volume contained within the grid is (in this case solid; however CFD-ACE is a computational fluid dynamics solver so the volume could be a fluid as well).
    c) Specify the boundary types (wall, thin wall, inlet, or outlet for ex. – note that values are set using GUI).
    d) Export the grid to a file. The exported grid uses a "dtf" extension, not to be confused with "DTF", the set of subroutines used to extract information from the "dtf" file.
2) Use GUI to:

a) Import the grid stored in the dtf file.

b) Specify the kind of solution to be performed (heat transfer for example).

c) Specify property values (density, conductivity and specific heat; the last two may be constants, algebraic, or piecewise linear).

d) Specify boundary conditions. For a heat transfer only problem with wall boundaries, the boundary conditions may be adiabatic, isothermal, constant heat flux, or a combination of convective and radiative loss.

e) Specify the initial conditions.

f) Specify the number of time steps and time step size and how often to store results.

g) Specify the number of iterations per time step.

h) Specify which results to store (temperature and enthalpy for example).

i) Submit the model to the preprocessor which prepares the model for the solver. In addition, this step generates a user modifiable input file.

Once these are complete, the last thing to do is submit the model to the solver, which starts the calculation process in motion. Results, when complete, can be analyzed using VIEW.

However, while the available boundary conditions are suitable for the four sides and the bottom of the processed sample, a modification to the solver is necessary in order to model the beam as anything other than a uniform flux on the upper, processed surface.

4.3 Boundary Conditions

The boundary conditions are set using GUI. For each of the six surfaces, both a type (adiabatic, isothermal, etc) and a value for that type are set. For boundaries that include radiation losses the surface emissivity is required. Emissivity is a complex function of many variables, including wavelength, temperature, material, and surface condition. The boundary condition definition within GUI however, requires only a value for the total emissivity and a background temperature. Therefore, an estimate of the surface emissivity is necessary. Similarly, for any boundary that includes convection losses, which are a complex function of flow speed and composition, material and geometry, GUI requires a simple values for the convection heat transfer coefficient and freestream temperature. However, in the case of convection, a cover gas was not used during processing. The only flow is naturally occurring, buoyancy driven due to slight density changes in the air surrounding the sample. An accepted value for a natural convection coefficient is 10 W/m^2K [35].

Reviewing several different sources for iron and steel emissivities, the surface condition has the biggest effect on emissivity. Omega engineering [36] gives values ranging from 0.74 to 0.95 for oxidized iron, 0.05 to 0.21 for unoxidized iron, 0.08 for unoxidized steel and 0.8 for oxidized steel. For polished steel, Omega reports an emissivity ranging from 0.07 to 0.14. Wade [37] reports for AISI C1020 steel emissivities of 0.2 for unoxidized and 0.8 to 0.9 for an oxidized surface. Electro-Optical [38] reports values of 0.14 to 0.38 for polished iron and 0.81 for oxidized iron. For polished stainless steel, they report an emissivity of 0.11. For stainless steel where the surface has been sandblasted, they give an emissivity of 0.38. Since the AISI 1050 samples used in this

project were sandblasted prior to processing, an emissivity of 0.4 was used in the model. The temperature of the surroundings was assumed to be room temperature, 293K.

Along the top surface, in addition to the emissivity for radiation losses, it is also necessary to know the spectral absorption coefficient for 1.06 microns (Nd:YAG wavelength) acting on AISI 1050 steel. Rather than relying on literature values which similarly vary depending largely on surface condition, an experimental and iterative numerical procedure was used to estimate the spectral absorption coefficient, similar to the calibration used by Frewin and Scott [39].

Using a constant delivered beam power (800 W), individual tracks were processed on 3" x 6" pieces of AISI 1050 steel (initially sandblasted to provide a clean surface) at different beam translation speeds such that the beam speed at which the material begins to melt at the surface is determined (6500 mm/min). This set of conditions was then modeled iteratively, changing the absorption coefficient and beam geometry each iteration, until both the surface reached melting temperature (1900 K) and the depth of the 1000 K isotherm corresponded to the HAZ profile of etched samples from the experimental work. This procedure yielded an estimate for the spectral absorption of 0.49.

Summarizing, along the four sides and top the convection heat transfer coefficient is 10 W/m^2K with a freestream temperature of 293 K. The emissivity is 0.4 with a surrounding temperature of 293 K. Additionally, the spectral absorption coefficient for the beam interacting with the top surface is 0.49.

For the bottom of the sample an approach similar to what Winkler [5] used is employed. Since the sample sits on a copper plate, which consequently has its own

thermal field, rather than using an isothermal boundary condition (BC), a convection BC with a high convection coefficient (500 W/m^2K) is used and 293 K "freestream" temperature. As a practical matter, for the amount of energy absorbed in the sample in this work, the temperature field is not sensitive to different heat transfer coefficients on the bottom surface. This should not be expected to be the true for problems of greater duration and higher energy absorption (a melting problem for example) in which bulk heating is far more apparent.

For the top surface, the boundary includes both incident flux and convective and radiative losses (eq 3.2, z=H). CFD-ACE does not have the ability to apply a non uniform incident flux, such as an incident beam, within GUI. Fortunately, CFD-ACE is flexible in allowing the user to define complex boundary conditions by modifying the flow solver and making changes to the input file. These are described later (sections 4.5 and 4.6 respectively).

4.4 Thermophysical Properties

Solving the enthalpy equation requires three property values, density, conductivity, and specific heat. Specifying these properties must be done within GUI, however values may be altered within the input file once it is created. Although all three properties may be temperature dependent, CFD-ACE v4.0 does not incorporate the use of non constant densities when modeling solids. Conductivity and specific heat, on the other hand, are permitted to vary with temperature. The temperature dependence can be specified either in a polynomial relation or, as was used in this project, in tabular form. The thermophysical properties of AISI 1050 steel are desired. For this reason, the density

used is 7840 kg/m^3. Figure 4.1 shows the thermal conductivity and specific heat as a function of temperature [40].

4.5 Solver Modification

The CFD-ACE solver by default works with uniform boundary conditions (BCs), i.e. isothermal, constant flux, or convection and/or radiation loss. A large class of problems can be studied with such BCs; however for a moving laser beam (a flux type boundary condition), this is not sufficient.

CFD-ACE anticipates the difficulty in working with a limited and generic model and provides a selection of user accessible subroutines for modification. One user accessible subroutine allows the user to define very complex boundary conditions that are otherwise impossible to set from within GUI. Users program their own modifications and recompile the subroutines with the standard flow solver to create a modified flow solver. Then, after completing the steps listed above, the user makes appropriate changes to the input file and runs the model using the modified solver. Modifications to the input file include specifying the beam processing parameters (beam power, geometry, translation speed, and overlap index) and changing the default boundary condition type (constant flux) to "user_defined". By changing to "user_defined", the solver knows to use the user defined boundary condition subroutine for that surface.

Appendix A gives a detailed listing of the user defined subroutine used in the project. The modified solver uses values from the input file to determine the laser energy distribution at different times.

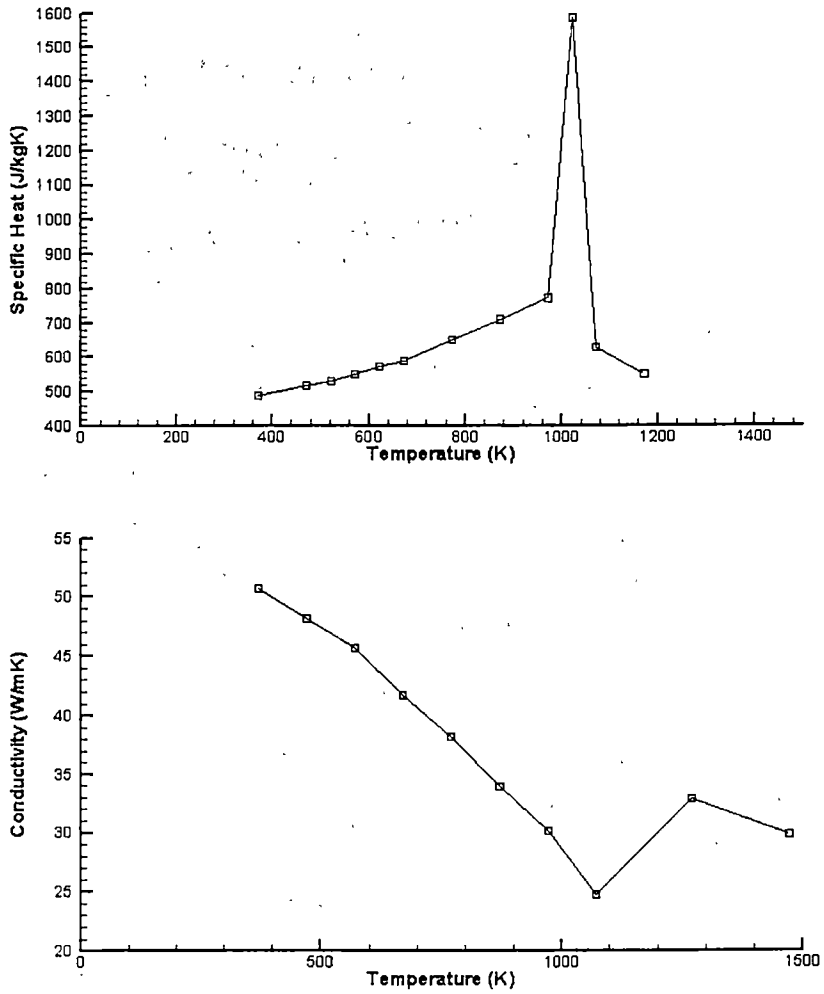


Figure 4.1: Thermophysical properties for AISI 1050 steel. (Source: MAPP Software, ASM International: Materials Park, OH)

4.6 Input File Modifications

There are two primary modifications to the input file necessary to make it work with the modified solver; the inclusion of 2 sections to the input file not generated by GUI and a change to the boundary condition on the processed side from "constant flux" to "user_defined".

Of the two additional sections, the first establishes a number of user understandable parameters that can be changed depending on the desired processing parameters chosen for each run. The parameters include beam power, beam geometry, processing speed, overlap index, convective and radiative properties, and the spectral absorption coefficient. The second section passes the parameters defined in the first into the solver through the use of real and integer arrays.

By changing the flux boundary on the top surface from a nominal constant to "user_defined", the input file instructs the solver to reference the boundary condition modifications described in section 4.5 above.

Appendix B lists a typical input file generated by GUI along with the modifications that are necessary to make it work with the modified flow solver.

4.7 Grid Generation

Although it was anticipated that, due to the steep thermal gradients expected, a grid with very fine resolution would be necessary, practical considerations prevent the user from creating a fine resolution grid without considering the negative influence. The domain size of the grid must be large enough that physical samples can be processed for

comparison purposes. The grid must fit with computational limits (memory and disk storage). And lastly, the grid itself must not influence the calculations.

The physical domain size selected is 25 mm square, 6 mm thick. 25 mm square was considered small enough for modeling purposes, and yet large enough that handling, mounting, and instrumenting were not overly delicate.

The computer used for modeling, currently a low end machine (Intel Pentium Pro 200 MHz machine with 2 CPUs) has 256 MB of memory and 12 GB of disk storage. After trial and error, it was determined that a CFD-ACE grid with 250,000 nodes consumes 6 MB of disk space (grid and default solution variables alone; additional solution variables increases the storage requirement). Moreover, while running, this size grid consumes about 220 MB of memory which, allowing for operating system overhead, represents an upper limit that is small enough to prevent the operating system from resorting to disk swapping. Disk swapping is a significant detriment to running speed since hard disks are typically an order of magnitude slower than memory in access speed.

With these constraints in mind, its necessary to determine how to distribute grid points within the model domain that results in an accurate solution. The simplest way to distribute grid points would be uniformly in all directions which, using 250,000 grid points would produce a cell spacing of just over 250 microns. However, such an approach is unacceptable for several reasons. It fails to take advantage of the fact that in areas far from the beam's track, the thermal gradients and rates of change are unlikely to be high, an indication that the cell spacing can be larger than in regions near the beam's track. It also fails to account for the possibility that the beam size might be unresolveable at that resolution. And finally, a finer grid resolution within the heat-affected zone is

required to accurately locate the HAZ boundary. For these reasons, an examination of the influence on grid spacing was done.

Flux boundary conditions must be uniform within a cell, so the smallest variation in flux that can be applied to a boundary is determined by the cell size. A 5 mm x 5 mm cell surface is unable to resolve a 1mm x 4 mm beam. Hence, any grid that attempts to incorporate the beam shape must have cells smaller than the beam shape. The smaller the grid spacing (the distance between two grid cell centers) the better the beam shape is resolved.

Additionally, the numerical solution to the enthalpy equation (and indeed the numerical solution to any differential equation) uses a differencing scheme that approximates derivatives. For example,

$$\frac{\partial T}{\partial x} \approx \frac{T(x+\Delta x)-T(x)}{\Delta x} \tag{4.1}$$

is an approximation for the partial derivative of T with respect to x. The approximation increases in accuracy as Δx decreases. In the limit as Δx approaches zero, the approximation approaches the formal definition of a derivative.

Both of these aspects (resolving the beam and improving the differencing approximation accuracy) are important and can be improved using small cell spacings. Very small cell spacings however, increase the total number of cells in the model and increase the computation time since equations are solved for each cell. So while small cell spacings are desirable for the reasons discussed above, using small cell spacings slows down the computation time.

To determine the largest cell spacings that yield accurate solutions, a series of test models were performed in which only the cell spacing in the processing direction was varied (cell spacings transverse to the processing direction were made small). The processing conditions for the series includes a beam power of 800 watts, a rectangular tophat beam profile 0.75 mm wide (in the same direction the beam moves while processing) by 4.50 mm long and a processing translation speed of 6500 mm/min. These are the same conditions found in section 4.2.

Figure 4.2 depicts the temperature profile at the surface of the sample and in the center of the beam after 0.12 seconds of processing. At positions away from the beam, the profiles agree with each other. However the peak temperatures are different, as indicated in Figure 4.3. Beyond a grid ratio (beam width divided by grid spacing) of about 5, the change in peak temperature is marginal (less than 5% change) with an increase in the number of cells within the beam (decreased cell spacing).

Based on these runs, the grid points were distributed as shown in Figure 4.4. The number of nodes in the x direction is 251, and the spacing is a constant 0.10 mm. In the y direction, the spacing was varied to increase the number of points in and near the beam tracks, where the thermal gradient is high. A total of 62 points are distributed across the width of the sample. In the vicinity of the beam edge, the spacing is as small as 0.15 mm. Away from the beam, the spacing grows as large as 2.00 mm. In the z direction, the nodes are spaced closest at the surface and further apart near the bottom of the sample. At the surface, the spacing is 0.03 mm; at the bottom the spacing is 2.00 mm. Figures 4.5 and 4.6 depict different surfaces of the grid.

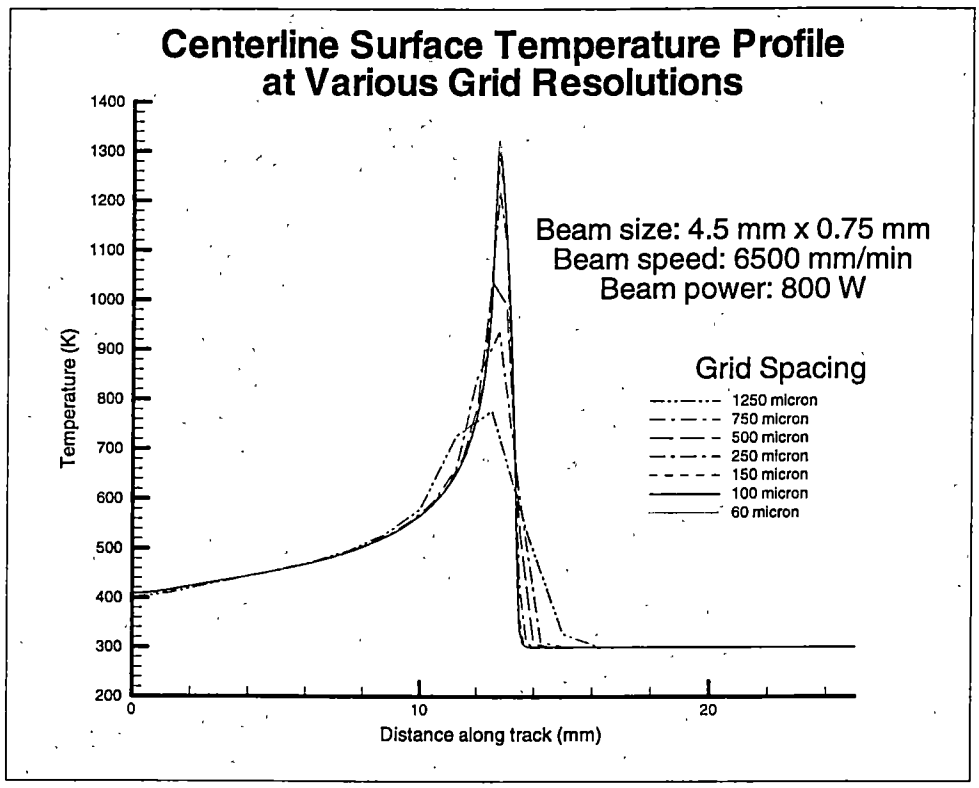


Figure 4.2: The influence of grid resolution on the resulting surface temperature profile at the center of the track.

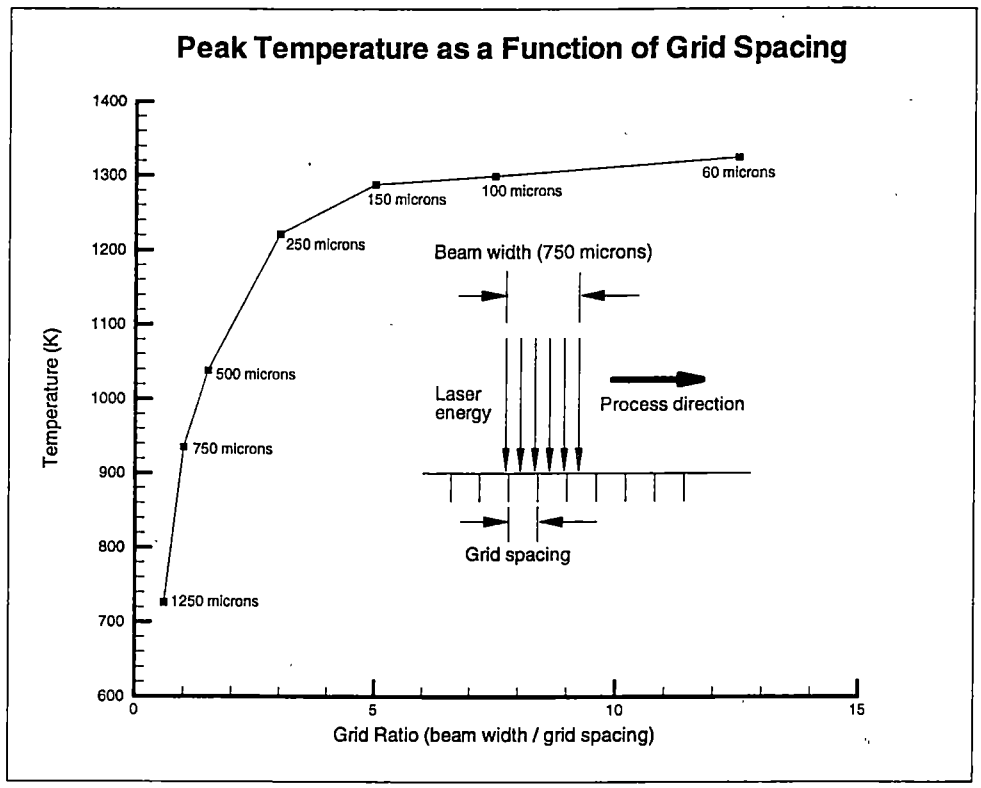


Figure 4.3: The influence of grid spacing on the peak temperature at any point on the surface. The processing conditions are 6500 mm/min beam speed, 800 W beam power, and 4.5 mm x 0.75 mm rectangular tophat beam profile.

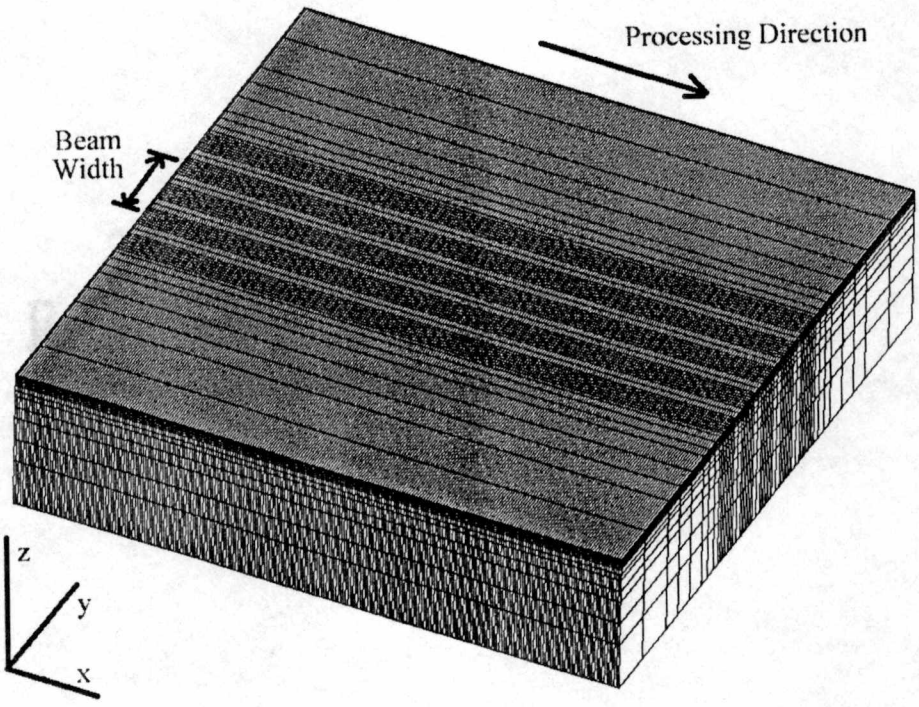


Figure 4.4: Orthographic view of the model grid depicting how the grid spacing varies spatially. The modeled domain size is 25 mm long by 25 mm wide by 6 mm high.

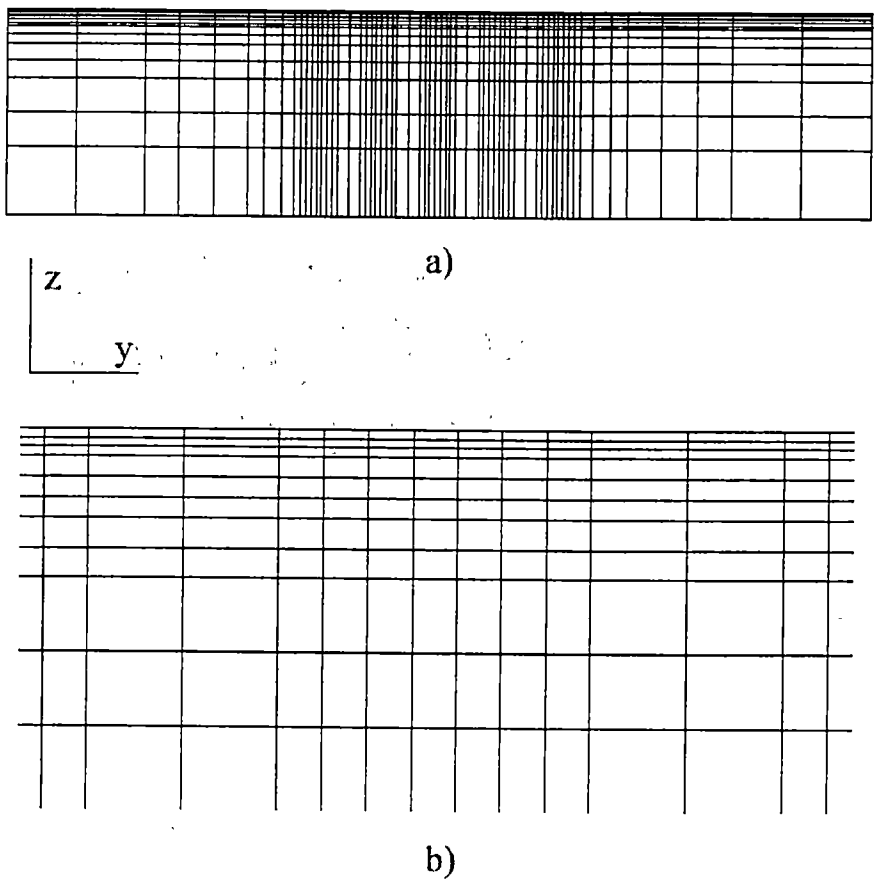


Figure 4.5: Side view of the model grid. Cell spacing varies in both the y and z directions. a) The cell spacing in the y direction is designed such that the beam edges fall within regions of smallest cells, where the spacing is 0.15 mm. b) An exploded view showing the cells near the surface, where the smallest cell spacing in the z direction is 0.03 mm. Half of the grid points in the vertical direction are positioned within 0.5 mm of the top surface.

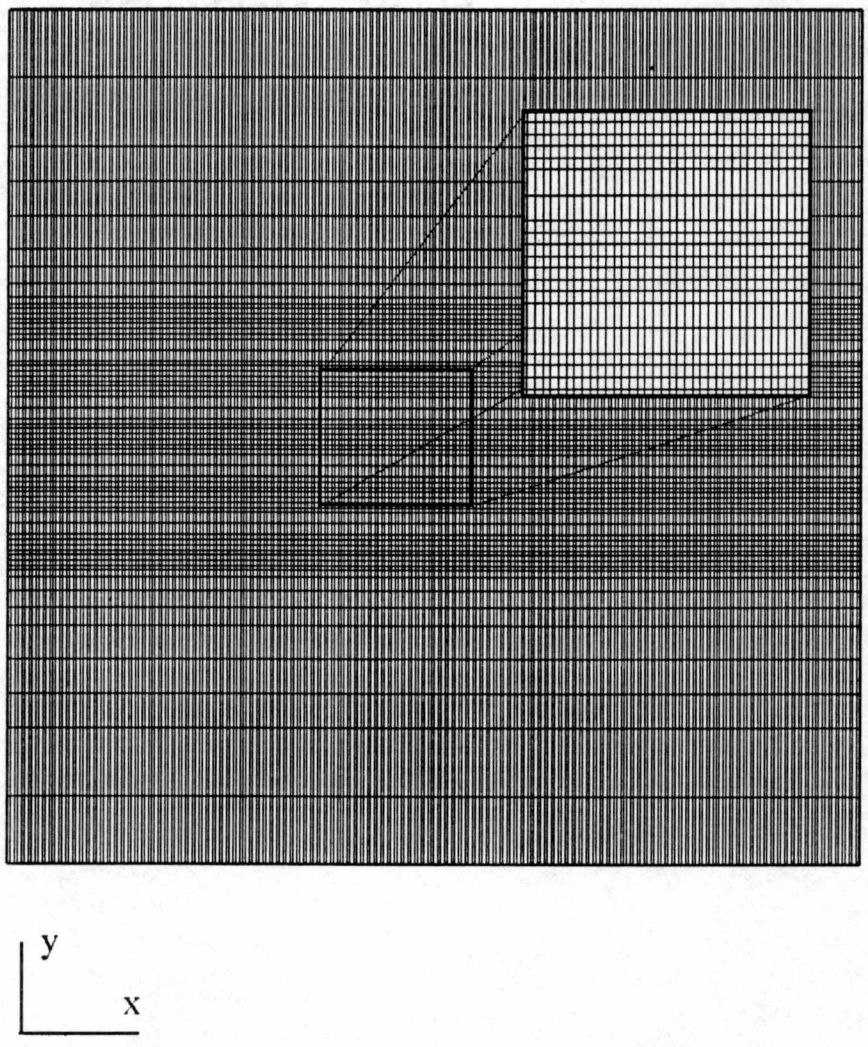


Figure 4.6: Top view of the model grid. The grid spacing is a constant 0.1 mm in the x direction and varies from 0.15 mm (exploded inset) in the "tracks" to 2.0 mm at the model edge in the y direction.

4.8 Timestep Determination

Similar to the grid spacing, the temporal spacing (time step size) is critical to the model solution as well. As with spatial coordinates, the numerical approximation to derivatives with respect to time is dependent on the time step size, Δt. There are several considerations for which the time step size is critical.

First, based on measured transient thermal profiles, the time rate of change of temperature, both heating and cooling, at any point as the beam passes through is high (see sec. 4.8). Large time steps will preclude capturing the transient response of temperature changes. In order to resolve these changes a small time step is required.

Second, the boundary condition for the processing surface itself is time dependent since the beam moves. To illustrate the importance of this, consider an example of a beam processing with a speed, V, and beam width (in the direction of beam movement), w. For a given time step, Δt, the distance the beam translates in the interval from t to $t+\Delta t$ is $V*\Delta t$. For values of Δt larger than w/V (beam width divided by translation speed), the beam translation distance exceeds the beam width and hence there are regions of the processing track that never "see" the beam. The only mechanism for changing the temperature at these locations would be thermal conduction from within the material.

In addition, even when Δt is smaller than w/V, there still exists the possibility of uneven heating. For example, regions where the beam in one timestep overlaps the beam in its new position in the next timestep receive more energy than non-overlapping regions.

For these reasons, it is necessary to determine how different time steps influence the calculations. To do this, another series of model calculations, similar to those done

to determine grid influence, were performed. In these, the grid spacing was held constant (0.100 mm in the processing direction) while the time step was varied. The beam power was again 800 W and the beam had a 750 mm x 4.50 mm rectangular tophat profile. The time step size is varied from as large as 10 ms (non-overlapping beam) to as small as 0.25 ms (beam translation distance per time step is less than grid cell spacing).

Figures 4.7 to 4.15 depict the results of these models by showing the peak temperature at the beam centerline on the surface of the sample. Rather than showing the profile at a particular instant in time, the figures show the peak temperature at each position along the line throughout the processing.

As the figures indicate, the peak temperatures exhibit an oscillatory nature that decreases with smaller time steps. The average temperature, shown in Figure 4.16 and calculated using the nearest number of complete cycles in the last 5 mm of the processed region, indicates an increase in temperature with smaller time steps. Figure 4.17 shows the amplitude of the thermal oscillation (one half the difference between average high and average low temperatures) at different time step sizes. Interestingly, the points, plotted on a log-log plot, form a line suggesting a power law relationship between the oscillation amplitude and the inverse of the time step size.

Figure 4.18 depicts the relationship between the wavelength ratio, defined to be the oscillation peak to peak distance divided by the beam translation distance, and time step size. For large Δt, the wavelength ratio is unitary, indicating a strong, and undesirable, influence of the beam's translation distance, itself determined by speed and time step size, on the thermal history of the model. Even for time steps small enough to insure the beam overlaps from one time step to the next, the influence exists. Only when

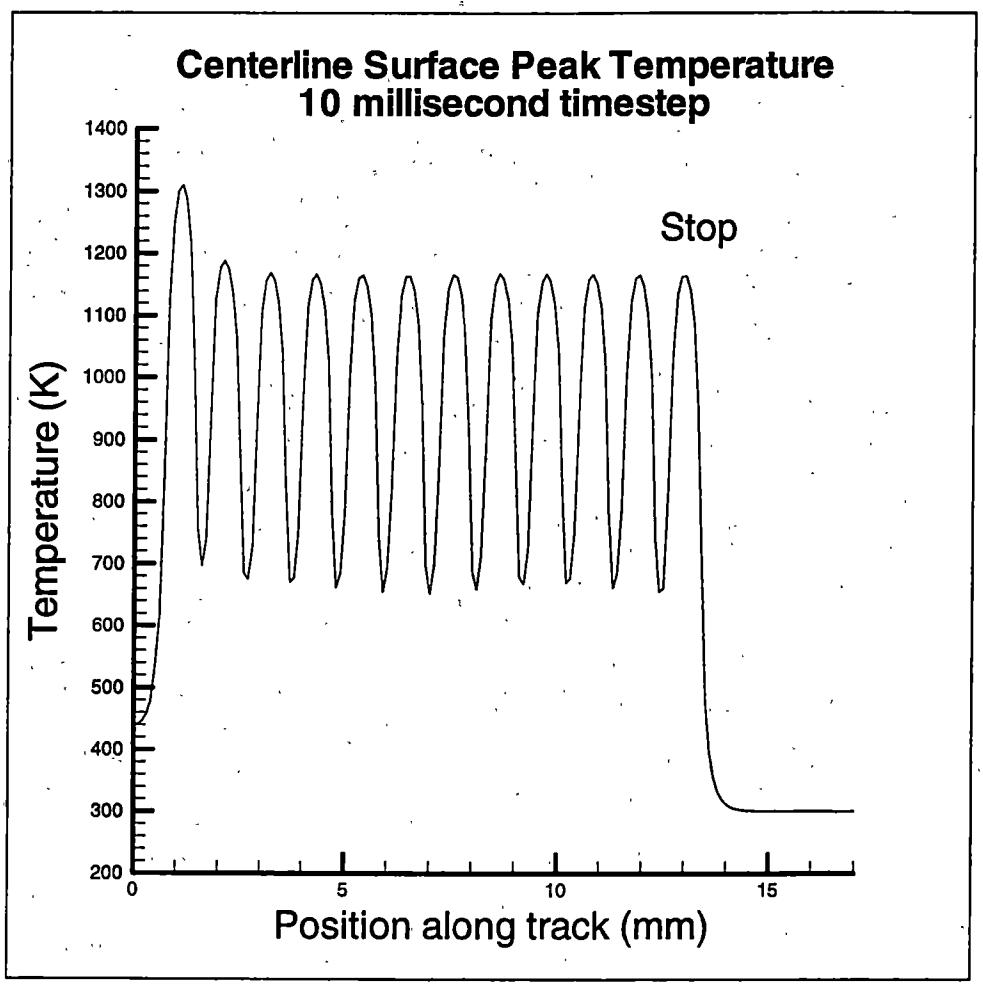


Figure 4.7: Peak surface temperatures for 10 millisecond timestep. Processing conditions were 800 W beam power, 6500 mm/min beam speed, and 4.5 mm x 0.75 mm rectangular tophat beam profile. This figure indicates the highest temperature reached at any location on the surface. With the beam starting at x = 0 mm, the model was halted when the beam reached x = 13 mm.

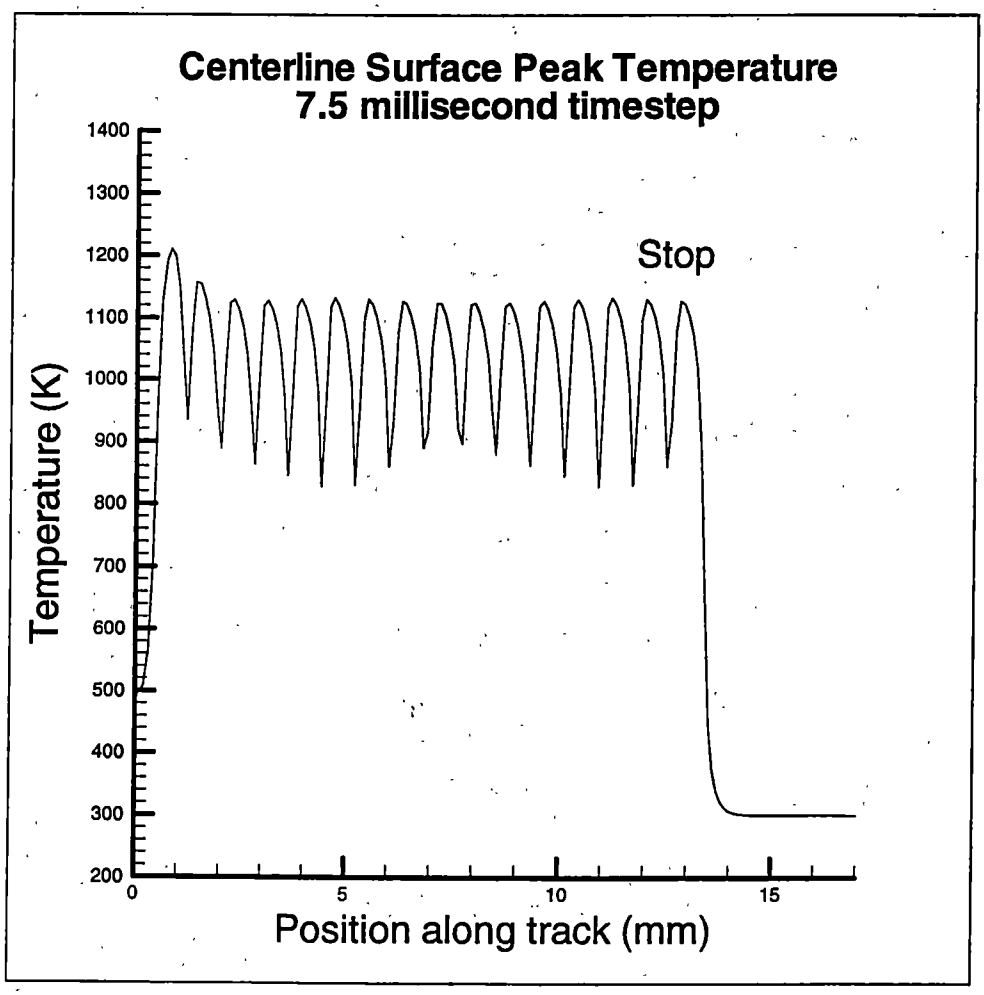


Figure 4.8: Peak surface temperatures for 7.5 millisecond timestep. Processing conditions were 800 W beam power, 6500 mm/min beam speed, and 4.5 mm x 0.75 mm rectangular tophat beam profile. This figure indicates the highest temperature reached at any location on the surface. With the beam starting at x = 0 mm, the model was halted when the beam reached x = 13 mm.

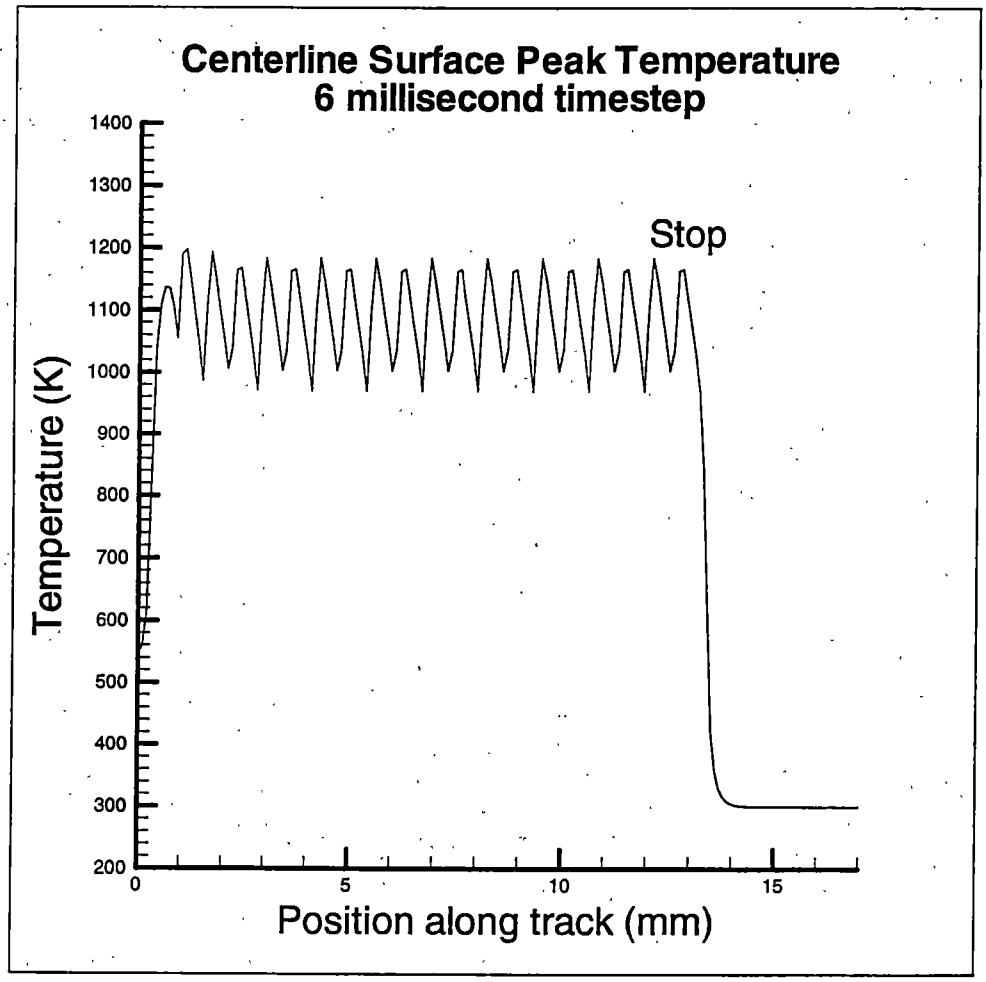


Figure 4.9: Peak surface temperatures for 6 millisecond timestep. Processing conditions were 800 W beam power, 6500 mm/min beam speed, and 4.5 mm x 0.75 mm rectangular tophat beam profile. This figure indicates the highest temperature reached at any location on the surface. With the beam starting at x = 0 mm, the model was halted when the beam reached x = 13 mm.

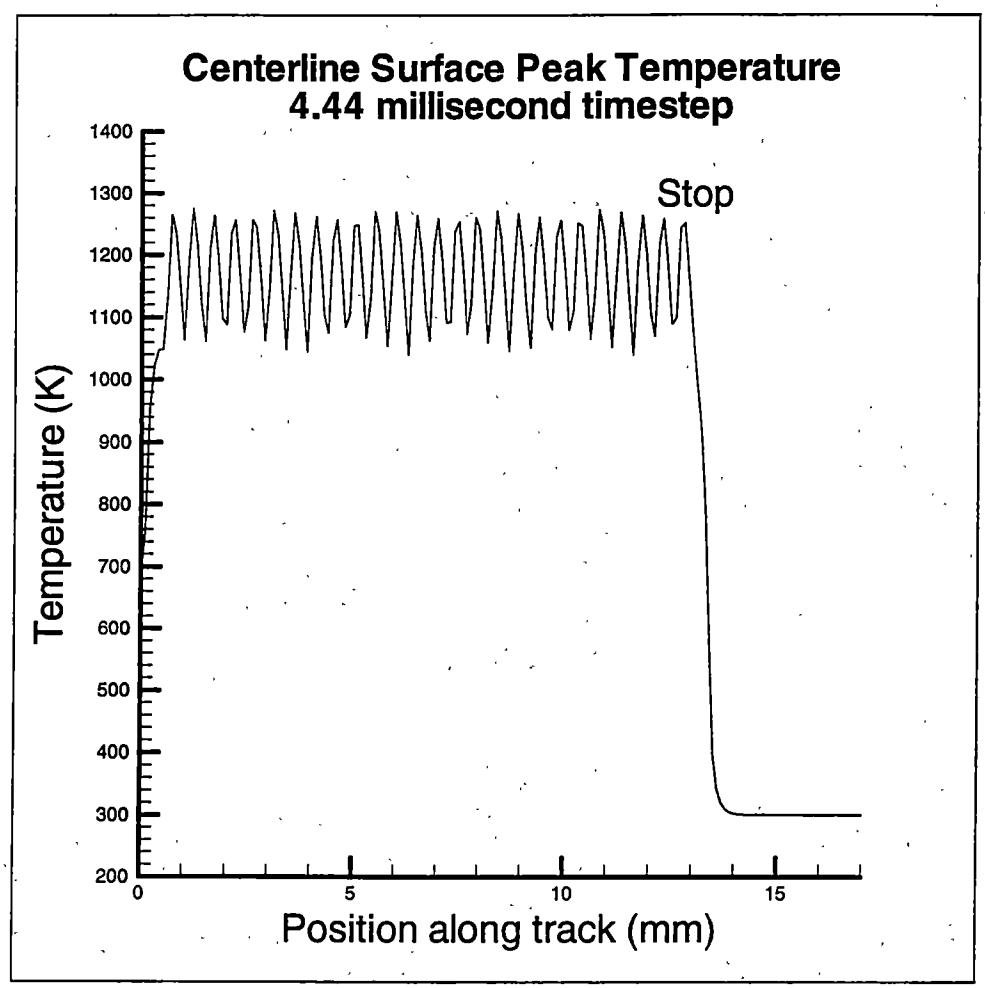


Figure 4.10: Peak surface temperatures for 4.44 millisecond timestep. Processing conditions were 800 W beam power, 6500 mm/min beam speed, and 4.5 mm x 0.75 mm rectangular tophat beam profile. This figure indicates the highest temperature reached at any location on the surface. With the beam starting at x = 0 mm, the model was halted when the beam reached x = 13 mm.

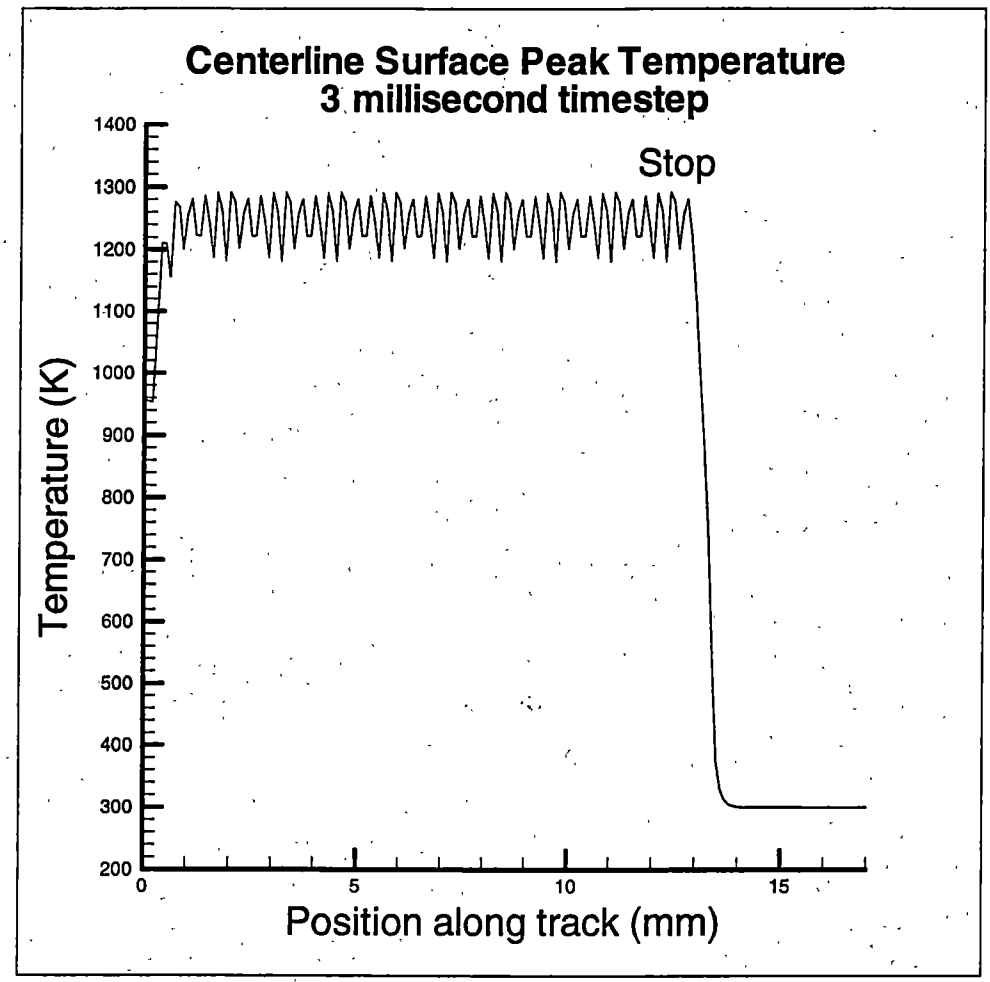


Figure 4.11: Peak surface temperatures for 3 millisecond timestep. Processing conditions were 800 W beam power, 6500 mm/min beam speed, and 4.5 mm x 0.75 mm rectangular tophat beam profile. This figure indicates the highest temperature reached at any location on the surface. With the beam starting at x = 0 mm, the model was halted when the beam reached x = 13 mm.

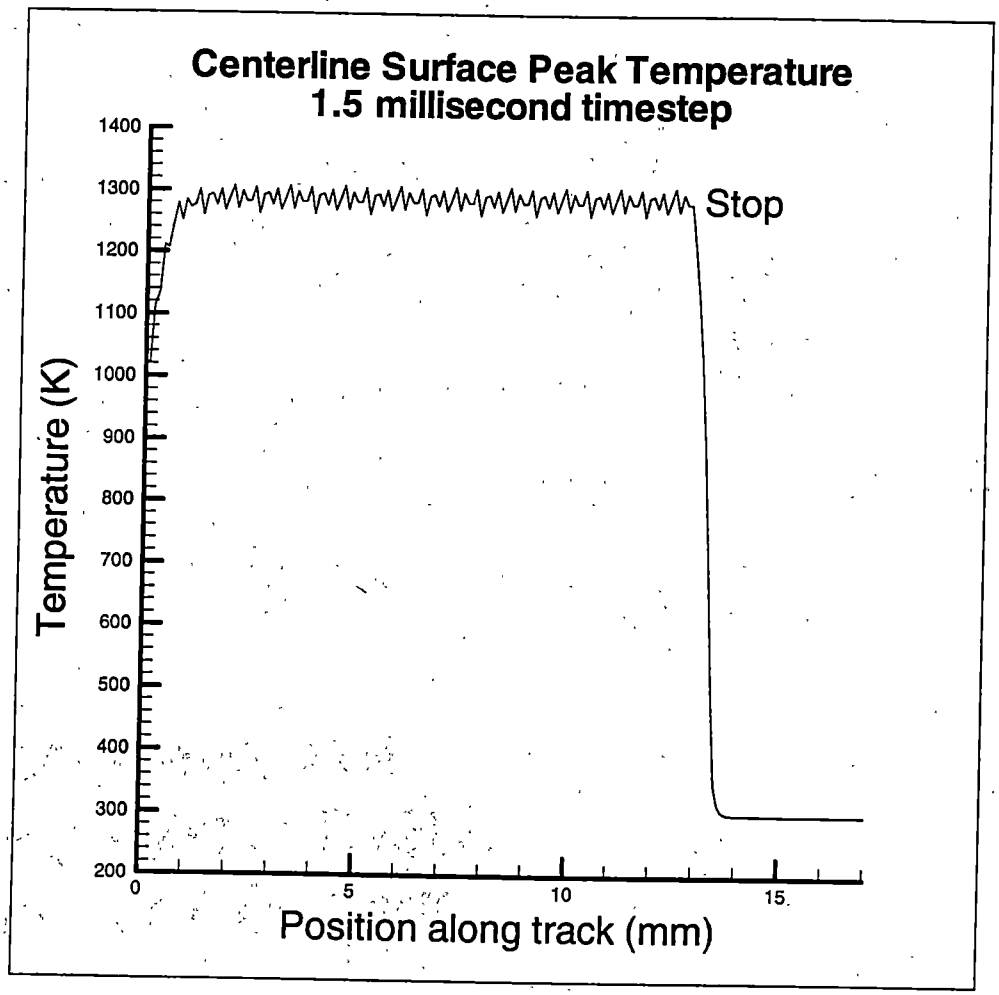


Figure 4.12: Peak surface temperatures for 1.5 millisecond timestep. Processing conditions were 800 W beam power, 6500 mm/min beam speed, and 4.5 mm x 0.75 mm rectangular tophat beam profile. This figure indicates the highest temperature reached at any location on the surface. With the beam starting at x = 0 mm, the model was halted when the beam reached x = 13 mm.

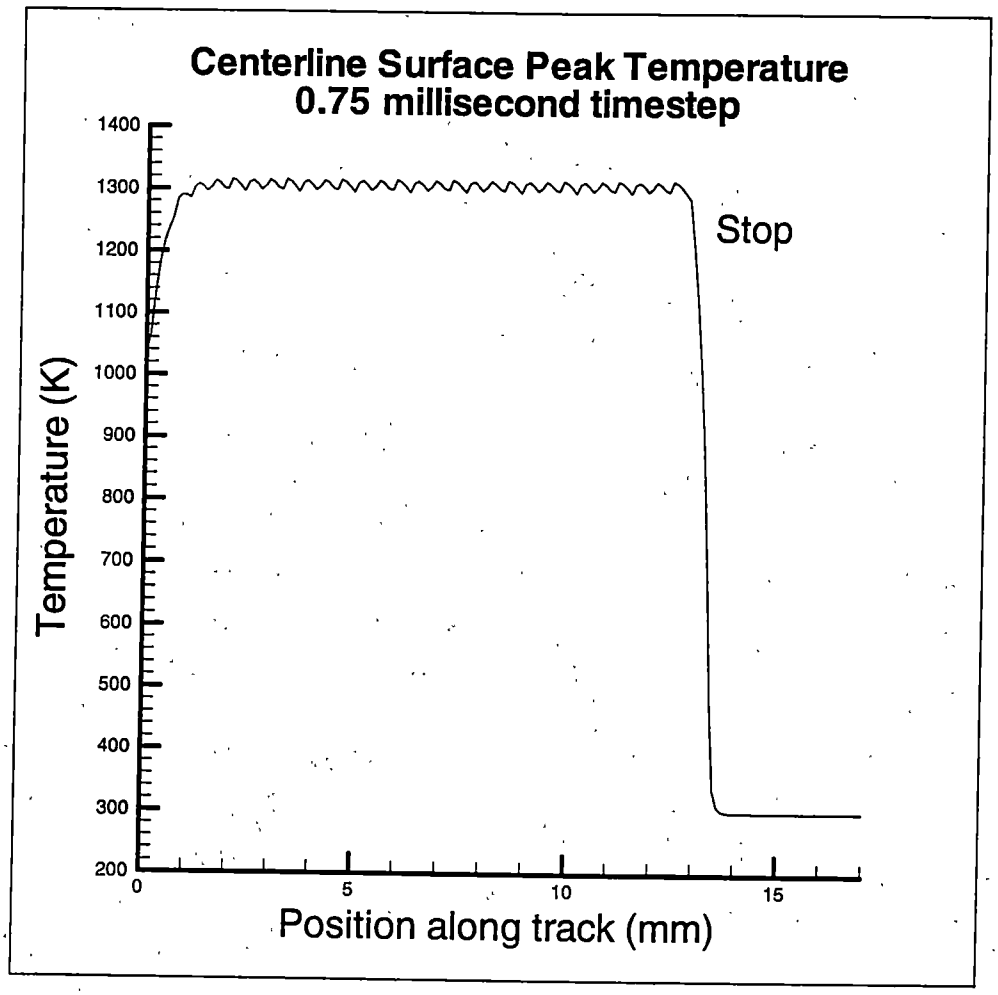


Figure 4.13: Peak surface temperatures for 0.75 millisecond timestep. Processing conditions were 800 W beam power, 6500 mm/min beam speed, and 4.5 mm x 0.75 mm rectangular tophat beam profile. This figure indicates the highest temperature reached at any location on the surface. With the beam starting at x = 0 mm, the model was halted when the beam reached x = 13 mm.

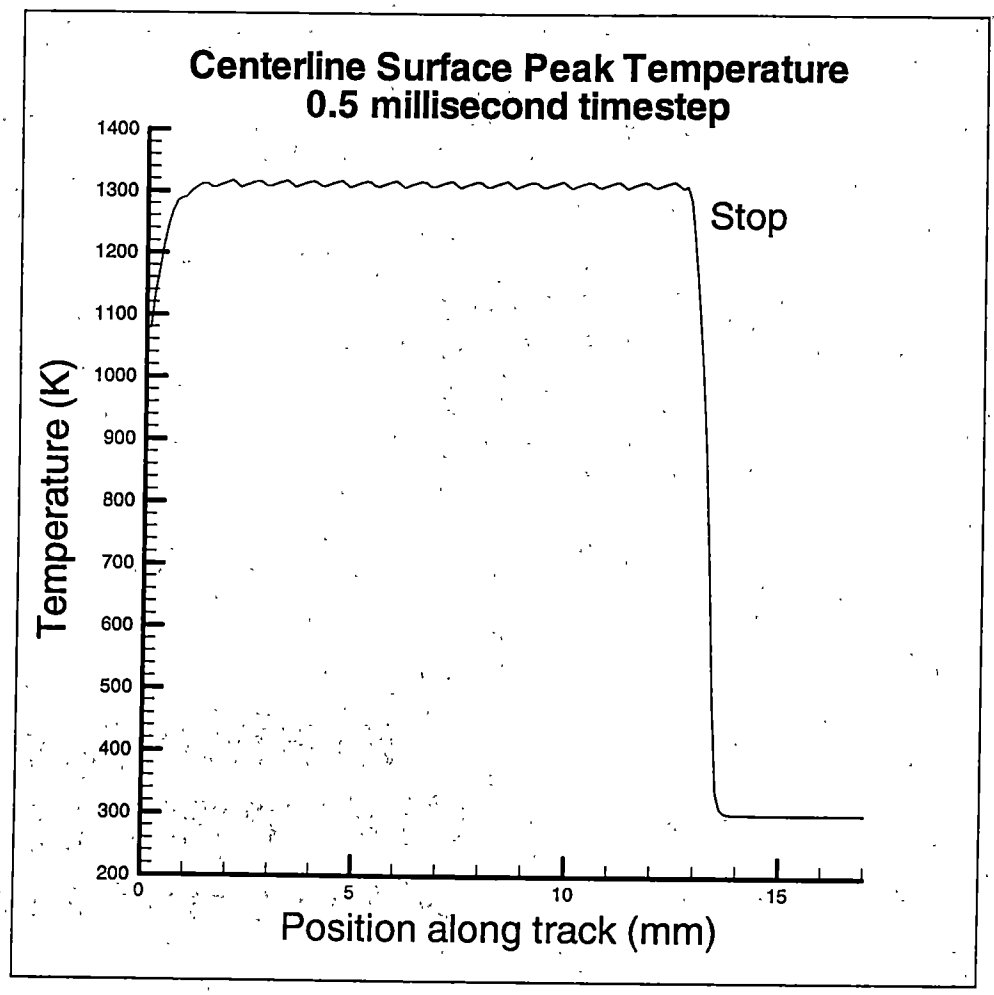


Figure 4.14: Peak surface temperatures for 0.5 millisecond timestep. Processing conditions were 800 W beam power, 6500 mm/min beam speed, and 4.5 mm x 0.75 mm rectangular tophat beam profile. This figure indicates the highest temperature reached at any location on the surface. With the beam starting at x = 0 mm, the model was halted when the beam reached x = 13 mm.

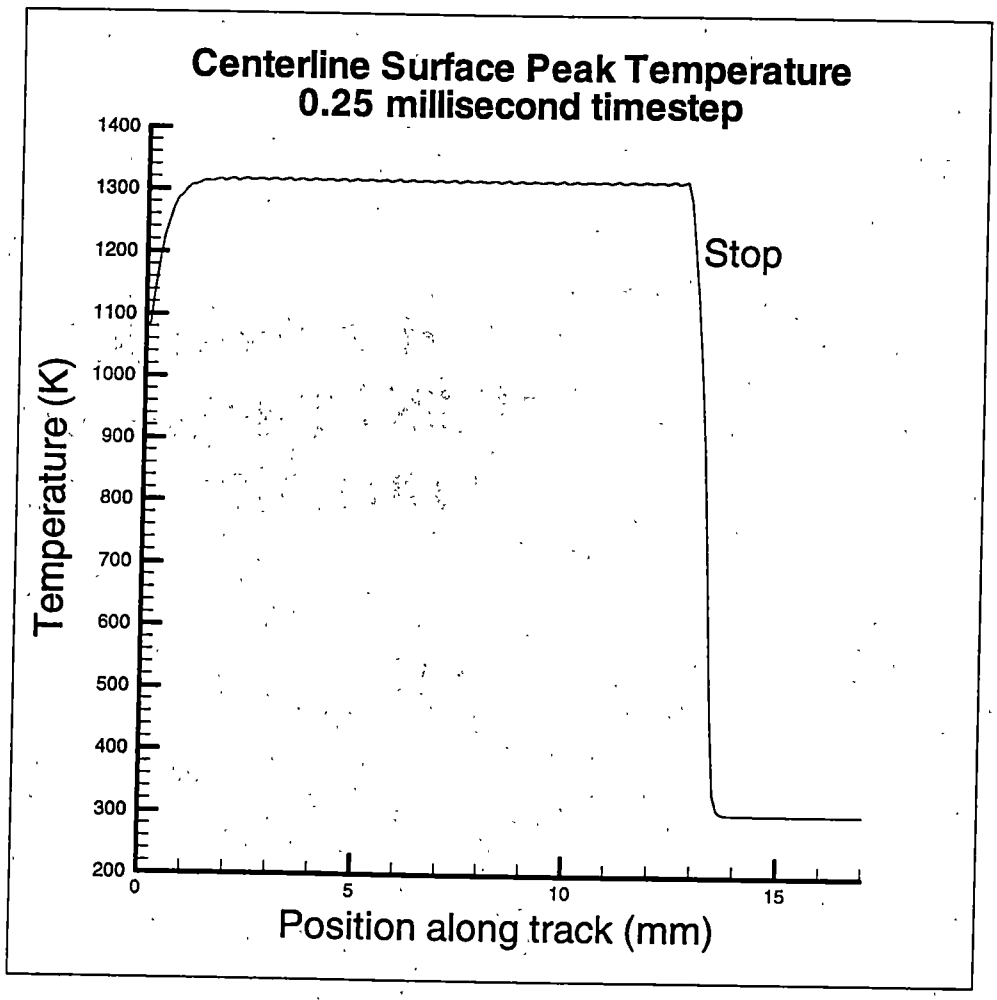


Figure 4.15: Peak surface temperatures for 0.25 millisecond timestep. Processing conditions were 800 W beam power, 6500 mm/min beam speed, and 4.5 mm x 0.75 mm rectangular tophat beam profile. This figure indicates the highest temperature reached at any location on the surface. With the beam starting at x = 0 mm, the model was halted when the beam reached x = 13 mm.

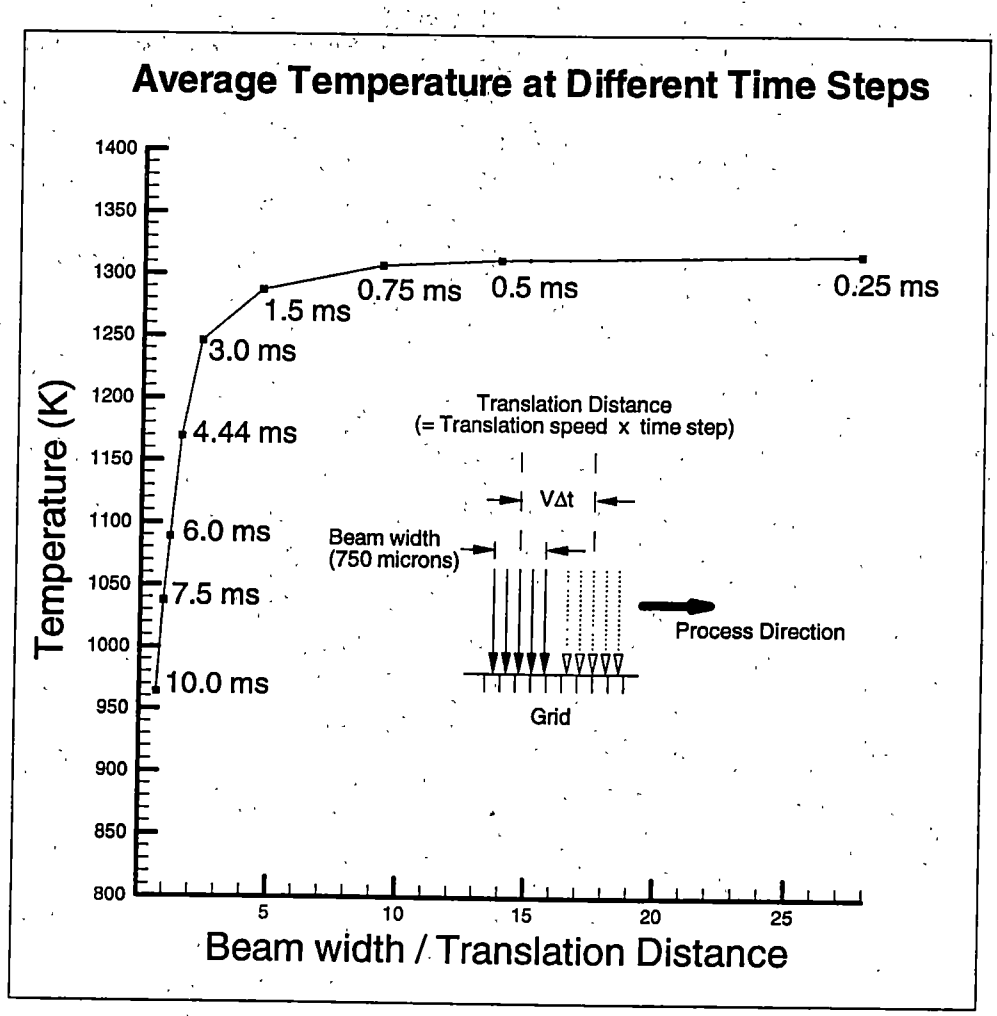


Figure 4.16: The influence of the discrete timestep on peak temperatures. Values are obtained by averaging the peak temperature of the track center grid points on the surface.

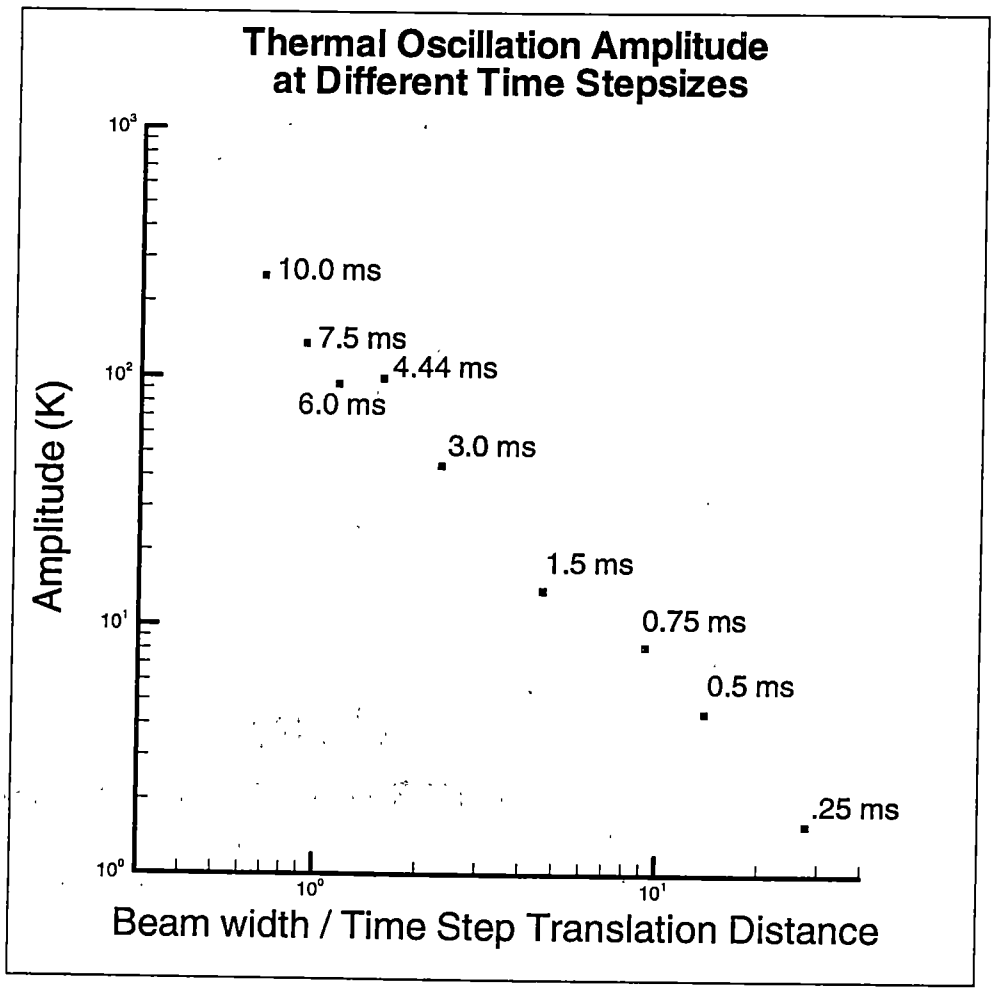


Figure 4.17: The magnitude of the thermal oscillation at different timestep sizes.

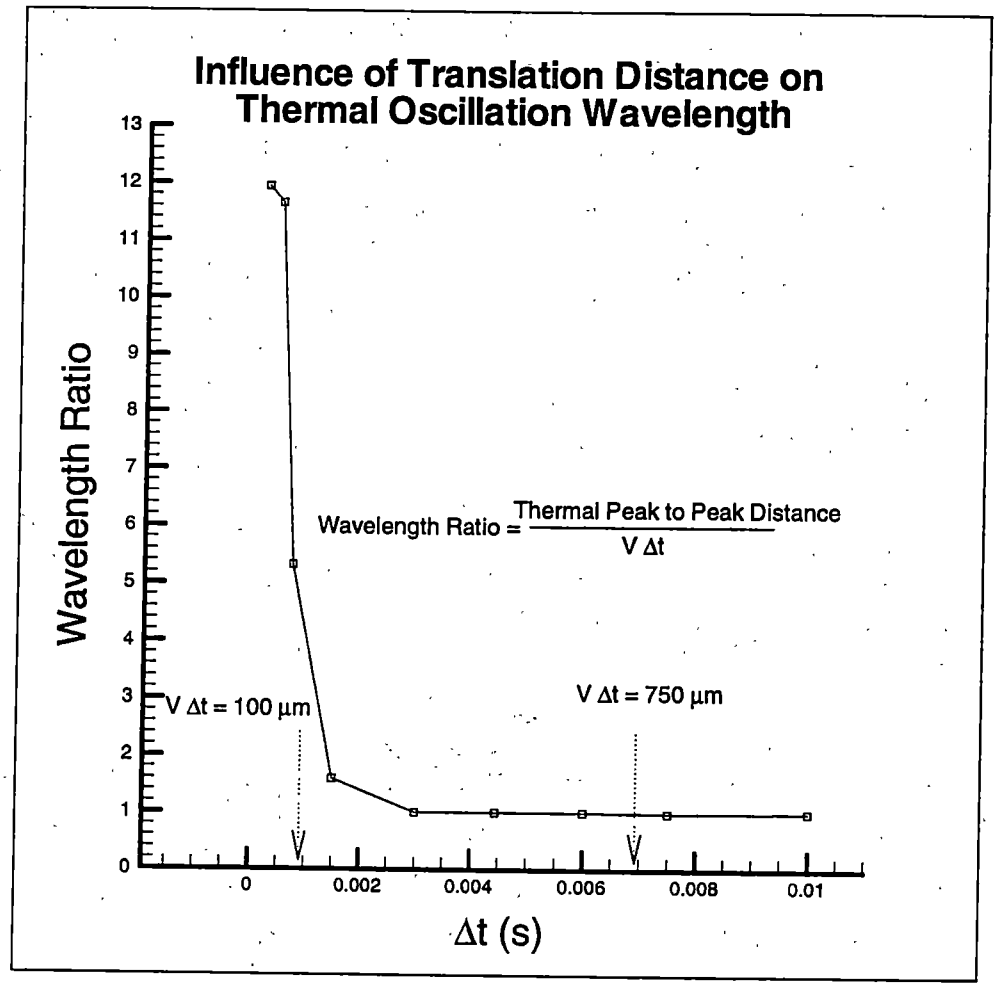


Figure 4.18: The wavelength of the thermal oscillation at different time steps. Arrows indicate the times at which the translation distance is equal to the x direction grid spacing (0.1 mm) and beam width (0.75 mm).

the step size is small enough that the translation distance is less than the grid size (marked as 100 microns on Figure 4.18), does the influence begin change. Although some oscillation still exists, the grid spacing begins to affect the periodicity of the oscillation by elongating it.

Based on results of grid cell spacing and time step size models, a grid spacing of 0.100 mm and a time step size of 0.5 ms were selected. Although these values are small and will therefore require a large number of grid cells and total time steps, they are necessary in order to calculate an accurate thermal history for purposes of determining rates of thermal change.

4.9 Comparison with Temperature Measurements

To verify that the numerical calculations are consistent with actual processing results, a series of thermocouple instrumented coupons were processed at 2 different beam powers and three different speeds, as listed in Table 4.1.

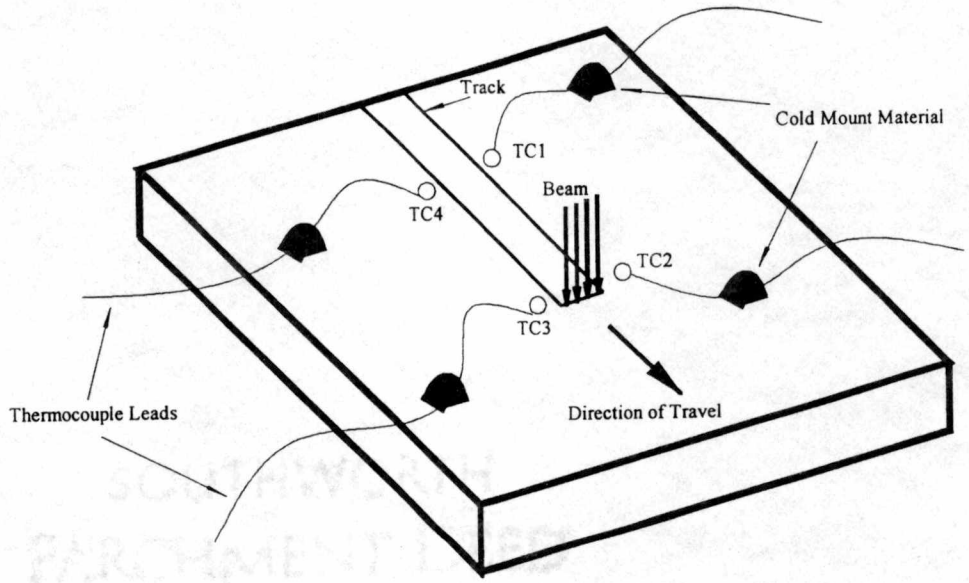
The coupons were 1" x 1" x ¼" size AISI 1050 steel. The coupons were sandblasted to provide a clean surface. Four type K thermocouples were then attached, held in place using a small bead of silver paint. The thermocouples were positioned in

Table 4.1 Processing Conditions for Temperature Comparisons

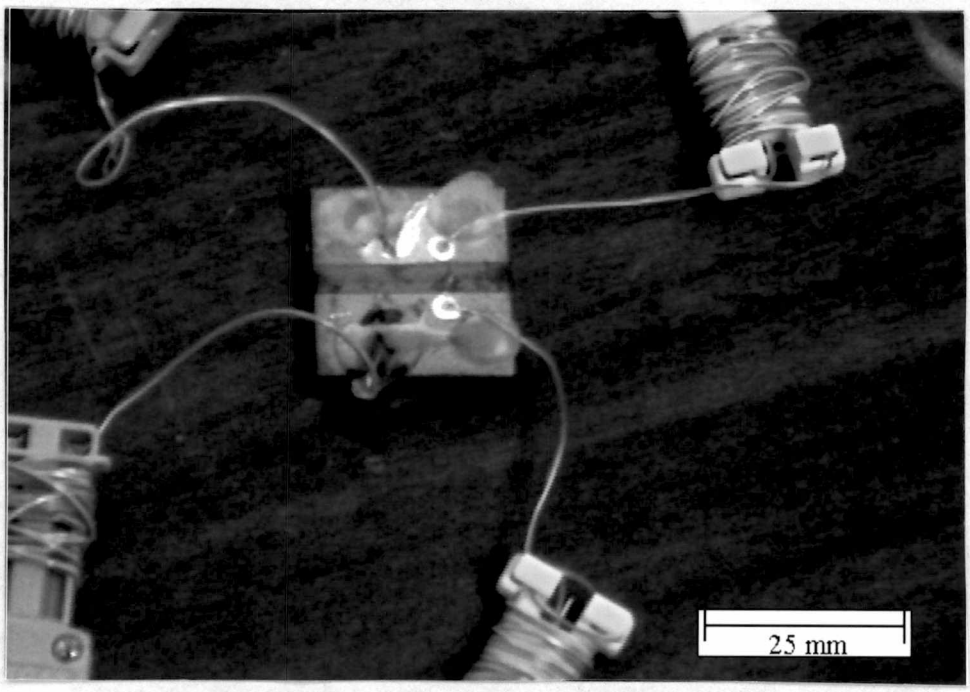
RDY	Beam Power (W)	Beam Speed (mm/min)
1002-1	500	5000
1002-2	500	6500
1002-3	650	6500
1002-4	650	6500
1002-5	650	8450
1002-6	650	8450

pairs just outside and on either side of the edge of the intended track (see Figure 4.19). The first pair was positioned towards the leading edge of the coupon and the second pair was positioned toward the trailing edge. Measurements were made using an ADAC data acquisition board with Testpoint software.

The thermocouples have a spherical bead approximately 300 microns in diameter. Figures 4.20 to 4.25 compare the results of measurements with model values for the six different samples. Using the thermocouple bead diameter as a measure of the thermocouples' uncertainty in position, the figures show calculated thermal profiles 300 microns closer to and further from the estimated position. The temperature profiles from one sample to another are different because the positions of the thermocouples, determined by microscopically inspecting for the bead impression left in the silver paint used to hold them in place, changes from one sample to another.



a) Schematic



b) Photo

Figure 4.19: Instrumented steel coupon showing the typical location of the thermocouples. Silver paint is used to hold the thermocouples (indicated by "TC" and numbered clockwise in the schematic) in place. A cold mount curing resin holds the thermocouple leads in place.

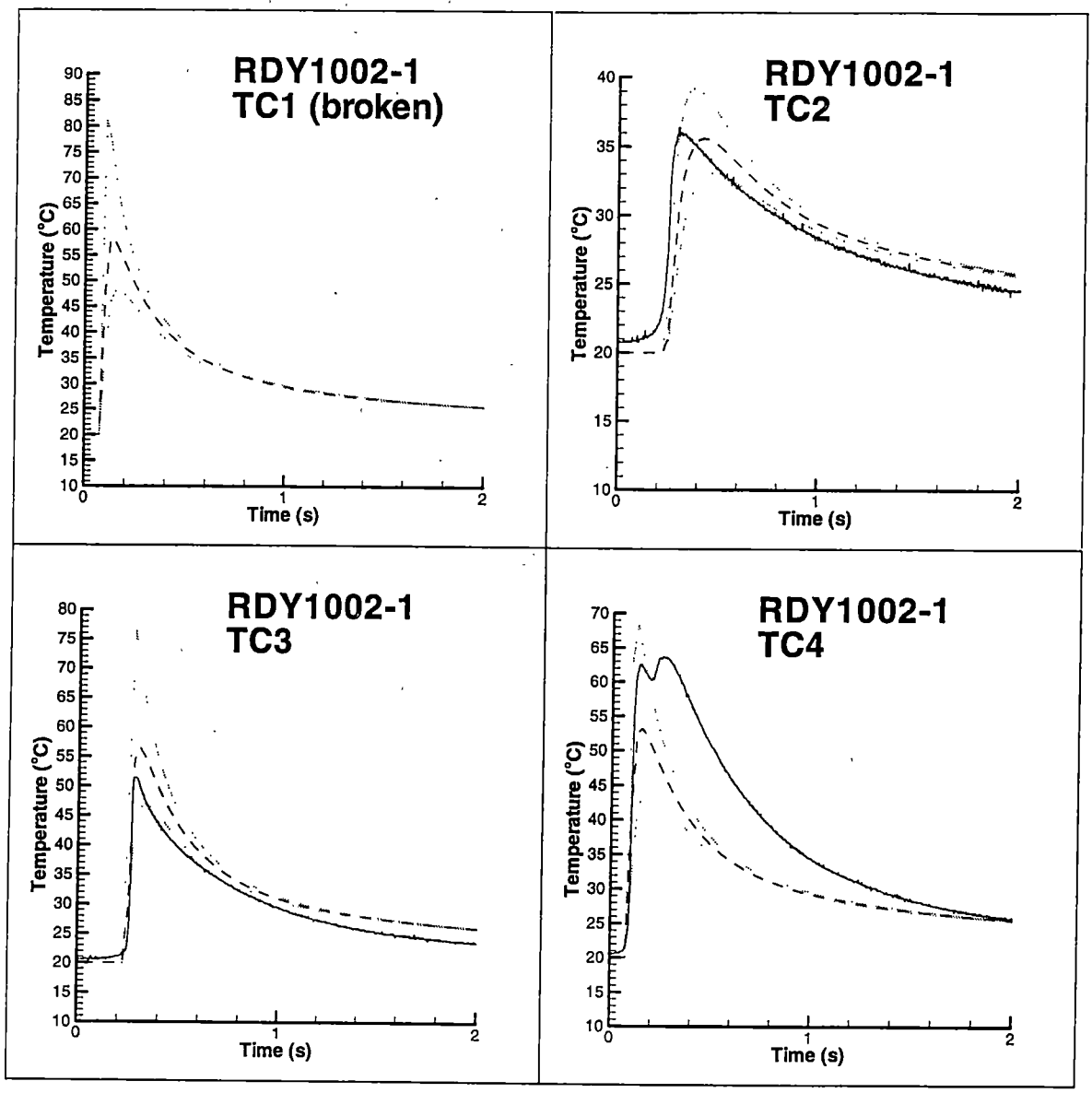


Figure 4.20: Comparing measured and modeled temperature profiles for run 1. The solid line indicates the measured temperature. The dashed line represents the modeled profile at the estimated location of the center of the thermocouple bead. The dotted lines indicate modeled profiles one bead diameter closer to and further from the beam. (thermocouple #1 was broken and failed to give any data). The processing conditions were 500 W beam power and 5000 mm/min beam speed.

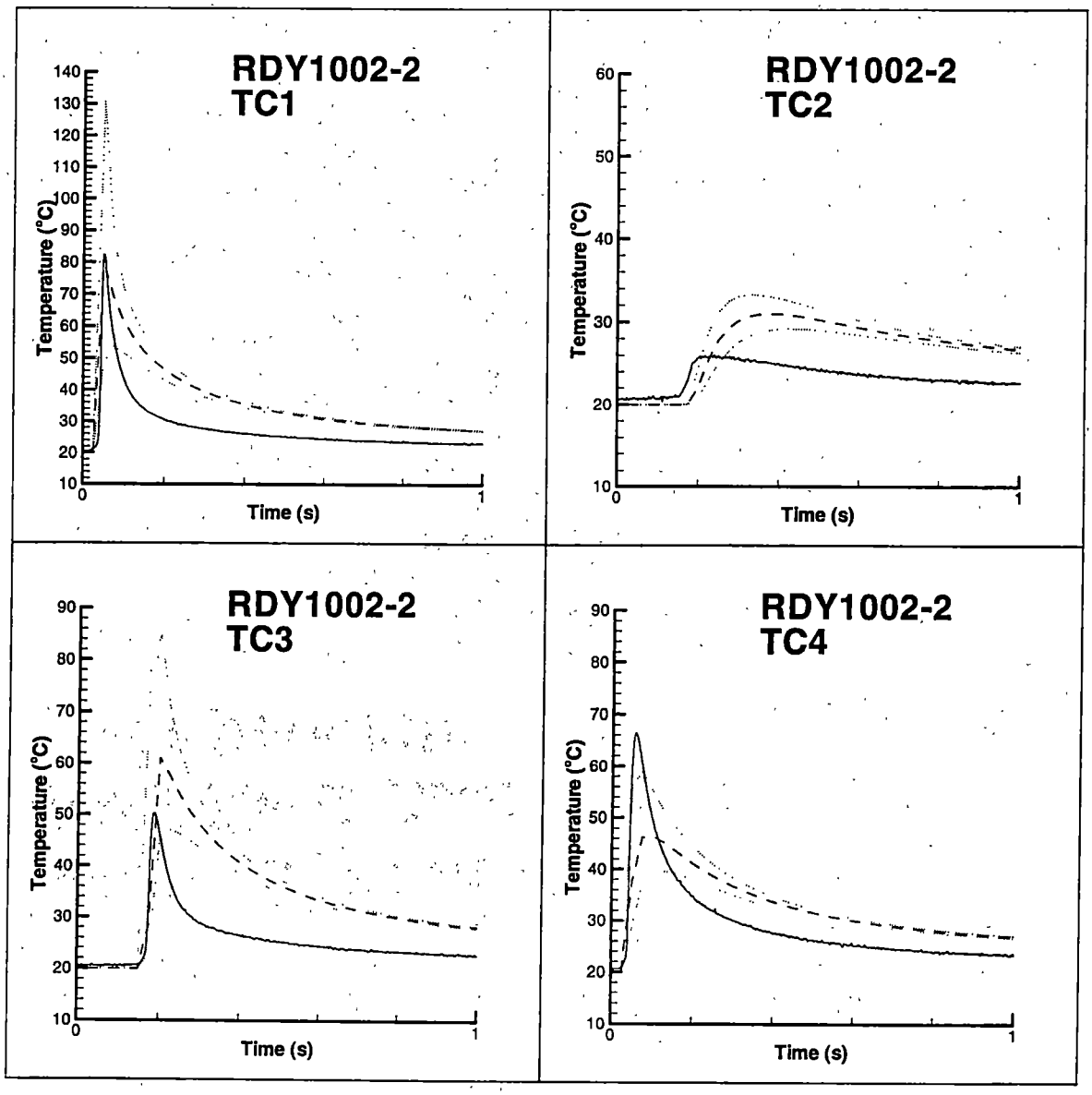


Figure 4.21: Comparing measured and modeled temperature profiles for run 2. The solid line indicates the measured temperature. The dashed line represents the modeled profile at the etimated location of the center of the thermocouple bead. The dotted lines indicate modeled profiles one bead diameter closer to and further from the beam. The processing conditions were 500 W beam power and 6500 mm/min beam speed.

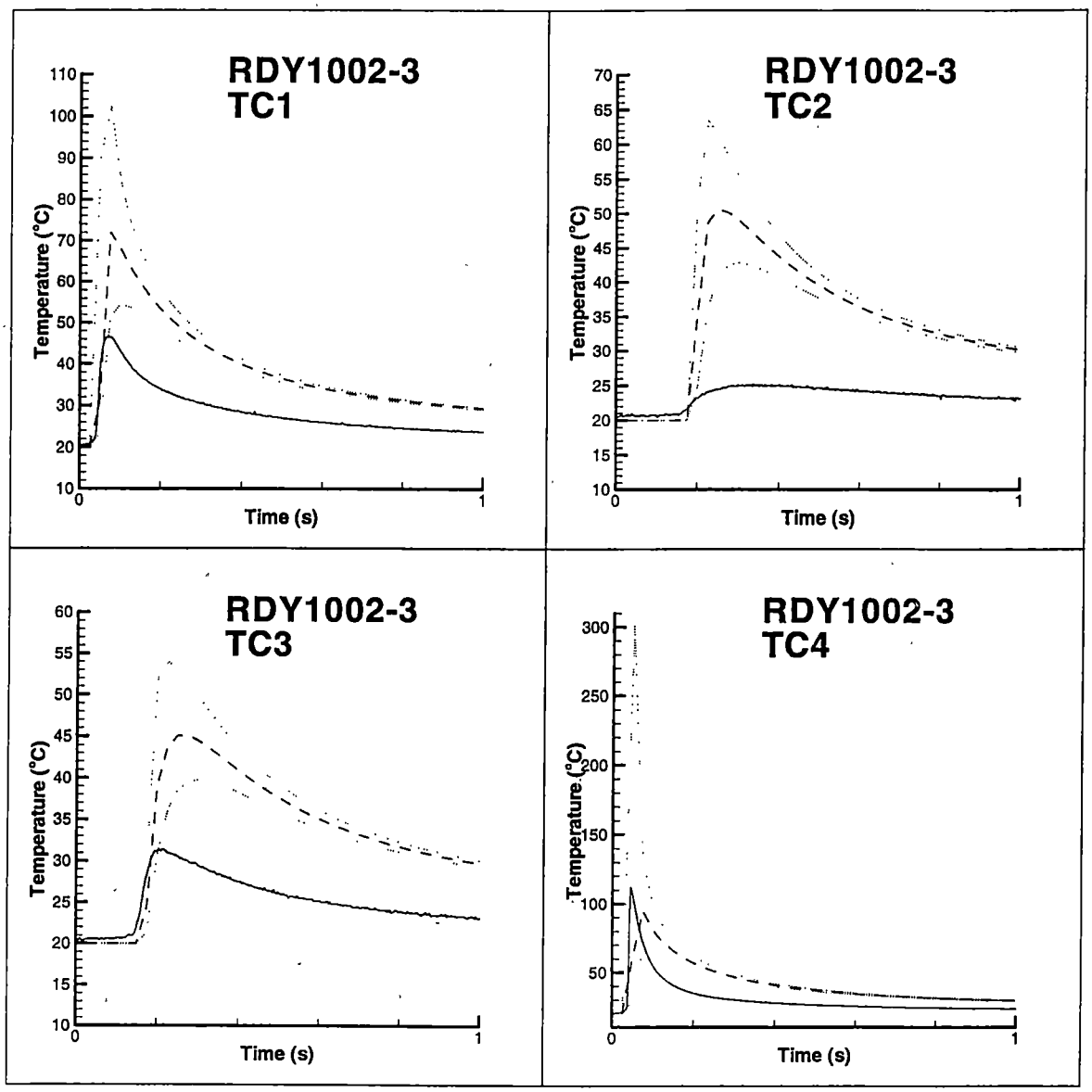


Figure 4.22: Comparing measured and modeled temperature profiles for run 3. The solid line indicates the measured temperature. The dashed line represents the modeled profile at the estimated location of the center of the thermocouple bead. The dotted lines indicate modeled profiles one bead diameter closer to and further from the beam. The processing conditions were 650 W beam power and 6500 mm/min beam speed.

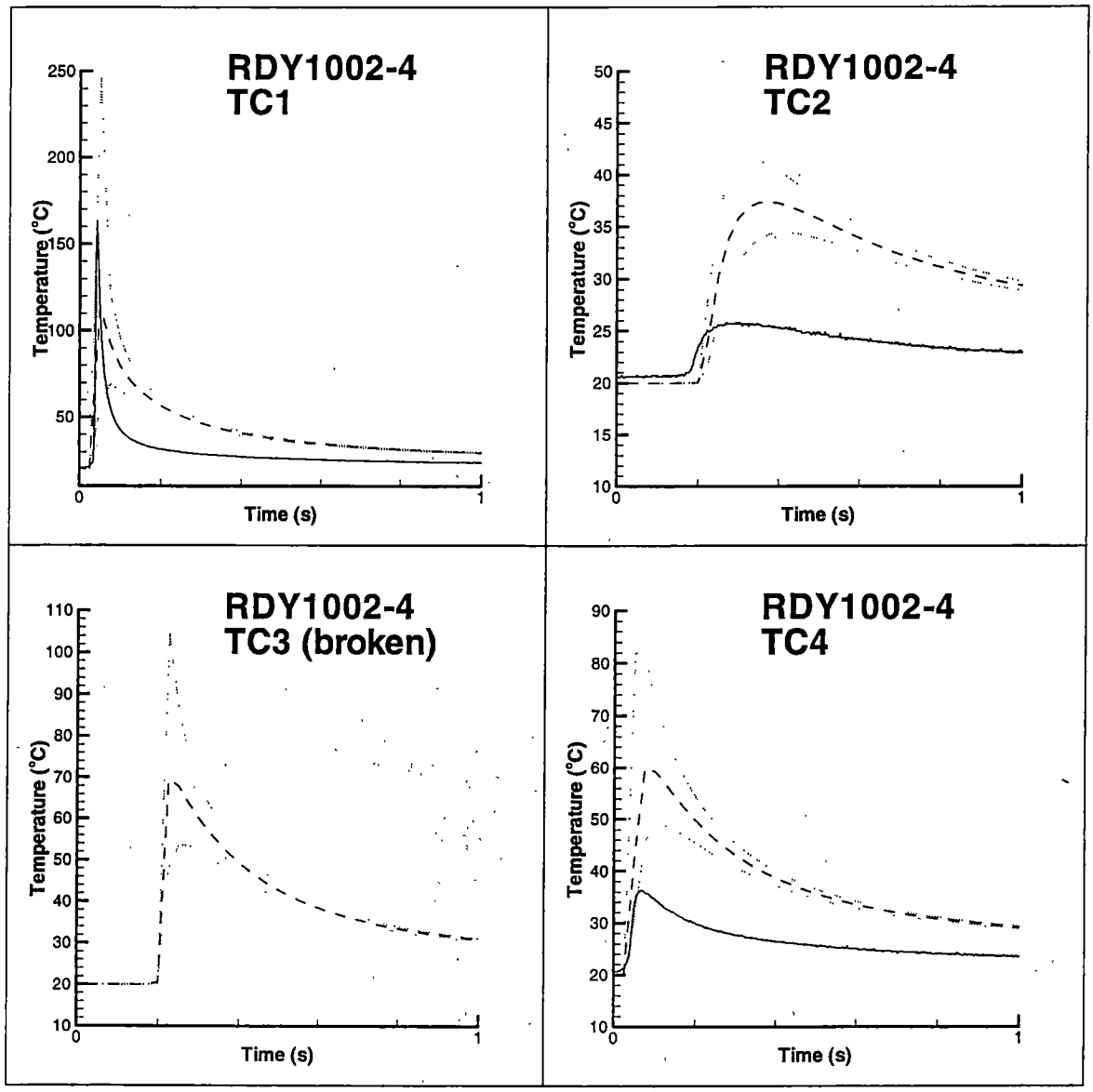


Figure 4.23: Comparing measured and modeled temperature profiles for run 4. The solid line indicates the measured temperature. The dashed line represents the modeled profile at the estimated location of the center of the thermocouple bead. The dotted lines indicate modeled profiles one bead diameter closer to and further from the beam (thermocouple #3 broke and gave no data). The processing conditions were 650 W beam power and 6500 mm/min beam speed.

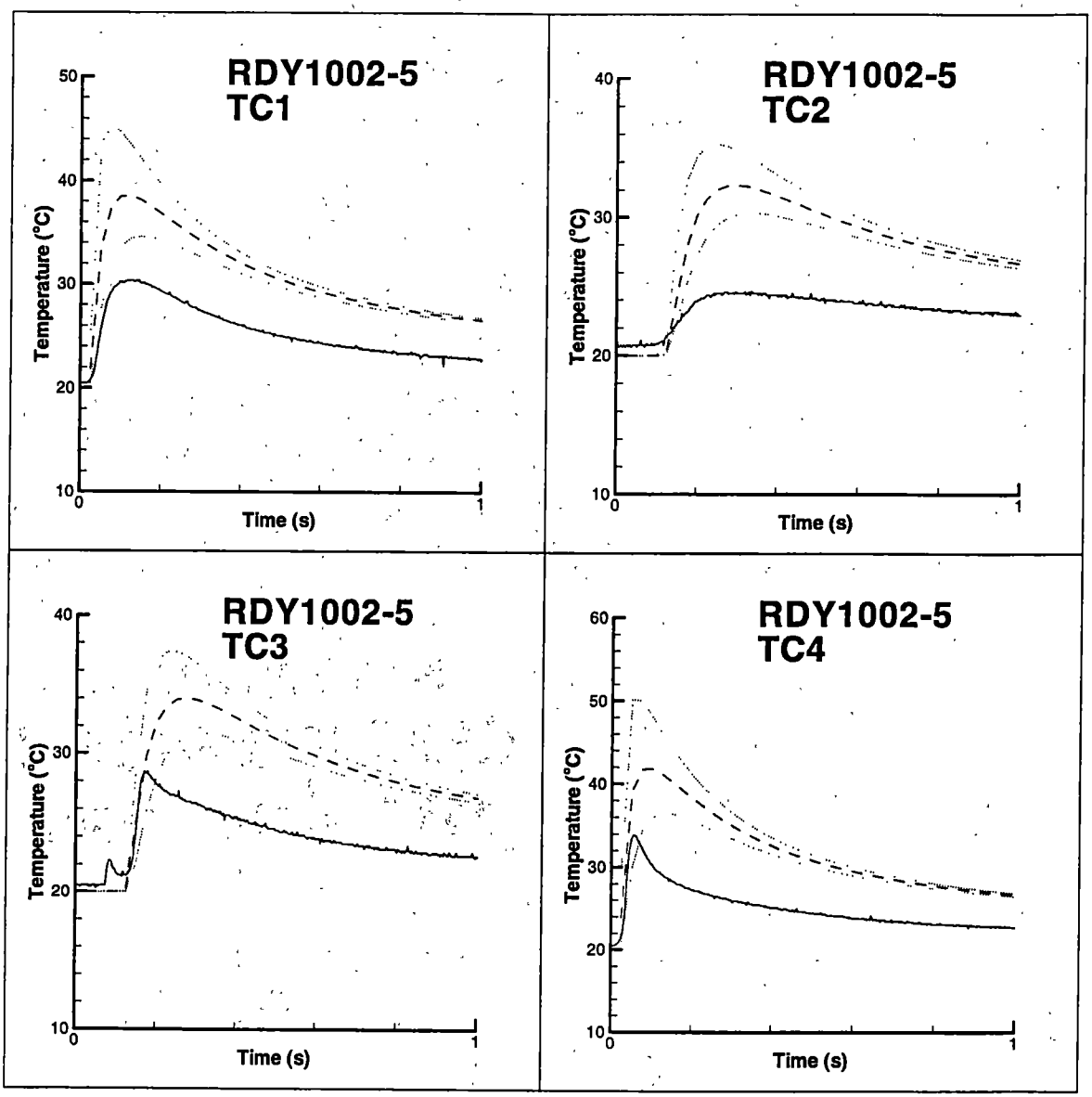


Figure 4.24: Comparing measured and modeled temperature profiles for run 5. The solid line indicates the measured temperature. The dashed line represents the modeled profile at the estimated location of the center of the thermocouple bead. The dotted lines indicate modeled profiles one bead diameter closer to and further from the beam. The processing conditions were 650 W beam power and 8450 beam speed.

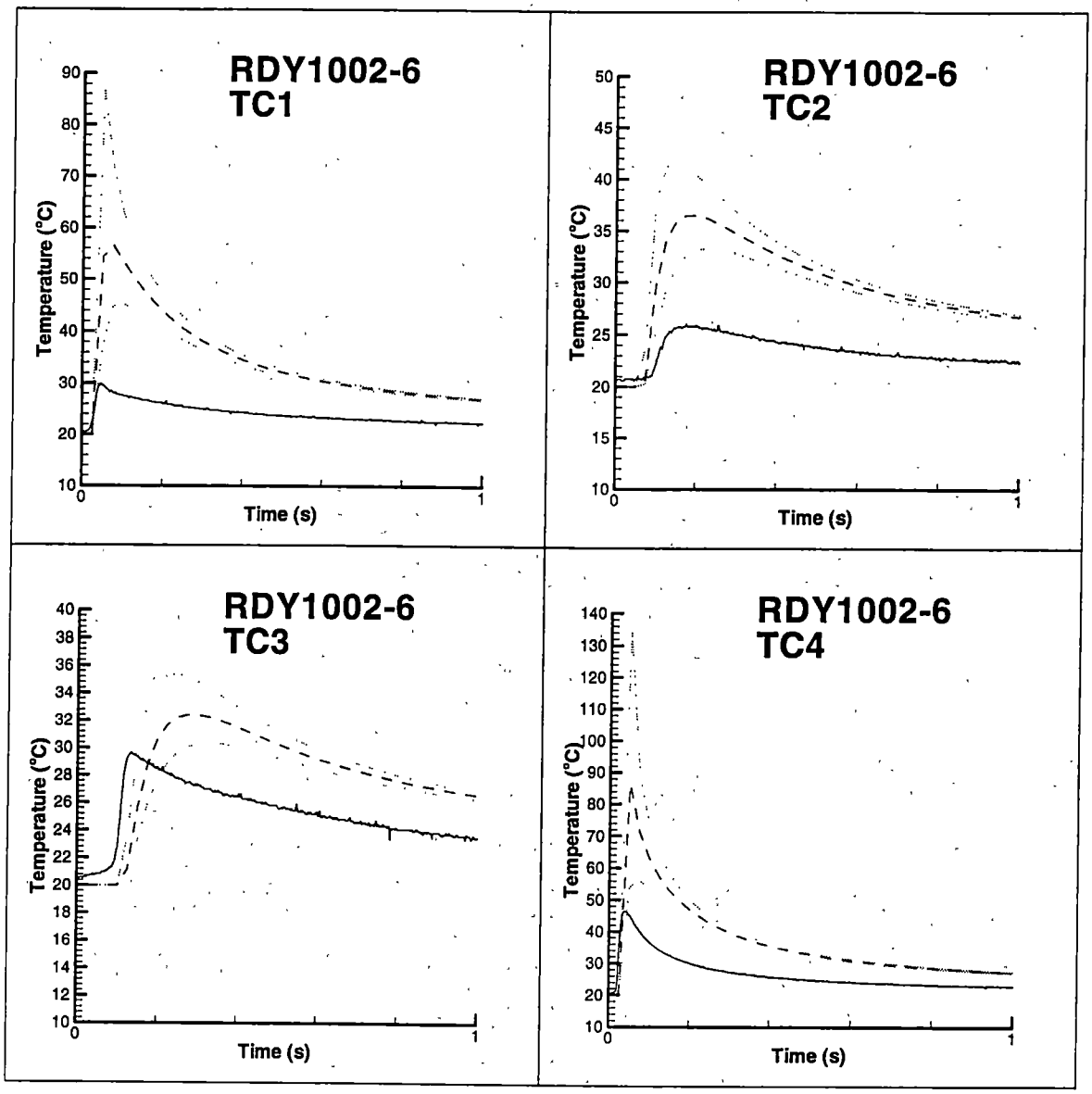


Figure 4.25: Comparing measured and modeled temperature profiles for run 6. The solid line indicates the measured temperature. The dashed line represents the modeled profile at the estimated location of the center of the thermocouple bead. The dotted lines indicate modeled profiles bead diameter closer to and further from the beam. The processing conditions were 650 W beam power and 8450 mm/min beam speed.

CHAPTER V

EXPERIMENTAL AND NUMERICAL

This chapter describes the actual processing conditions used in both the numerical and experimental portions of this research. Chapter IV described the model properties, and included comparisons with experiments performed for the sole purpose of validating the model. This chapter focuses on the processing parameters designed to produce a temporal thermal field numerically that replicates the thermal field that exists when heat treating steel with a laser. The next chapter will compare the results to determine how well the model could be used to predict resulting properties when actual laser heat treating is performed and determine the influence of the overlap on the resulting thermal field

5.1 Numerical Processing Parameters

Initially, the experimental beam shape's geometry wasn't known and could only be inferred based on an examination of the processed material's heat affected zone (beam width approximately equal to a single track width for example). As was described in Section 4.3, by iterating on the modeled beam's geometry (width and length) and absorption coefficient, reasonable agreement was obtained between experimental and numerical heat affected zones (where the transition temperature isotherm was used to define the numerical HAZ boundary).

The resulting beam geometry, 3.4 mm long by 0.3 mm wide rectangular tophat, was assumed to be reasonably close to the actual beam since the thermal measurements agreed well with predicted ones.

Owing to the exceptional amount of real time this model takes to solve, only one different overlap case was studied. The processing parameters (Table 5.1) were 650 W beam power, 6500 mm/min translation speed and 1.7 mm index. The beam power and speed were chosen based on results from Chapter 4 in which it was determined that 800 W and 6500 mm/min just initiates melting on the top surface; using a lower beam power insures no melting.

5.2 Experimental Processing Parameters

Initially, an estimate for the beam shape had to be used for the numerical model since an accurate measurement of the actual beam wasn't available. Later however, after the modeling runs had been completed, the University of Tennessee Space Institute obtained a profilometer (Veeko Metrology WYKO RST500) capable of determining the laser output profile. Unfortunately, upon examining the beam profile used in making the temperature measurements, it was seen that the actual processing beam was somewhat different than the modeled beam. As is seen in Figure 5.1, an equivalent rectangular tophat beam that has the same cross sectional area of the real beam would have a width of 0.45 mm, significantly more than the model incorporates.

Table 5.1 Model Processing Parameters

Parameter	**Values**
Beam Power	650 watts
Translation Speed	6500 mm/min
Index	1.7 mm

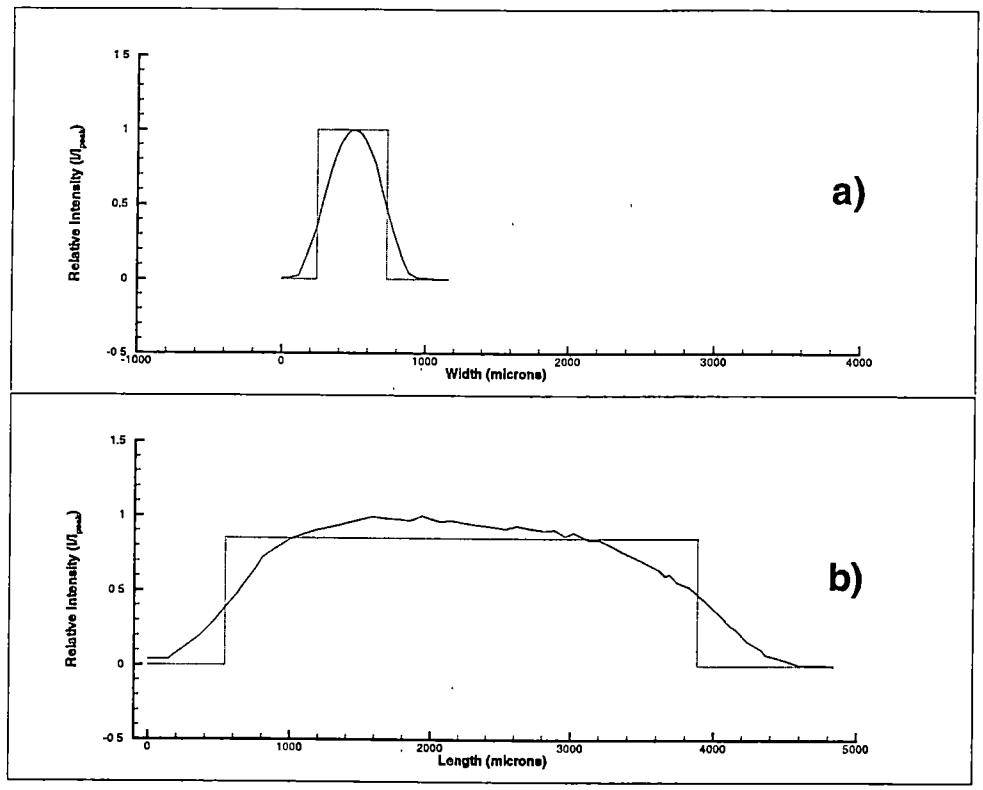


Figure 5.1: Measured beam profile for 4643 optics at focus for a) beam width (direction of beam travel) and b) beam length. The equivalent tophat with the same peak intensity and is 3.36 mm long x 0.45 mm wide (dotted line shown), wider than the 3.40 mm long x 0.30 mm wide beam used in the model.

To compensate for this change, a new optics arrangement was made so that the equivalent tophat cross sectional width could be reduced to 0.31 mm, only slightly more than the 0.30 mm used in the model (see Figure 5.2). In order to compensate for the slightly wider beam, the processing speed was increased (proportional to the width increase) to 6717 mm/min.

In addition, in order to reduce the beam width in the new optics it was necessary to increase the length of the beam to 4.5 mm. Since, for a given beam power increasing the beam width decreases the beam intensity, and the peak intensity flux is critical to the energy balance, the beam power was increased for the experiments in order to keep the peak intensities of the modeled and actual beams comparable. If the absorption coefficient were known, the increase would be proportional to the area ratio of the actual and modeled laser. However, since there is uncertainty in knowing the actual absorption coefficient for the processed material, a series of single tracks at multiple powers were done on 3" x 6" pieces of 1050 steel to determine HAZ depths for comparison to modeled predictions.

In the model, with the beam power set to 650 W and using an absorption coefficient of 0.49, the power absorbed by the modeled sample is 318.5 W. Since the actual beam is wider, to keep the absorbed intensity the same its necessary for the absorbed power to be increased to 435.6 W. Table 5.2 lists the different delivered beam powers and the absorption coefficient the sample would need to have to absorb 435.6 W. After performing the single track experiments and examining the results, three were selected for multitrack runs. Table 5.3 lists the beam power and overlap index used in those trials.

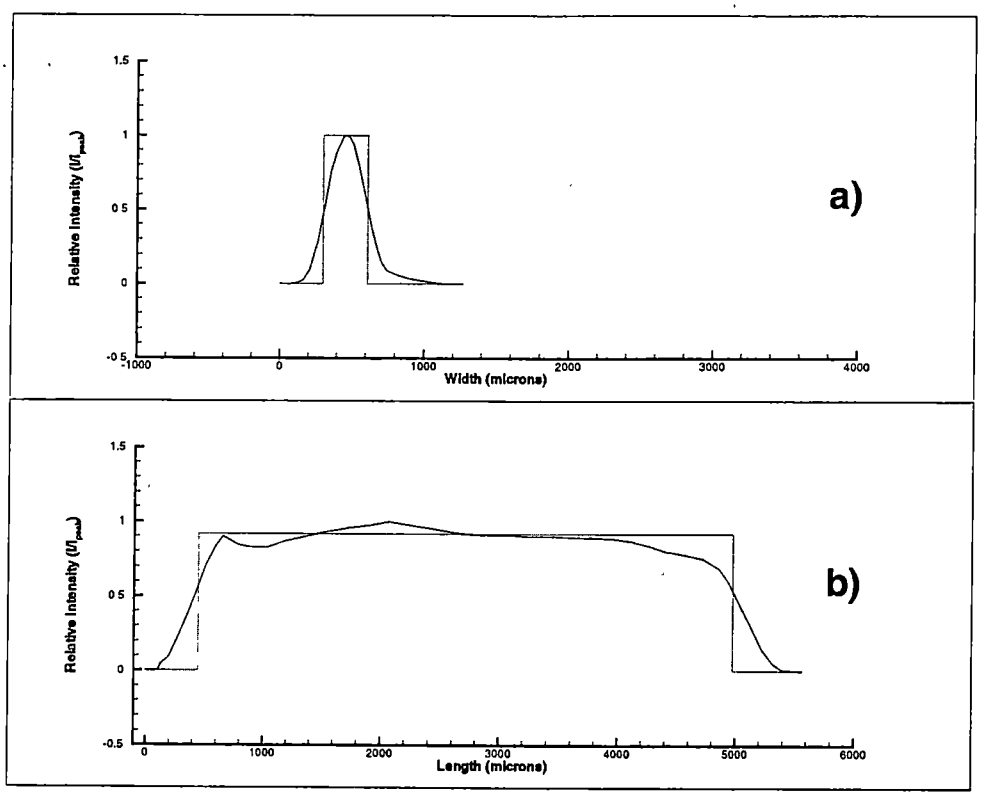


Figure 5.2: Measured beam profile for 6644 optics at focus for a) beam width (in the direction of beam travel) and b) beam length. The equivalent tophat with the same peak intensity is 4.50 mm long x 0.31 mm wide (dotted line shown), nearly identical in width to the 0.30 mm wide beam used in the model. In addition, the length profile more closely approximates that of a tophat.

Table 5.2 Processing Parameter for Single Track Experiments

RDY	# of Tracks	Delivered Power	Beam Speed	Absorptivity
1135-1	1	1452 watts	6717 mm/min	0.3
1135-2	1	1245 watts	6717 mm/min	0.35
1135-3	1	1089 watts	6717 mm/min	0.4
1135-4	1	968 watts	6717 mm/min	0.45
1135-5	1	871 watts	6717 mm/min	0.5
1135-6	1	792 watts	6717 mm/min	0.55
1135-7	1	726 watts	6717 mm/min	0.6
1135-8	1	670 watts	6717 mm/min	0.65
1135-9	1	622 watts	6717 mm/min	0.7

Table 5.3 Processing Parameters for Multi Track Experiments

RDY	# of Tracks	Delivered Power	Beam Speed	Index
1135-10	3	1089 watts	6717 mm/min	0.5
1135-11	3	1089 watts	6717 mm/min	1.7
1135-12	3	1089 watts	6717 mm/min	2.5
1135-13	3	968 watts	6717 mm/min	0.5
1135-14	3	968 watts	6717 mm/min	1.7
1135-15	3	968 watts	6717 mm/min	2.5
1135-16	3	871 watts	6717 mm/min	0.5
1135-17	3	871 watts	6717 mm/min	1.7
1135-18	3	871 watts	6717 mm/min	2.5

CHAPTER VI

RESULTS AND DISCUSSION

This chapter gives the results of the numerical and experimental work done in Chapter V. Two sets of experimental data were acquired. In the first, single heat treated tracks were created at a constant beam speed and different beam powers. Since the absorptivity of the material is unknown (at least for the purposes of accurately modeling the thermal field), a series of differing beam powers indicates the sensitivity of the heat treating process to the amount of energy that is absorbed. In the second set of data, multitrack heat treating was performed using three different beam powers and three different overlap indices.

6.1 Single tracks

After processing, the samples were cross sectioned (plane perpendicular to the beam translation direction), mounted in a hot mount and sanded to a mirror finish using 800 grit sandpaper. The samples were then etched for 30 seconds using a 5% nital etchant (5 ml HNO_3 in 95 ml ethanol). Figure 6.1 is a photo of one such etch. Although a tophat profile was desired, it should be noted that the depths of the HAZ at the ends of the track are greater than the depths in the middle of the track, as is hinted at in Figure 6.1. For this reason, depths were measured at the center of the track, whenever possible (note given later).

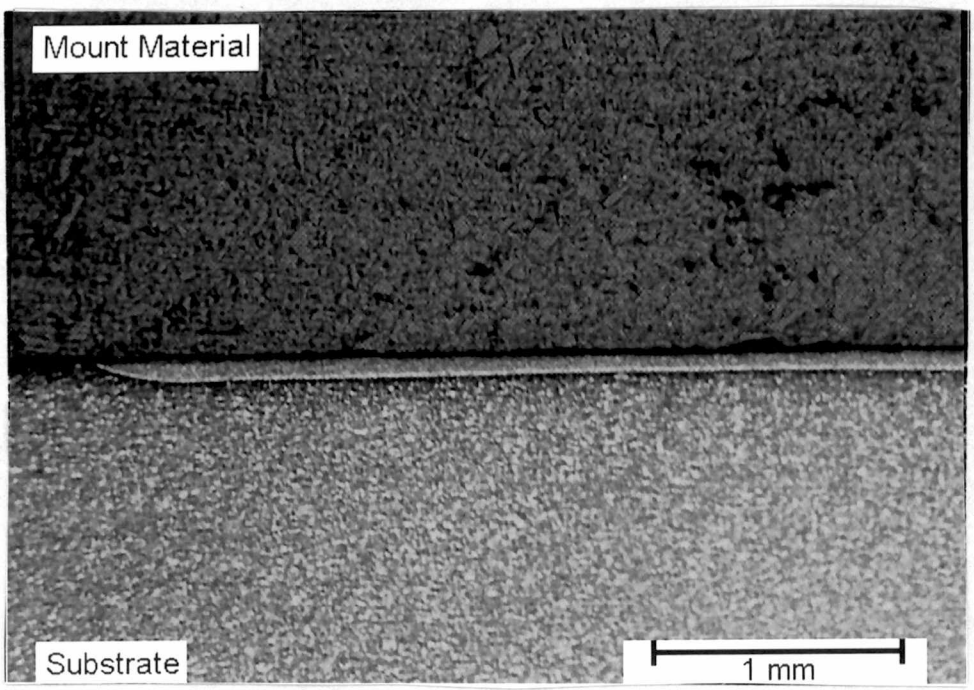


Figure 6.1: Image showing the heat affected zone for a single track. Processing conditions were 1452 W beam power and 6717 mm/min beam speed. The cross sectional surface has been polished and then etched (5% Nital) to give contrast between the base material ferrite and any other phases formed during processing.

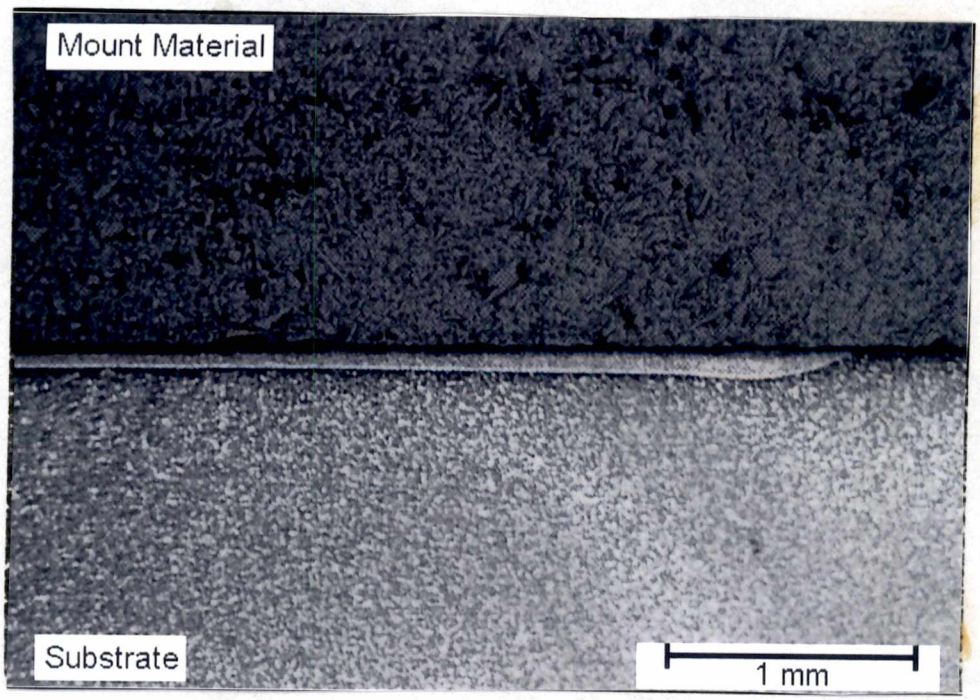


Figure 6.1 (continued)

Using other images like Figure 6.1, the depths of the HAZs were measured for all the different single track runs and are shown in Figure 6.2 (each run was measured twice, resulting in 2 data points for each unique beam power). Although there were nine different beam powers used, none of the lowest three powers (726 watts, 670 watts, and 622 watts) resulted in any discernible heat affected zone. For the other six runs, the HAZ depth increases linearly with beam power and increases from around 0.02 mm at 792 W to 0.07 mm at 1452 W.

6.2 Multiple Tracks

Using the three beam powers (1089 W, 958 W, and 871 W) that represent absorptivities the closest to the absorptivity used in the model (0.49), nine more experimental runs were done (three different indices at each of the three beam powers). Each complete track cycle (beam at the leading edge to beam at the leading edge for the next track) took 2.0 seconds. After sectioning, mounting, polishing, and etching the processed samples (done identically to the single tracks), the samples were again examined under a microscope. Figure 6.3 is a schematic showing the multiple track run process and a depiction of the resulting heat affected zone.

Figure 6.4 shows photos of the etched samples after processing (P = 968 W, 1.7 mm index and 6717 mm/min beam speed). As was mentioned earlier, there are two separate factors that change (increase) the HAZ depth of a track over the corresponding depth of its predecessor; a change in the absorption coefficient and a residual thermal field, both resulting from previous tracks. In Figure 6.4, the influence can clearly be

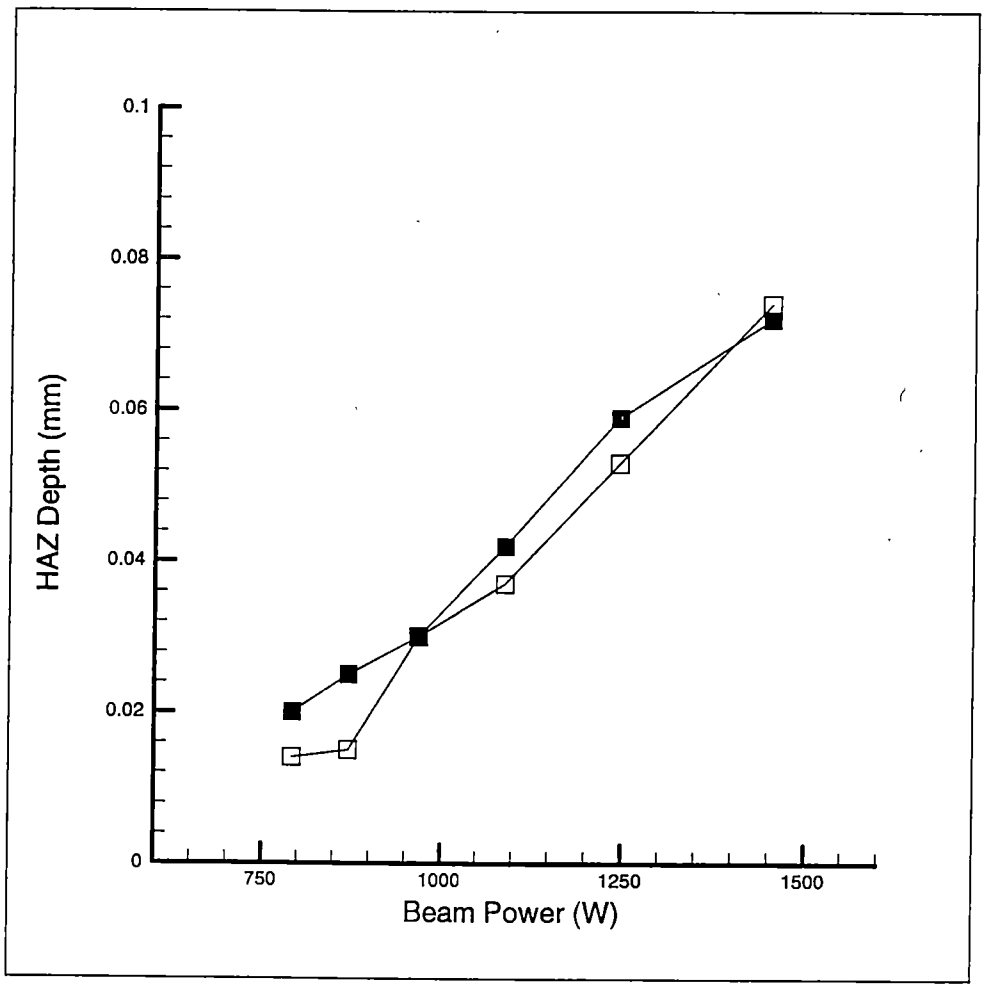
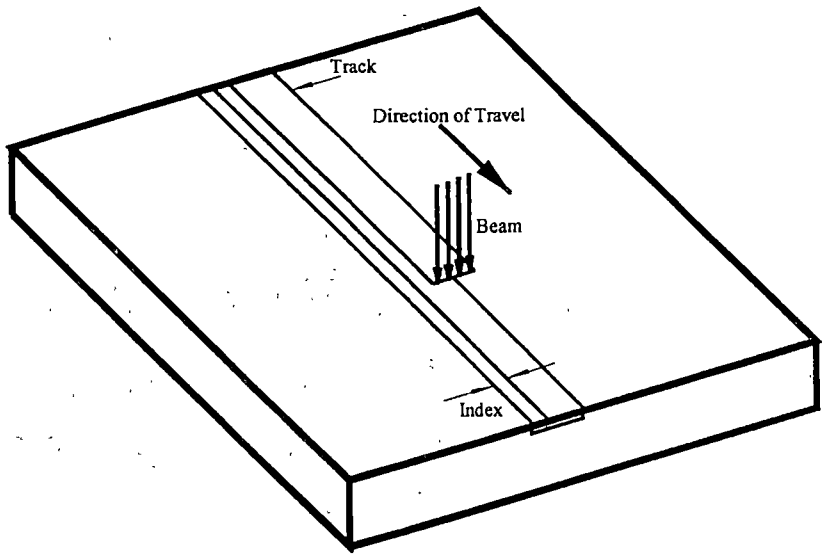
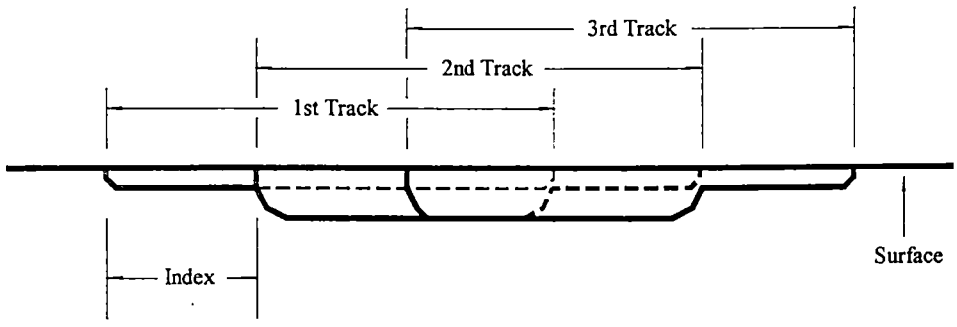


Figure 6.2: The track center depth of the heat affected zone at different beam powers. Beam powers below 792 W resulted in no discernible HAZ.



a)



b)

Figure 6.3: Schematics of multiple track runs (a) and resulting heat affected zone (b).

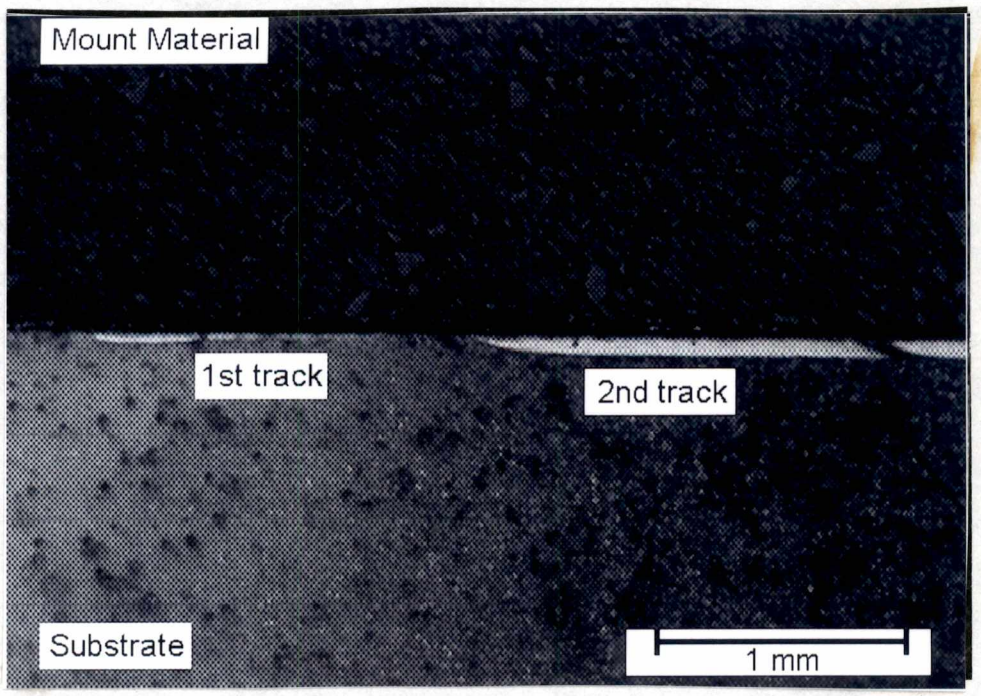


Figure 6.4: Image showing the HAZ for three overlapping tracks. The processing conditions were 968 W beam power, 6717 mm/min beam speed, and 1.7 mm index. The increased HAZ depth near the edges of the 1st and 3rd tracks are a result of the optics.

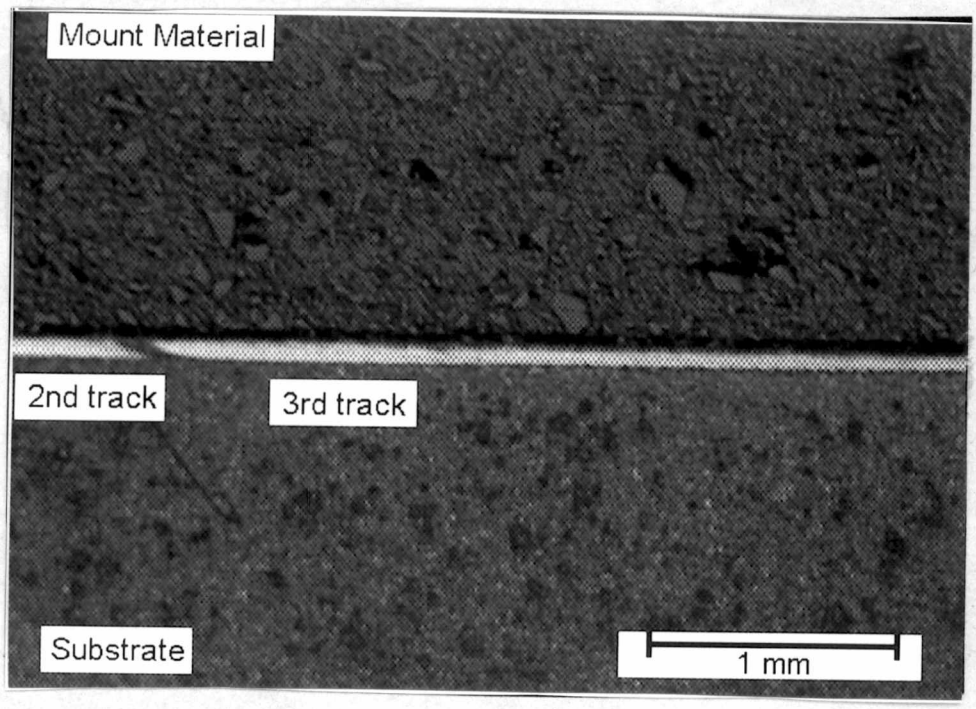


Figure 6.4 (continued)

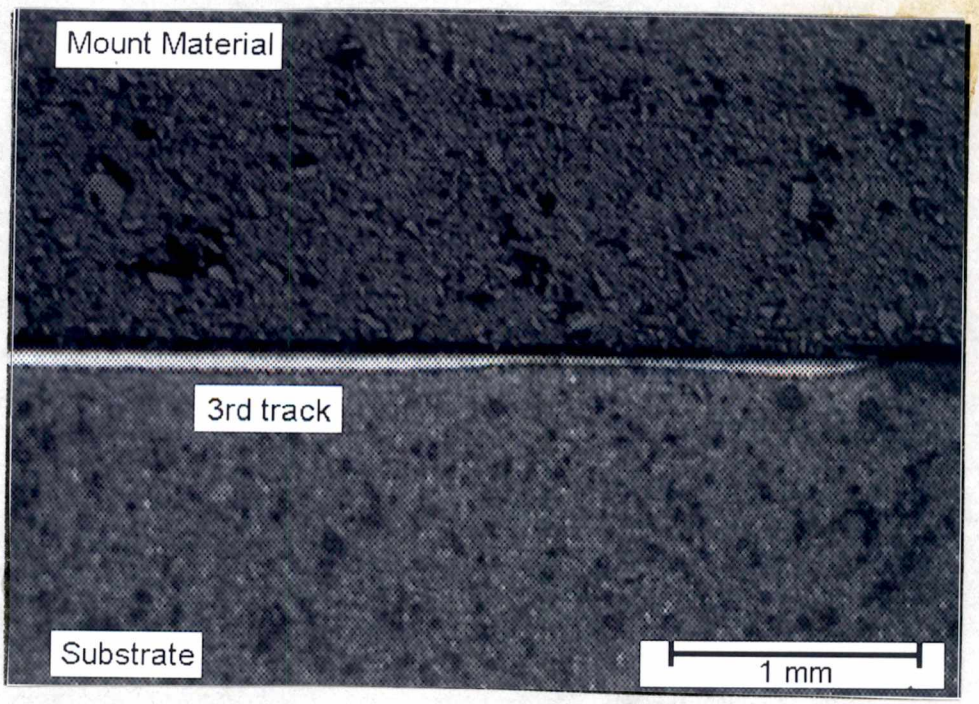


Figure 6.4 (continued)

seen, where the portion of the second and third track that overlap with previous tracks have greater HAZ depths than elsewhere.

Figure 6.5 shows the HAZ depths taken at, or as close to as possible, the track centers for the multitrack runs when the beam power was 871 watts. For the smallest overlap index (0.5mm), the beams overlap everywhere except the left 0.5 mm of the first track and the last 0.5 mm of the third. Unfortunately, this region corresponds to the "lobe" effect (an artifact of the optics used) so measurements are made as far from the beam edge, without going into the next track, as possible. Additionally, for the 2.5 mm index, the third track's measurement is made from within the region it overlaps with the second track. Figures 6.6 and 6.7 show the same depths for 968 and 1089 watts respectively. From the HAZ depths, the first track is uniformly the shallowest, while the second and third track depths are approximately the same.

6.3 Numerical Results

The numerical model was intended to discern the thermal effects of previous tracks on subsequent ones. Although adding the capability would not be troublesome, the model does not account for any change in absorption coefficient that might occur in overlap regions with prior tracks. Thus, it is able to differentiate between the effects of absorption coefficient from thermal field effects in overlapping tracks.

Figure 6.8 depicts peak temperature isotherm contours in the modeled process (beam power = 650 watts, absorption coefficient = 0.49, speed = 6500mm/min, 1.7 mm index). Although there is a hint of the bulk heating effect, indicated by the increase in

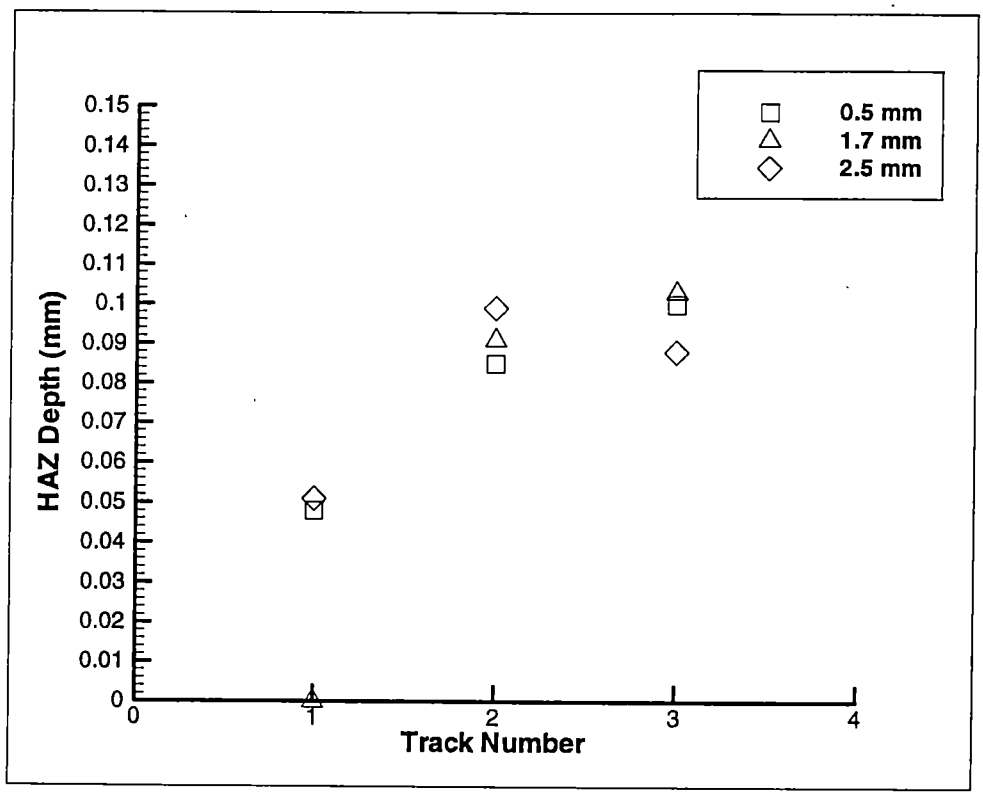


Figure 6.5: HAZ depths resulting from each track at various indeces using a 871 watt beam.

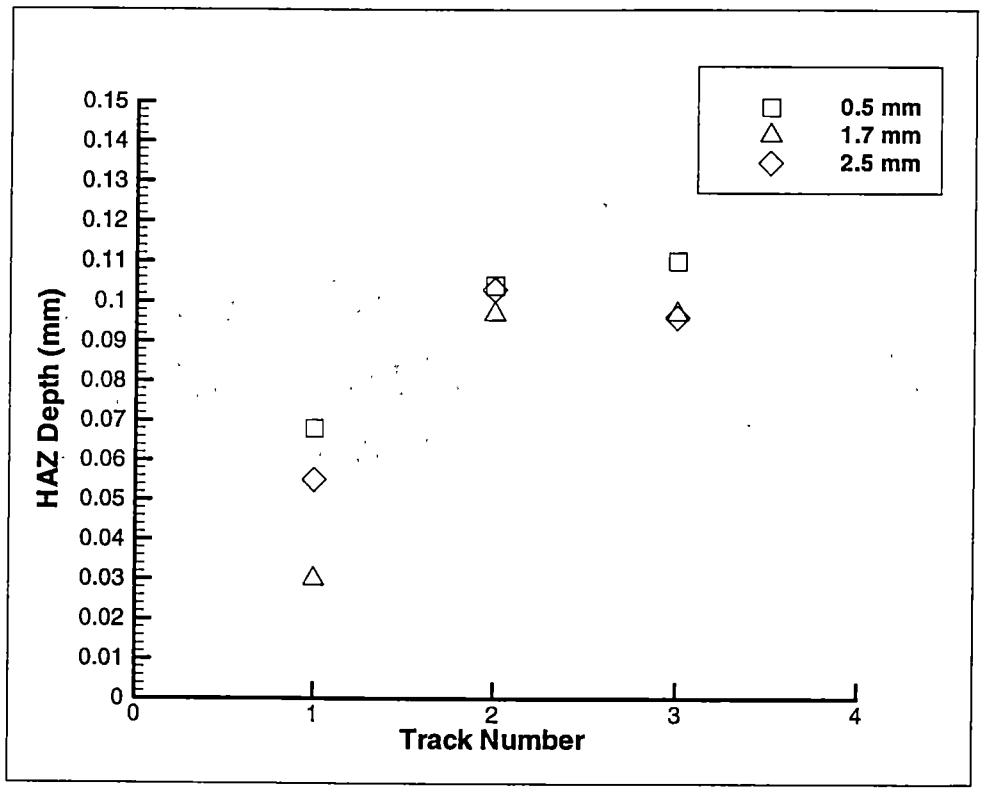


Figure 6.6: HAZ depths resulting from each track at various indeces using a 968 watt beam.

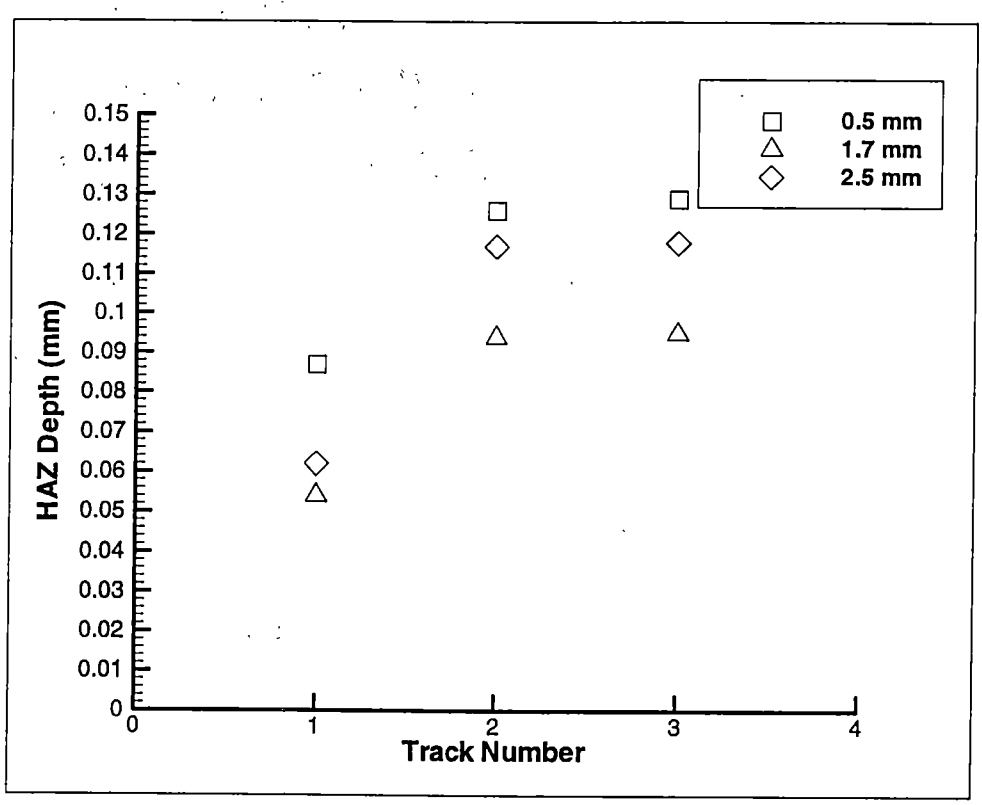


Figure 6.7: HAZ depths resulting from each track at various indeces using a 1089 watt beam.

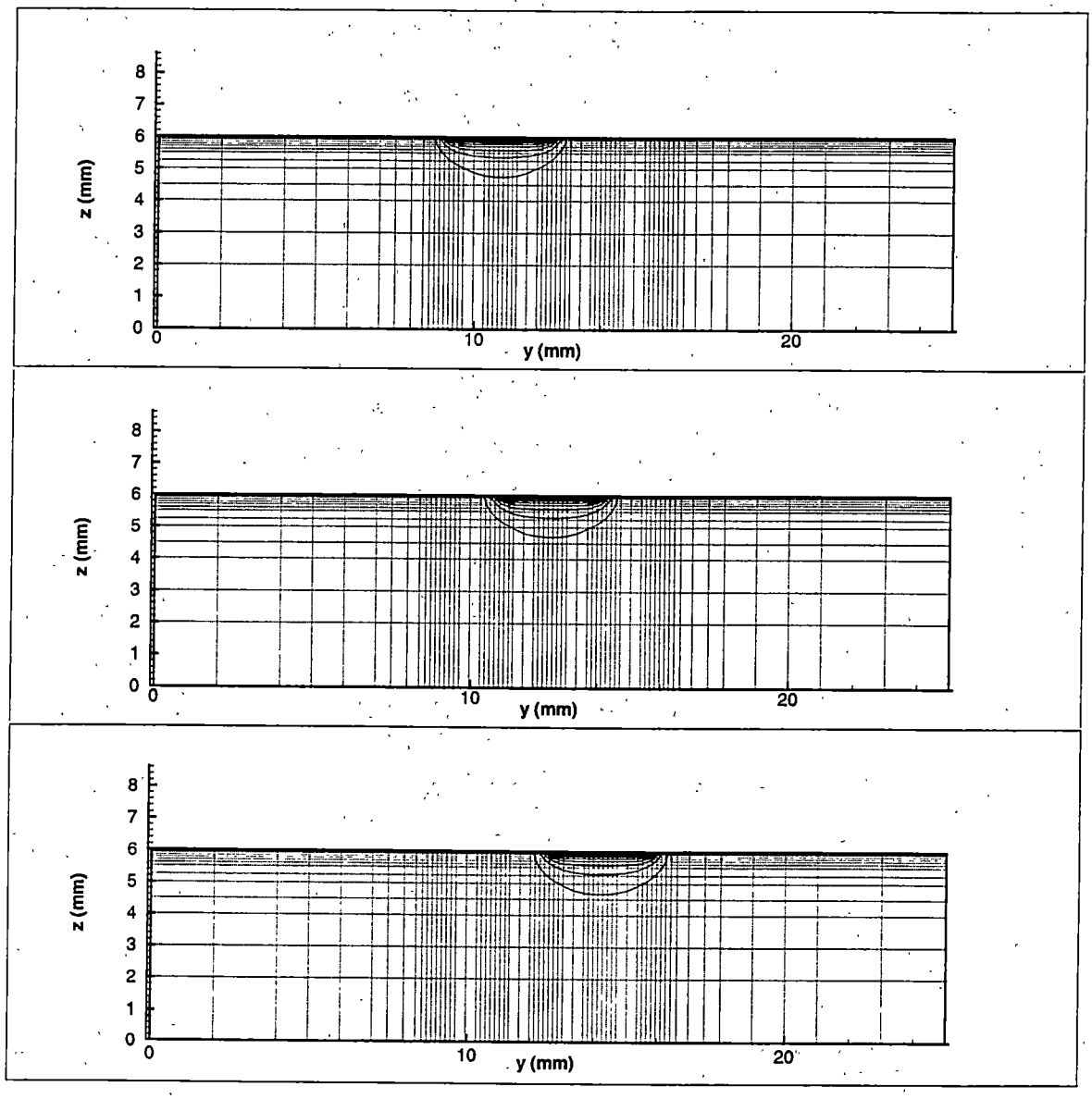


Figure 6.8: Peak temperature contour lines after the completion of the first, second, and third tracks respectively.

depth from the first track to the third of the coolest isotherm in Figure 6.8, Figure 6.9 indicates that any influence on HAZ depth, represented by the 1000 K isotherm, is small.

Figure 6.10 shows the peak temperatures in the sample near the surface. Although there is a temperature change at constant depths from one track to the next ("2nd track – 1st track" and "3rd track – 1st track") the difference is small compared to the slope of the curve at the transition temperature, which at 1000 K is 5000 K/mm. At that point, for example, a 5 K increase in temperature lowers the HAZ depth by 1 micron. Therefore, any change in HAZ depth due to the residual thermal field, for the limited number of tracks performed in this research, is small.

Bulk heating does influence the thermal field however. In Figure 6.11, the peak cooling rates are seen to be reduced from the first track to the second, and from the second to the third. Figure 6.12 further demonstrates the change by plotting a "peak cooling rate" profile from the surface into the material. Subsequent tracks experience lower cooling rates.

The bulk heating effect is additionally observed, albeit only slightly, by examining the amount of time any particular point spends above the transition temperature. A contour plot of these times is shown in Figure 6.13 while Figure 6.14 gives a profile from the surface down to the edge of the HAZ (as defined by the transition temperature isotherm) at the center of each of the tracks.

6.4 Discussion

Two important considerations become apparent when comparing the model with experimental results. First, although the cooling rates do change as a consequence of

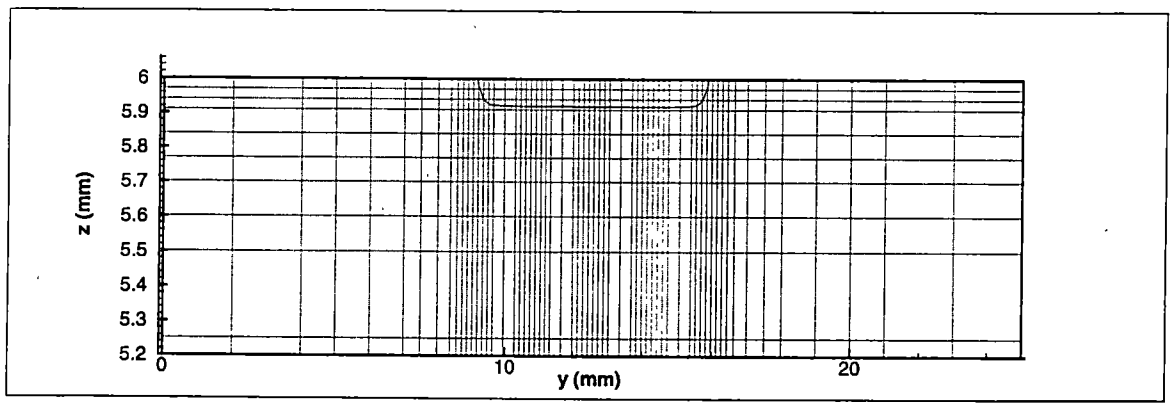


Figure 6.9: Cumulative 1000K isotherm depth. Bulk heating does not significantly increase the depth of the isotherm representing the traditional (slow heating rate) ferrite to austenite transition temperature. (Note: To exaggerate the depth of the isotherm, the z axis scale has been magnified by a factor of 10)

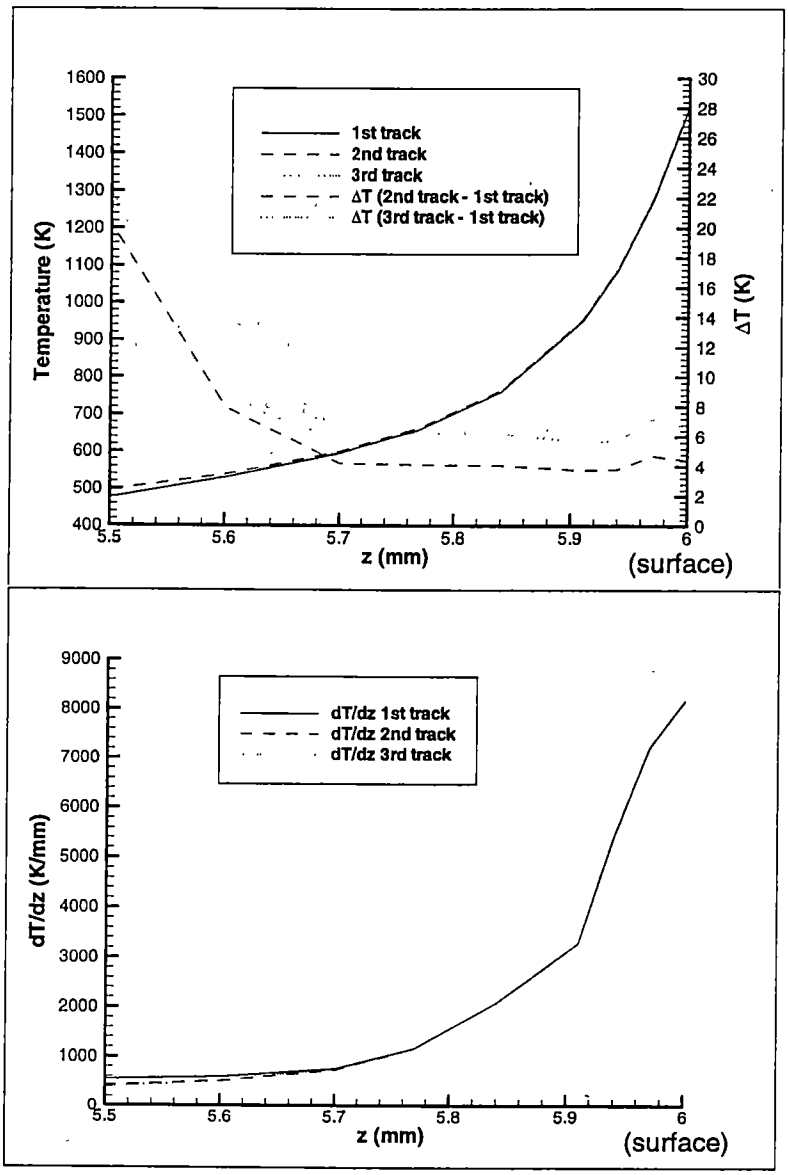


Figure 6.10: HAZ depth sensitivity to temperature changes resulting from bulk heating. In the top figure, the track center peak temperatures in the z direction are shown for the 0.5 mm closest to the surface. The temperature increases from the 1st track to the 2nd and 3rd are indicated by the ΔT curves. However, upon examination of the slope of the peak temperature curve (lower figure), at regions near 1000 K, the slope of the temperature curve is such that, at the temperature changes from the 1st to subsequent tracks (4 K to 6 K), the 1000 K isotherm depth is only increased by about 1 micron.

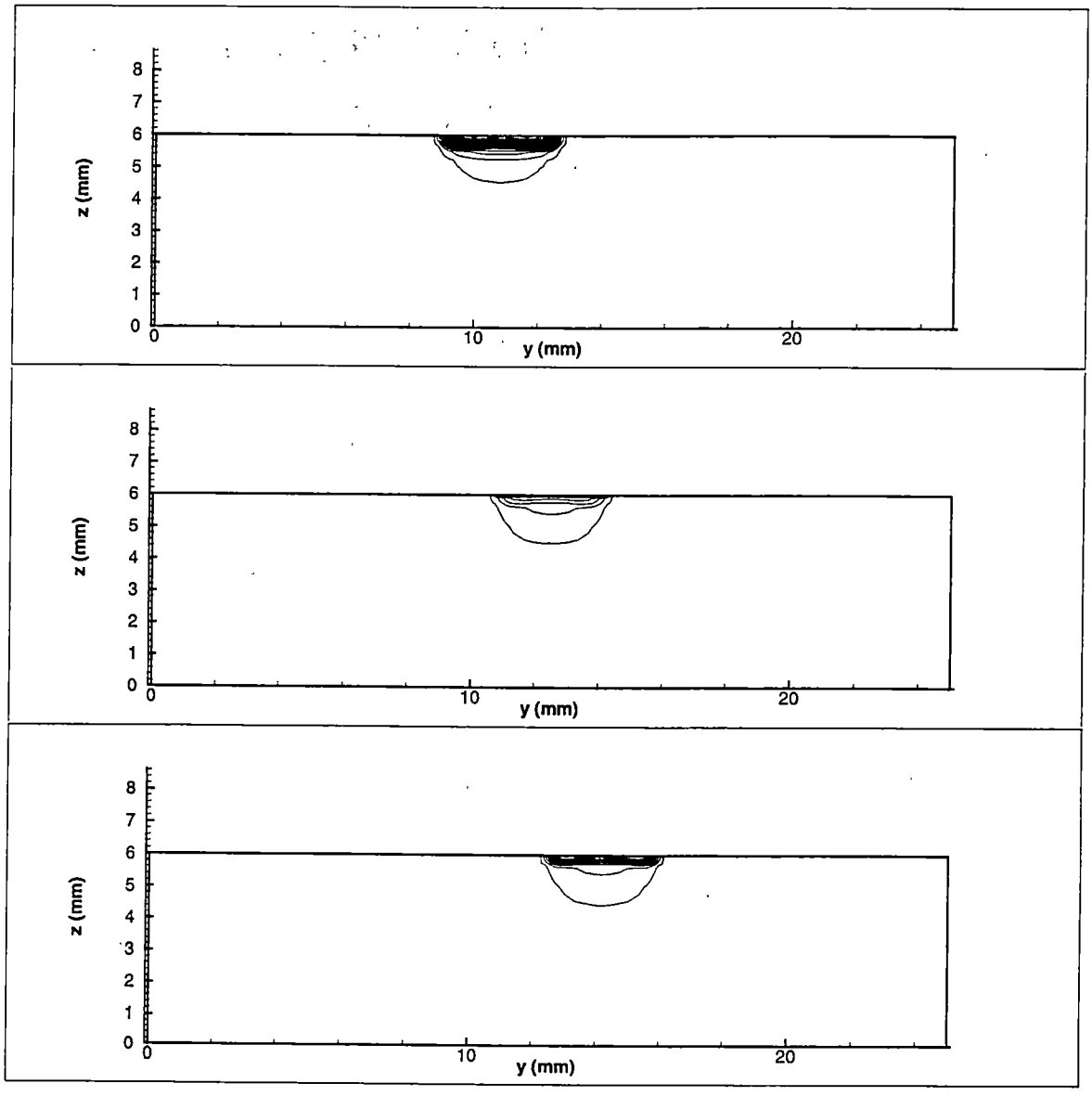


Figure 6.11: Peak cooling rate isolines after the completion of the first, second, and third tracks respectively. The decrease in cooling rates on subsequent tracks is indicated. The modeled processing parameters were 650 W, 0.49 absorptivity, 3.4 mm x 0.3 mm rectangular tophat beam profile, 1.7 mm index, and 6500 mm/min beam speed.

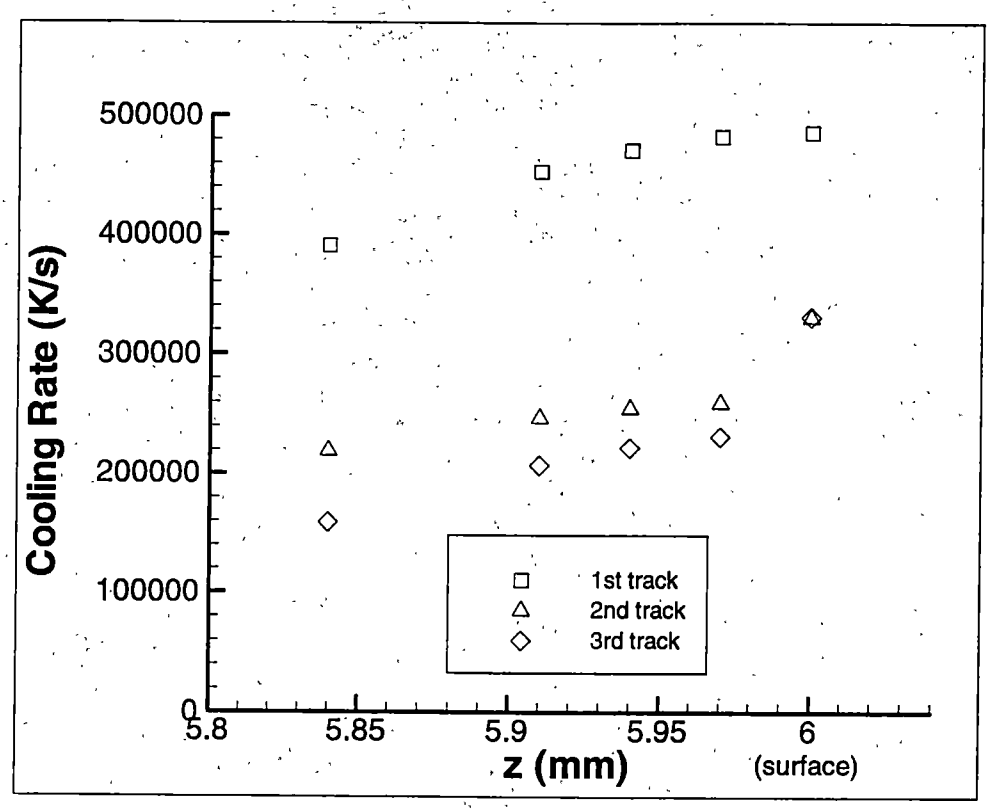


Figure 6.12: Cooling rates near the surface for each track. Bulk heating is indicated by the reduction in cooling rates in subsequent tracks.

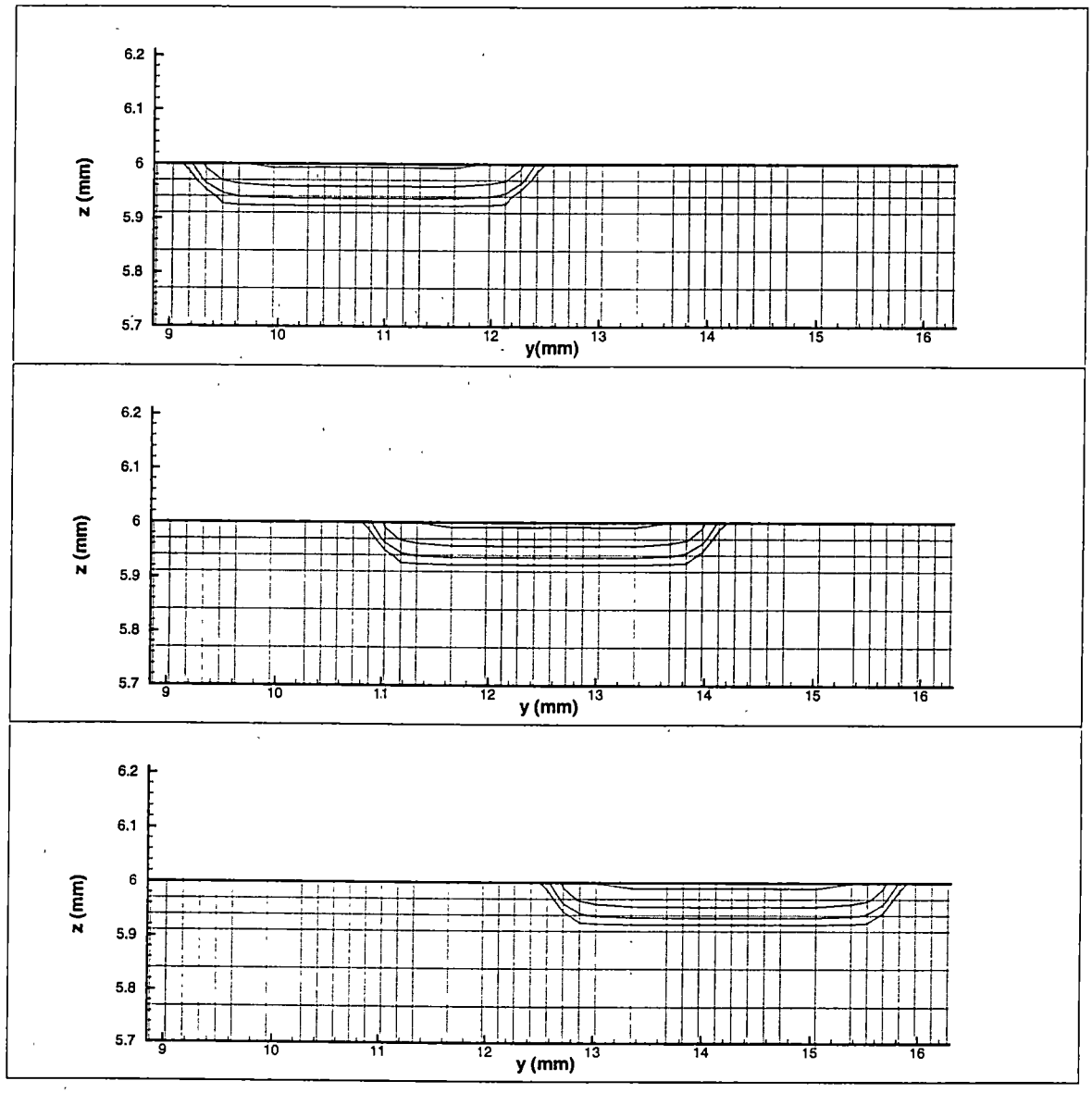


Figure 6.13: Time spent above 1000K. The contour lines are taken after the completion of the first, second, and third tracks respectively. Processing parameters were 650 W beam power, 0.49 absorption coefficient, 6500 mm/min beam speed, 3.4 mm x 0.3 mm rectangular tophat beam profile, and 1.7 mm index. (Note: The z axis has been scaled by a factor of 5 to exaggerate the depth of the isotherms)

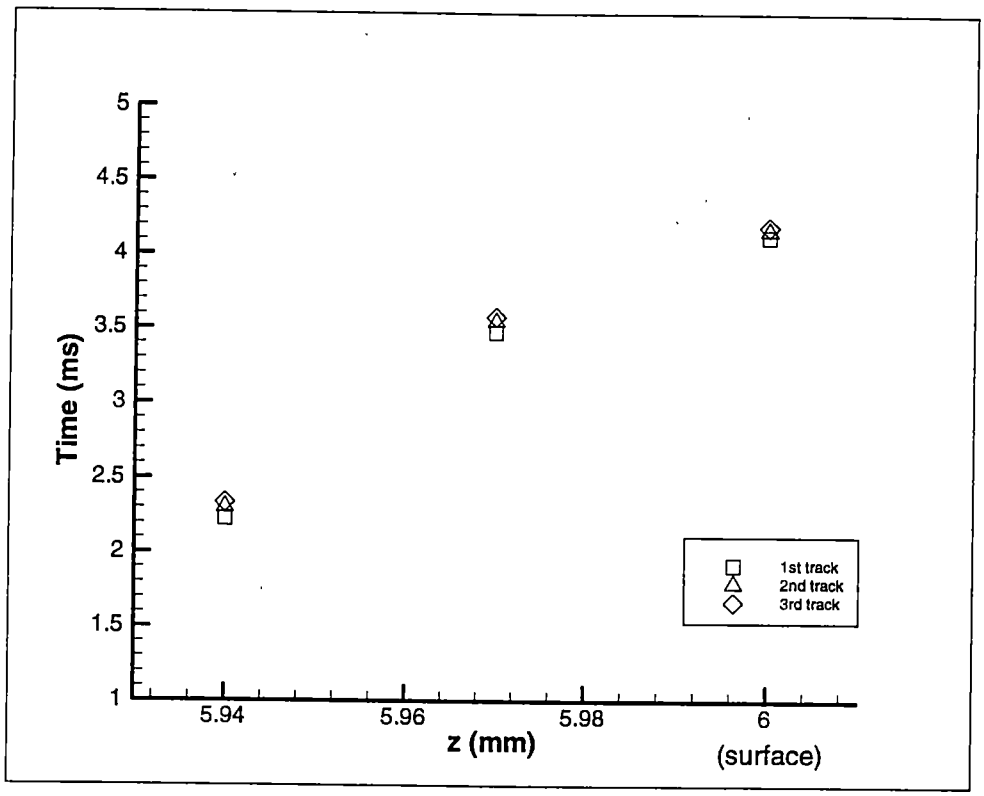


Figure 6.14: Influence of the track number on the amount of time spent above the 1000K isotherm. The time is insensitive to the track number. The amount of time is critical for the formation of phases which diffusion is important (eg. ferrite to austenite transformation).

bulk heating, the cooling rates everywhere are nevertheless several orders of magnitude higher than that required to transform austenite to martensite (Figure 3.7). Second, using the experimental HAZ depth in Figure 6.2, along with the model temperature at that depth, it is possible to produce Figure 6.15, which indicates what the transition temperature (which defines the edge of the HAZ) is depending on the absorption coefficient. Assuming the absorption at 1.06 microns in 1050 steel is between 0.3 and 0.55, the transition temperature is between 1020 K and 1400 K.

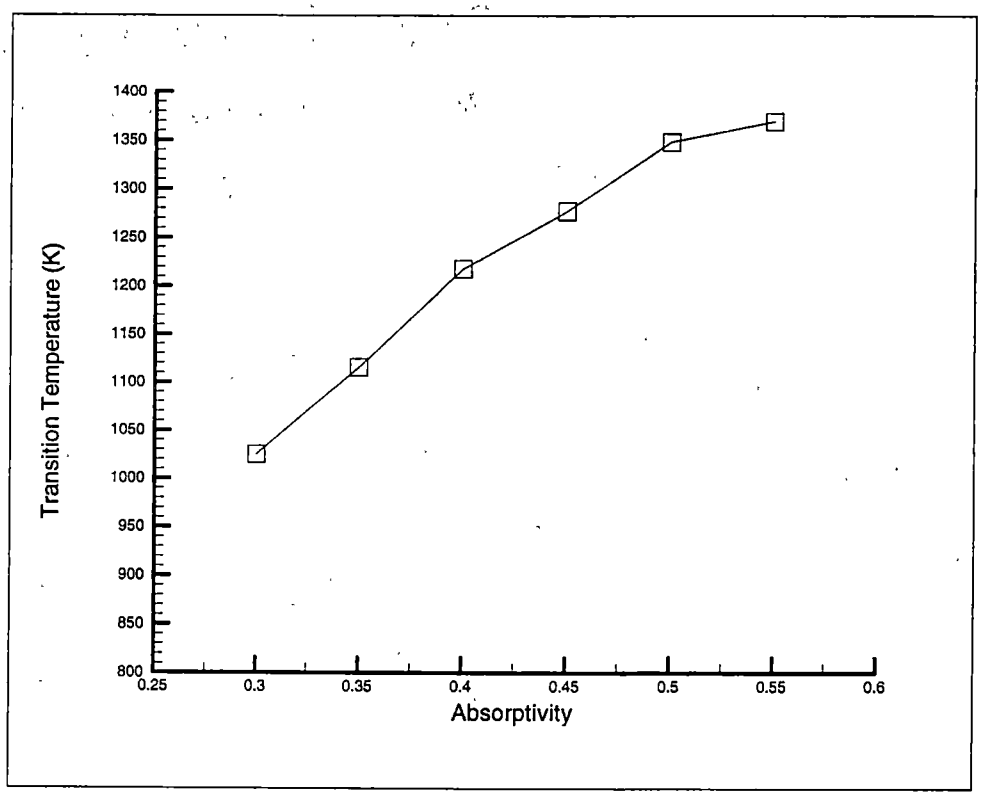


Figure 6.15: Predicted transition temperature from different absorption coefficients. For an absorption coefficient of 1.06 micron wavelength incident on 1050 steel between 0.3 and 0.55, the transition temperature for the heat affected zone is between 1020 K and 1400 K.

CHAPTER VII

CONCLUSION

The purpose of this research was to determine possible effects of the unique characteristics of laser heat treating on AISI 1050 steel.

Three possible characteristics of laser heat-treating were identified that differed from traditional heat-treat processes. First, the heating rate for laser heat treating is high in comparison to the isothermal conditions typical of traditional heat treating. Second, the amount of time available for diffusion transformations to occur in laser heat treating is predicted to be small compared to those available in traditional heat treating. And third, bulk heating resulting from numerous heat treat cycles may alter the quenching affect from the start to the finish.

Addressing these characteristics, a solution approach that combined experimental and numerical processes was created. Experiments were performed on small coupons of AISI 1050 steel, both single and multiple tracks using a Nd:YAG laser at various beam powers. A computational heat transfer model that determined the thermal field within a processed sample was created using a commercial CFD code.

Combining the HAZ depth from experimental runs at different beam powers with the calculated temperature at those depths, the temperature at which the base ferrite in 1050 steel transforms to other phases is seen in Figure 6.15 to be between 1020 K and 1400 K for an absorption coefficient between 0.3 and 0.55.

The model predicts very little time is spent above 1000 K, suggesting that, even if the temperature at which ferrite transforms to austenite were unchanged, very little (if

any) austenite will form. Therefore, the HAZ is expected to be composed predominantly of phases other than martensite, since the austenite precursor has little opportunity to form.

However, despite bulk heating, the predicted cooling rates are much higher than that indicated in Figure 3.5 as sufficient for complete transformation of austenite into martensite. Therefore any austenite that does form, however little, would be expected to change to martensite.

There are several areas for future work that need investigation. The number of tracks studied in this project was limited. Future work may indicate numerous tracks cause sufficient bulk heating to occur that lowers the quench effectiveness of the bulk material. In addition a future model could incorporate possible changes in the absorption coefficient from both oxidation and different phase composition. Also, an analysis that identifies the evolved solid phases could be correlated to specific temperatures to determine how the transition temperatures for different transformations are individually influenced by the high heating and cooling rates.

Another direction for further research would involve altering the model to incorporate a "moving grid". As some of the results in chapter IV indicate, both a small time step and, in the vicinity of the beam, a small grid spacing is needed to capture the actual temperature field while processing. A static grid, like used in this research, consumes (and wastes) a tremendous amount of memory by having small grid space cells in regions far from the beam. A moving grid would permit the cell spacings around the beam to decrease, while freeing up memory by reducing the number of cells elsewhere. This would improve the calculation accuracy, reduce the storage requirements, and

improve the calculation speed. All of these as well as a finer grid will be necessary to model solid to liquid and liquid to gas phase changes, another topic for future consideration.

LIST OF REFERENCES

[1] Oshea, Callen, Rhodes. An Introduction to Lasers and Their Applications. (Reading, MA: Addison Wesley, 1978) 251-261.

[2] JA Hopkins, M Murray, MH McCay, N Dahotre. "Laser processed aluminum surfaces in automotive applications: Performance requirements for cylinder bores and valve seats". Society of Automotive Engineers. 98SAM-123. (1998).

[3] Brooks, C.R. Principles of the Heat Treatment of Plain Carbon and Low Alloy Steels. (Materials Park, OH: ASM International, 1996) 9.

[4] Brooks, 209.

[5] Brooks, 215.

[6] Jon Winkler, "A Temperature Study of Laser-Irradiated Bone." Diss. University of Tennessee, 1997.

[7] D Rosenthal. "The theory of moving sources of heat and its application to metal treatments". Transactions of the ASME. Nov 1946, 849-866.

[8] HS Cline, TR Anthony. "Heat treating and melting material with a scanning laser or electron beam". J Appl Physics, Vol 48, 1977. 3895-3900.

[9] O Manca, B Morrone, and V Naso. "Quasi-steady-state three dimensional temperature distribution induced by a moving circular Gaussian heat source in a finite depth solid". Int J of Heat Mass Transfer. Vol 38, no 7 1995. 1305-1315.

[10] SM Zubair, MA Chaudhry. "Heat conduction in a semi-infinite solid due to time-dependent laser source". Int J of Heat Mass Transfer. Vol 39, No 14, 1996, 3067-3074.

[11] SM Zubair, MA Chaudrhy. "Temperature solutions due to time-dependent moving-line-heat sources". Heat and Mass Transfer. Vol 31 1996, 185-189.

[12] MA Chaudhry, SM Zubair. "Heat conduction in a semi-infinite solid subject to time-dependent boundary conditions". HTD-Vol 207. Fundamental Problems in Conduction Heat Transfer. ASME 1992. 77-83.

[13] I Chen, S Lee. "Transient temperature profiles in solids heated with scanning laser". J Appl Physics. Vol 54, 1983. 1062-1066.

[14] YI Nissim, A Lietoila, RB Gold, and JF Gibbons. "Temperature distributions produced in semiconductors by a scanning elliptical or circular CW laser beam". J Appl Physics, Vol 51, 1980. 274-279.

[15] M. Lax. "Temperature rise induced by a laser beam". Journal of Applied Physics. Vol. 48, No 9, Sept 1977. 3919-3924.

[16] M. Lax. "Temperature rise induced by a laser beam II. The nonlinear case". Appl Phys Lett 33(8) 15 October 1978. 786-788.

[17] JE Moody and RH Henkel. "Temperature profiles induced by a scanning CW laser beam". J Appl Physics, Vol 53, 1982. 4364-4371.

[18] MF Ashby, KE Easterling. "The transformation hardening of steel surfaces by laser beams – I. Hypo-eutectoid steels". Acta metall. Vol. 32, No 11, 1984, 1935-1948.

[19] TW Abou-Arab, MA Al-Nimr. "A study of a multidimensional transient heat conduction problem with a moving heat source Part 1: Analytical solution". Materials at High Temperatures. Vol. 9, No 1, 1991. 35.

[20] C Maier, P Schaaf, U Gonser. "Calculation of the temperature profile for laser treatment of metallic samples". Material Science and Engineering. A150, 1992, 271-280.

[21] A Kar, J Mazumder. "Three-dimensional transient thermal analysis for laser chemical vapor deposition on uniformly moving finite slabs". J Appl Phys. Vol. 65, No 8, April 1989. 2923-2934.

[22] TW Abou-Arab, KM Saleh, I Ramadan. "A study of a multidimensional transient heat conduction problem with a moving heat source Part 2: Numerical and experimental". Materials at High Temperatures. Vol. 9, No 1, 1991. 41.

[23] P Ehrard, C Holle, C Karcher. "Temperature and penetration depth prediction for a three-dimensional field below a moving heat source". Int. J Heat Mass Transfer. Vol. 36, No 16, 1993, 3997-4008.

[24] J Mazumder and WM Steen (1980). "Heat transfer model for CW laser materials processing". J Appl Physics. Vol. 51, No 2. 947-952.

[25] O Manca, B Morrone, S Nardini. "Thermal models in moving heat sources with high peclet numbers". Presented at the 1995 ASME International Mechanical Engineering Congress & Exposition. San Francisco, CA. Nov 12-17, 1995.

[26] S Kou, DK Sun, YP Lee. "A fundamental study of laser transformation hardening". Metallurgical Transactions A. Vol. 14A April 1983. 643-653.

[27] P Michaleris, A DeBiccari. "Prediction of welding distortion". Welding Research Supplement. April 1997. 172s-.

[28] N Pirch, EW Kreutz, X He, BL Mordike. "The modeling of heat-momentum, and solute transport in laser surface alloying". Modeling of casting, welding and advanced solidification processes VII. Cross and Campbell (eds). The minerals, metals, and materials society, 1995, 47.

[29] C Chan, J Mazumder, MM Chen. "A two-dimensional transient model for convection in laser melted pool". Metallurgical Transactions A. Vol. 15A December 1984. 2175-2185.

[30] ME Thompson, J Szekely. "The transient behavior of weldpools with a deformed free surface". Int J Heat Mass Transfer. Vol. 32, No 6, 1989, 1007-1019.

[31] Brooks, 221.

[32] Brooks, 215.

[33] CFDAce Theory Manual V4.0 (Huntsville, Al: CFDRC, 1998)

[34] Hirsch, C. Numerical Computation of Internal and External Flows: Volume 1. Fundamentals of Numerical Discretization. (New York, NY: John Wiley and Sons, 1988). 240

[35] Incropera, F.P. and D.P. Dewitt. Fundamentals of Heat and Mass Transfer, 4th Ed. (New York, NY: John Wiley and Sons, 1996).

[36] Omega Engineering: http://www.omega.com/literature/transactions/volume1/emissivitya.html

[37] WR Wade, "Measurements of Total Hemispherical Emissivity of Various Oxidized Metals at High Temperatures", NACA TN 4206. Mar 1958. 46

[38] Electro-Optical: http://www.electro-optical.com/bb_rad/emissivity/matlemisivty.htm

[39] MR Frewin, DA Scott. "Finite Element Model of Pulsed Laser Welding". Welding Research Supplement. Jan 1999. 15-22.

[40] MAPP: Properties of Engineering Materials. Ver 1.1. ESM Software, Hamilton OH.

APPENDICES

APPENDIX A

USER BOUNDARY CONDITION

This section describes the boundary condition used to model the processed surface. In particular, the equations are adapted for use as a flux boundary condition to be used in CFD-ACE's User Boundary Condition.

In Chapter 3, equation 3-3 and 3-4 described the energy distribution for a rectangular tophat and elliptical Guassian beam respectively. Repeated here, they were:

$$(A-1) \qquad q''(x,y,t) = \frac{\alpha P(t)}{4x_r y_r} \qquad |x - x_b(t)| < x_r \quad and \quad |y - y_b(t)| < y_r$$
$$= 0 \qquad otherwise.$$

$$(A-2) \qquad q''(x,y,t) = \frac{\alpha P(t)}{\pi x_r y_r} \exp\left\{ -\frac{[x - x_b(t)]^2}{x_r^2} - \frac{[y - y_b(t)]^2}{y_r^2} \right\}.$$

where α is the spectral absorption coefficient, P(t) is the time dependent beam power (beam may be turned off during some periods), and x_r and y_r are either the 1/e radii (Guassian) or ½ the width and length (rectangular) of the beam. The position of the center of the beam is at $x_b(t)$,$y_b(t)$. Although only the rectangular tophat beam was used in the project, both beam types are actually coded into the modified solver and consequently described here.

For both cases, it is assumed there is a rectangular grid distribution with cell centers located at $x_c(i,j)$ and $y_c(i,j)$ and cell widths and lengths of $\Delta x(i,j)$ and $\Delta y(i,j)$. When the input file specifies "Q = user_defined" (see Appendix B) CFD-ACE accesses

the user defined boundary condition to determine what the flux for that boundary. Unique fluxes may be calculated for each cell.

Rectangular Tophat

When a cell falls entirely outside of the beam, the flux for the cell resulting from the beam is zero. When the cell falls completely within the beam, the beam flux for that cell, f(i,j), is

$$f(i,j) = \frac{P(t)}{4x_r y_r} \qquad (A-3)$$

However, when the edge of the beam passes within a cell, a scheme must be employed in order to account for the non-uniformity of the beam distribution across the cell. Since CFDACE requires a constant flux to be specified across the entire cell, it is necessary to reduce the intensity of the beam in the cells where the beam edge falls in order to conserve energy.

Defining the intersection area between the beam and a grid cell to be A_{int}, the flux due to the beam for such a cell can be written as

$$f(i,j) = \frac{P(t)}{4x_r y_r} \frac{A_{int}}{\Delta x(i,j)\Delta y(i,j)}. \qquad (A-4)$$

The advantage of this is that it can be used everywhere. When the cell falls completely within the beam, $A_{int} = \Delta x(i,j)*\Delta y(i,j)$. When the cell is entirely outside the beam, A_{int} is zero.

Guassian Beam

An altogether different scheme is used for the Guassian beam. Since this project involves a numerical solution anyway, it is appropriate to ask the question, "How small should the grid cells be so that using the Gaussian intensity at the cell center across the entire cell results in a total energy approximately equal to the beam power, P?". Expressed mathematically, what values for Δx and Δy result in

$$(A-5)\quad \int_{-\infty}^{\infty}\int_{-\infty}^{\infty} I_0 e^{\left[-\left(\frac{x-x_b(t)}{x_r}\right)^2-\left(\frac{y-y_b(t)}{y_r}\right)^2\right]}dxdy \approx \sum_{i=1}^{Imax}\sum_{j=1}^{Jmax} I_0 e^{\left[-\left(\frac{x_c(i,j)-x_b(t)}{x_r}\right)^2-\left(\frac{y_c(i,j)-y_b(t)}{y_r}\right)^2\right]}\Delta x(i,j)\Delta y(i,j)$$

where $x_b(t)$, $y_b(t)$ is the beam position and $x_c(i,j)$,$y_c(i,j)$ is the cell center location. It is easy to show (though not included here) that, for a constant cell spacings, Δx and Δy, the summation differs from the integral by less than 1% when

$$(A-6)\qquad \frac{\Delta x}{x_r} \le 1 \quad and \quad \frac{\Delta y}{y_r} \le 1.$$

So long as the cell spacings in each direction are smaller than the Guassian beam radii to the 1/e points, reasonable accuracy is obtained by using the intensity of the beam at the cell center across the entire cell. Although the tophat beam used throughout this project, it is clear from Chapter 4 (which also used a rectangular tophat beam) that grid sizes are smaller than that expressed in eq. A-6. Therefore, it is possible to express the beam flux for each cell using the equation:

$$(A-7)\qquad f(i,j)=\frac{P(t)}{\pi x_r y_r}\exp\left[-\left(\frac{x_c-x_b(t)}{x_r}\right)^2-\left(\frac{y_c-y_b(t)}{y_r}\right)^2\right].$$

These equations (A-4 and A-7) will be found in the following source code, the user defined boundary condition modification to the flow solver.

```
C-----------------------------------------------------------------

      SUBROUTINE ubound(BCINDX,IVAR,I,J,K)
      IMPLICIT DOUBLE PRECISION (A-H, O-Z)
      IMPLICIT INTEGER (I-N)
      LOGICAL ERROR
      INTEGER BCINDX
C
C       P = Beam power (Watts)
C       xr = x direction elliptical radius to 1/e (m)
C       yr = y direction elliptical radius to 1/e (m)
C       von = beam velocity in x direction while beam is on (m/s)
C       voff = beam velocity in x direction while beam is off (m/s)
C       oi = overlap index (m)
C       d = distance beam moves in x direction (m)
C       x0,y0 = initial beam location (m,m)
C       emm = total hemispherical emmisivity (unitless)
C       absor = spectral absorptivity (unitless)
C       Ts = radiative background temperature (K)
C       h = convective heat transfer coefficient (W/m^2K)
C       Ta = freestream ambient temperature (K)
C       itype = beam type (1 = Guassian, 2= rectangular tophat)

C       pi = 3.141592654
C       sigma = Stefan Boltzman constant (W/m^2K^4)
C       time_on = Amount of time each cycle beam is on (s)
C       time_off = Amount of time each cycle beam is off (s)
C       time_cycle = Total time to complete one cycle (s)
C       num_complete_cycles = Number of already completed
C             cycles
C       time_this_cycle = Time from start of current cycle (s)
C       time_off_this_cycle = time since beam turned off (s)
C       xb,yb = current beam location (m,m)
C       ibeam = flag to turn of beam during return trip (unitless)
C       beam_intensity = Peak beam intensity, I0 (W/m^2)
C       beam_flux = amount of beam energy delivered to cell
C             face (W/m^2)
C       convection_loss = net energy exchange due to convection
```

```
C               (W/m^2)
C       radiation_loss = net energy exchange due to radiation
C               (W/M^2)
C       flux_net = net energy exchange for cell face (W/m^2)
C       THIS IS THE SET BC, Q=flux_net
C

C       Define a few constants
        pi    = 3.141592654
        sigma = 5.67e-8

C       Get the processing parameters specified in the input file
        call get_ruser(1,P)
        call get_ruser(2,xr)
        call get_ruser(3,yr)
        call get_ruser(4,von)
        call get_ruser(5,voff)
        call get_ruser(6,oi)
        call get_ruser(7,d)
        call get_ruser(8,x0)
        call get_ruser(9,y0)
        call get_ruser(10,emm)
        call get_ruser(11,absor)
        call get_ruser(12,Ts)
        call get_ruser(13,h)
        call get_ruser(14,Ta)
        call get_iuser(1,itype)

C       Determine which domain the boundary condition is being
C               set for.
        call get_active_domain(idomain)

C       Determine the CFDACE variable index for these variables
        call get_var_index('T',ind_t)
        call get_var_index('XG',ind_x)
        call get_var_index('YG',ind_y)

C       Determine the current time.
        call get_time(time,itime)

C       What temperature is this cell?
        call get_bc(bcindx,ind_t,i,j,k,T)

C       What is the location of this cell?
        call get_value_one_cell(ind_x,idomain,i,j,k,xx,error)
        call get_value_one_cell(ind_y,idomain,i,j,k,yy,error)
```

```
C       Determine the current beam center position.
        time_on    = d/von
        time_off   = d/voff
        time_cycle = time_on + time_off

        num_complete_cycles = int( time/time_cycle )
        time_this_cycle = time - time_cycle*num_complete_cycles

        if (time_this_cycle.gt.time_on) then
              time_off_this_cycle = time_this_cycle - time_on
              xb = x0 + d - voff*time_off_this_cycle
              yb = y0 + oi*num_complete_cycles
              ibeam = 0
        else
              ibeam = 1
              xb = x0 + time_this_cycle*von
              yb = y0 + oi*num_complete_cycles
        end if

        if (itype.eq.1) then

C       Calculate the beam flux for the Guassian beam
              beam_intensity = P/pi/xr/yr * ibeam
              beam_flux = beam_intensity*exp(-((xx-xb)/xr)**2-((yy-yb)/yr)**2)

        elseif (itype.eq.2) then

C       Calculate the beam flux for the rectangular tophat beam
C       Note that cell dimensions aren't stored, only the cell face areas.
C       Therefore a little algebraic manipulation is necessary to determine
C             the cell dimensions.

              call get_var_index('AREAW',ind_aw)
              call get_var_index('AREAS',ind_as)
              call get_var_index('AREAL',ind_al)
              call get_value_one_cell(ind_aw,idomain,i,j,k,ax,error)
              call get_value_one_cell(ind_as,idomain,i,j,k,ay,error)
              call get_value_one_cell(ind_al,idomain,i,j,k,az,error)
              wx = .5*sqrt(ay*az/ax)
              wy = .5*sqrt(ax*az/ay)
              cell_area = az
C             write(*,*) '***',i,j,wx,wy,cell_area

C       Define the beam and cell boundary locations and calculate the
C             intersection area and intensity for the cell.
```

```
        xw = xx - wx
        xe = xx + wx
        yn = yy + wy
        ys = yy - wy
        xbw = xb - xr
        xbe = xb + xr
        ybs = yb - yr
        ybn = yb + yr
        wx = 0.0
        wy = 0.0
        if(xw.le.xbw.and.xe.gt.xbw.and.xe.le.xbe) wx=xe-xbw
      if(xw.le.xbw.and.xe.gt.xbw.and.xw.le.xbe.and.xe.gt.xbe) wx=xbe-xbw
        if(xw.gt.xbw.and.xe.le.xbe) wx=xe-xw
        if(xw.gt.xbw.and.xw.le.xbe.and.xe.gt.xbe) wx=xbe-xw
        if(ys.le.ybs.and.yn.gt.ybs.and.yn.le.ybn) wy=yn-ybs
        if(ys.le.ybs.and.yn.gt.ybs.and.ys.le.ybn.and.yn.gt.ybn) wy=ybn-ybs
        if(ys.gt.ybs.and.yn.le.ybn) wy=yn-ys
        if(ys.gt.ybs.and.ys.le.ybn.and.yn.gt.ybn) wy=ybn-ys
        area_inter = wx * wy
        beam_intensity = P/xr/yr/4 * ibeam
        beam_flux = beam_intensity * area_inter / cell_area
else
        write(*,*) 'Invalid beam type'
end if

beam_flux = absor*beam_flux
convection_loss = h*(T - Ta)
radiation_loss  = emm*sigma*(T**4 - Ts**4)
flux_net = beam_flux - convection_loss - radiation_loss
call set_bc(flux_net)

RETURN
END
```

APPENDIX B

MODIFIED INPUT FILE

Below is a typical input file used in this project. The bold and italicized lines indicate additions to the input file once the use of GUI is complete. Lines beginning with an asterisk, *, are "commented" and ignored by the solver.

```
TITLE "
*
*
*
*
*
********************* Model ***********************
*
*
MODEL overlap
*
* Define the processing parameters
PARAMETERS
 REAL P=650,ITYPE=2,XR=0.00015,YR=0.0017
 REAL VON=0.10833333,VOFF=0.01101695
 REAL INDEX=0.0017,DIST=0.025
 REAL XINIT=0.00,YINIT=0.0108
 REAL EMMISIVITY=0.4,ABSOR=.49, TSURR=293.
 REAL HTC=10.0, TAIR=293.
END
*
* Pass the processing parameters into the solver using
* The predefined arrays RUSER and IUSER
INTERNAL
 RUSER(1)=P
 RUSER(2)=XR
 RUSER(3)=YR
 RUSER(4)=VON
 RUSER(5)=VOFF
 RUSER(6)=INDEX
 RUSER(7)=DIST
 RUSER(8)=XINIT
 RUSER(9)=YINIT
 RUSER(10)=EMMISIVITY
 RUSER(11)=ABSOR
 RUSER(12)=TSURR
 RUSER(13)=HTC
 RUSER(14)=TAIR
```

```
 IUSER(1)=ITYPE
END
*
GEOMETRY
 GRID 3D BFC
 USE GRID FROM overlap.DTF DTF
* Cell Types
* name: Default
  SOLID Default 1 250 1 61 1 15
END
*
PROBLEM_TYPE
 SOLVE HEAT
*UNSTEADY TF = 0 TL = 1 STEPS = 10
* Define the time period for this run
* Time step size is (TL-TF)/STEPS
UNSTEADY TF = 0.12 TL = .24 STEPS = 240
END
*
PROPERTIES
 DENSITY CONSTANT 1.1563
 VISCOSITY CONSTANT_KINEMATIC 1.71e-005
 SPECIFIC_HEAT 1000
 CONDUCTIVITY PRANDTL 0.7
* SOLID_PROPERTIES Default K = 30 CP = 30 RHO = 30
* change the property values from constants to piecewise linear
 SOLID_PROPERTIES Default K = piecewise_linear CP = piecewise_linear RHO = 7840
* Define the k(T) curve
K 12
293 373 473 573 673 773 873 973 1073 1273 1473 2000
48.6 46.5 44.3 42.2 38.4 35.6 31.8 28.9 31.1 28.0 30.6 30.0
* Define the Cp(T) curve
CP 13
373 473 523 573 623 673 773 873 973 1023 1073 1173 2000
486 515 528 548 569 586 649 708 770 1583 624 548 500
END
*
MODELS
END
*
*** Boundary Conditions ***
*
BOUNDARY_CONDITIONS
* boundary condition: Default
 WALL 1 1 1 61 1 15  WEST
 U = 0 V = 0 W = 0 HC = 10 TINF = 293 TINFR = 293 EPS = 0.4
* boundary condition: Default
 WALL 250 250 1 61 1 15  EAST
 U = 0 V = 0 W = 0 HC = 10 TINF = 293 TINFR = 293 EPS = 0.4
* boundary condition: Default
 WALL 1 250 1 1 1 15  SOUTH
 U = 0 V = 0 W = 0 HC = 10 TINF = 293 TINFR = 293 EPS = 0.4
* boundary condition: Default
 WALL 1 250 61 61 1 15  NORTH
 U = 0 V = 0 W = 0 HC = 10 TINF = 293 TINFR = 293 EPS = 0.4
```

```
* boundary condition: Default
  WALL 1 250 1 61 1 1  LOW
  U = 0 V = 0 W = 0 HC = 5000 TINF = 293
* boundary condition: Default
  WALL 1 250 1 61 15 15  HIGH
*U = 0 V = 0 W = 0 Q = 10
* Change the flux boundary value from a constant to "user_defined"
U = 0 V = 0 W = 0 Q = user_defined
END
*
INITIAL_CONDITIONS
*Full field initial conditions
*T = 293
* Continue run using the restart file from from last timestep
RESTART FROM run1.0100.AUR CONTINUE
END
*
********** Solve **********
*
*
SOLUTION_CONTROL
 ALGORITHM SIMPLEC
 S_SCHEME UPWIND H
 T_SCHEME EULER
                                        ITERATIONS 30
 C_ITERATIONS 1
 SOLVER CG H
 S_ITERATIONS 5 U V W
 S_ITERATIONS 30 PP
 S_ITERATIONS 50 H
 INERTIAL_FACTOR 0.2 U V W
 INERTIAL_FACTOR 0.2 H
 RELAX 1 P RHO T VIS
 MINVAL -1e+020 U V W
 MINVAL -1e+020 P
 MINVAL 1e-006 RHO
 MINVAL 1e-010 T VIS
 MINVAL -1e+020 H
 MAXVAL 1e+020 U V W
 MAXVAL 1e+020 P RHO
 MAXVAL 5000 T
 MAXVAL 100 VIS
 MAXVAL 1e+020 H
END
*
OUTPUT
 H_TRAN ON
 DTF ON
 DTF_SCALARS T CP COND H_FLUX
 DIAGNOSTICS OFF
 TIME_SAVE 50
 UNIQUE_NAME ON
                                        END
```

VITA

Brent Blaha was born at Bethesda Naval Hospital in Bethesda, MD on March 18, 1969. The third of four children to a career naval officer, he grew up in several different locations along the East Coast of the United States. High school graduation (Kempsville High School, June 1987) occurred while living in Virginia Beach, VA. He received his undergraduate degree in Aerospace Engineering from the University of Virginia (Charlottesville, VA) in May of 1991. Yearning for further education, he started graduate studies at the University of Tennessee Space Institute (Tullahoma, TN) in August 1991. Exposing a patience that would make a sloth proud, he ultimately completed both a Master of Science degree in Mechanical Engineering (May 1994) and a Doctor of Philosophy degree, also in Mechanical Engineering (December 2000). He has a wife, Elina, and 2 sons, Jason and Allen.